

Chapter 5

Gun Experimental Characterization

In the previous chapters, I have made detailed predictions of how the gun is expected to perform. In this chapter, I report on the experimental tests I have made of those predictions. Characterization of the gun can be broken down into several categories. There are steady-state properties and there is the evolution of the system into the steady-state.

System evolution deals with the response of the beam-cavity system to the RF pulse, and includes such topics as the evolution of beam current, reflected power, and beam momentum. This topic is beyond the scope of the present work, and will be addressed in future publications. Theoretical and numerical treatment of steady-state properties appeared in Chapter 2.

For the steady-state, there is a natural subdivision into transverse and longitudinal beam properties. Of course, by transverse beam properties I mean primarily the emittance, but also the transverse phase-space *distribution*, of which the emittance is only one parameter. The emittance measurements I have done relied on the variation of a quadrupole upstream of a phosphorescent screen. From the variation of beam-size with quadrupole strength one can, as I will show, deduce the emittance (under certain assumptions). While this cannot, even ideally, provide complete knowledge of an arbitrary transverse phase-space distribution, it does provide all of the second-order moments. Also, if the measured beam size as a function of quadrupole strength

is compared to a simulation of the same experiment, using an initial beam distribution calculated by MASK, and if the two are found to be similar, then one may reasonably conclude that not only are the measured and calculated emittances in agreement, but also that the measured and calculated phase-space distributions may well be in agreement.

Longitudinal beam properties include the momentum spread and the dependence of momentum on cavity field levels, in addition to the bunch length. Momentum spectra proved one of the best diagnostics available on the SSRL system, with measurements being possible over the full range of gun operating conditions. In spite of this, there is ambiguity in the measurements in that direct knowledge of the cavity fields and cathode current density was not available.

Bunch length measurements were performed using the third preinjector linac section, phased at the null so as to impart a time-dependent momentum spread to the beam. By analysing the momentum spread with a bending magnet as a function of the fields in the linac section, the bunch length can be determined.

The term “steady-state” refers to a hypothetical condition reached by the gun after a sufficient time has elapsed since the beginning of the driving RF pulse. As I discussed in chapter 3, this condition is expected to be reached only during the later part of the (rather short) $2\mu\text{s}$ RF pulse delivered to the gun at SSRL, particularly when beam-loading is small (as happens for low-current running). This injects some ambiguity into any experiment that purports to be a measurement of a steady-state property. Additional complications arise from the fact that the RF pulse delivered to the gun had a “flat-top” with an upward slope amounting to (typically) 10% of the average power level of the flat-top.

Being a combination of a research project and a construction project serving a “higher goal”, the RF gun project did not include the most sophisticated diagnostics possible. Certainly, in order to characterize the gun sufficiently to verify many of the detailed predictions I have made in previous chapters, more complete experiments are needed than I have been able to do. However, the experiments that have been done demonstrate that the gun performs largely as expected. As my discussion of the experiments proceeds, I will indicate what the short-comings of the measurements are thought to be, and how these might be overcome in future work.

While the experiments I will report on represent my own efforts, they could never have been done without the efforts and support of many people, whom I am pleased to recognize in the acknowledgements.

5.1 Experimental Configuration

In this section, I will give an overview of the primary experimental configuration that I used at SSRL[54]. While some experiments were done at Varian or with different configurations at SSRL, the data I shall cover were taken with the configuration I shall describe here.

5.1.1 Gun-to-Linac Components

Figure 5.1 shows a schematic layout of the “Gun-to-Linac” region (or “GTL”) of the SSRL Preinjector. This system is similar to that used for the HEPL RF gun[32], in that both systems employ an RF gun with an alpha-magnet for bunch compression (see Chapters 3 and 4), along with quadrupoles to control the transverse beam size.

In addition to providing bunch compression, necessary in order to obtain low momentum spread at the end of the linac, the alpha-magnet also allows momentum filtration. As discussed in Chapter 3, the beam inside the alpha-magnet is dispersed according to momentum. A scraper (referred to as “the scraper” or “the alpha-scraper”) inside the alpha-magnet can be moved into the beam from the low-momentum side, thus allowing the operator to let through only those particles with momenta greater than a certain value (this is discussed fully in a following section). I will discuss how the alpha-scraper is used for measurement of the momentum spectrum in Section 5.3.

The scraper is only one of the variables under the control of the operator. The alpha-magnet gradient and the gradients in the quadrupoles are all independently controllable, allowing great flexibility in the optics. The RF power delivered to the gun, the phase and frequency of that power, and the cathode filament power are the gun-specific “knobs” at the operator’s disposal.

Steering magnets are also included in the transport line. These are useful for magnetic optics tests and to compensate for alignment errors, magnetic field errors, and stray magnetic fields. Each steering magnet provides both horizontal and vertical steering, using a picture-frame design with four coils. Steering magnets are placed just after the gun, before and after the alpha-magnet, and between the last quadrupole and the chopper.

Figure 5.1 also shows the traveling-wave beam-chopper[77], which is used to select

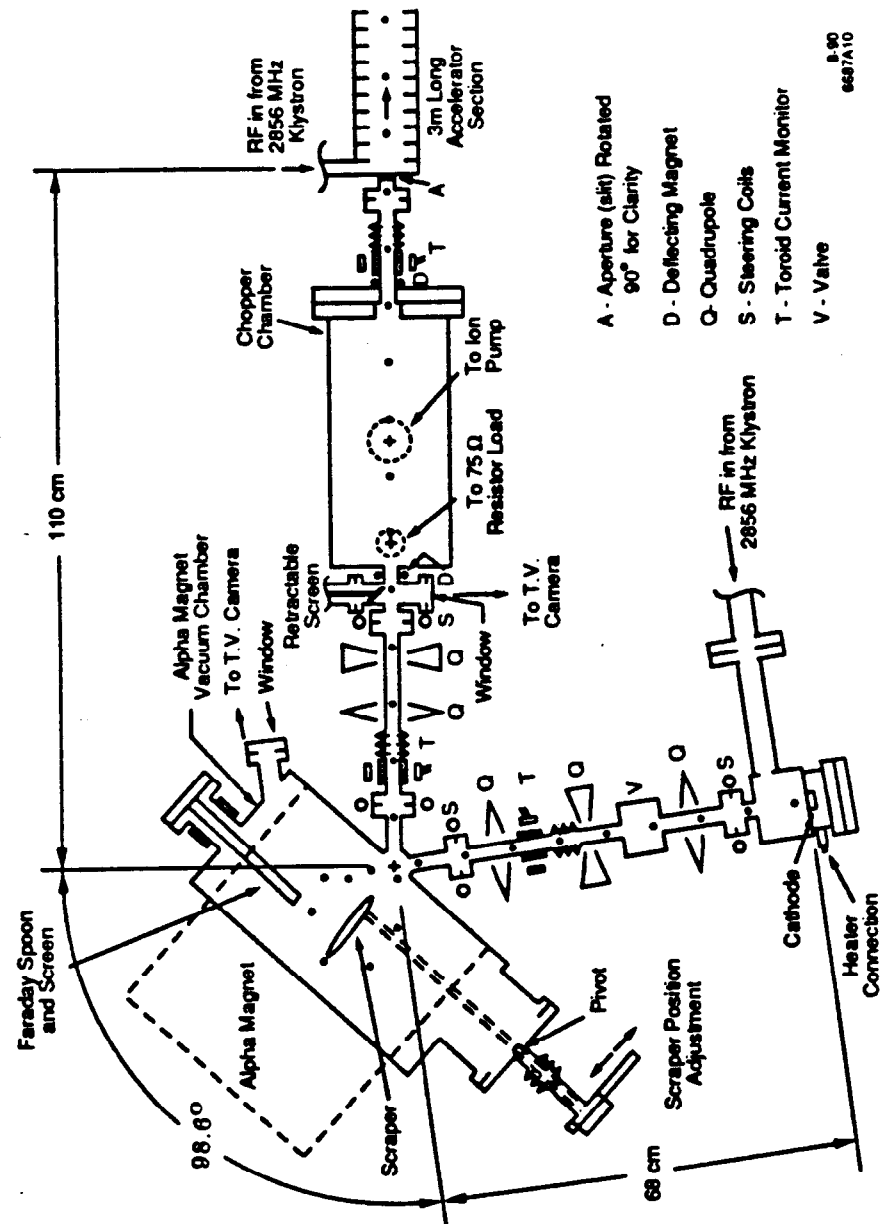


Figure 5.1: Gun-to-Linac Region of the SSRL Preinjector

three to five bunches for injection into the linac out of the train of several thousand bunches that is emitted by the gun during each RF pulse. I will not discuss the chopper further here.

5.1.2 Gun-to-Linac Instrumentation

Several types of diagnostic instrumentation are available in the GTL[78, 79]. Forward and reflected RF power signals are available from a directional coupler in the rectangular waveguide leading to the gun. The coupler is not as close to the gun as one might like: originally, the coupler was quite near the gun, but the ceramic window covering the coupling hole broke, forcing us to find a new position for the coupler. The coupler used for these experiments is about 1 m from the gun body, with a wave-guide “H-bend” and a high power RF window between the gun and the coupler. These signals are converted into voltages by calibrated diodes, so that one obtains a signal that is related to the power envelope of the RF signal in question. Because of the H-bend between the coupler and the waveguide, reflected power signals will include the effect of any mismatch between the H-bend and the rectangular waveguide leading up to it, instead of simply being a product of the match between the gun cavity and the waveguide. Cold-test measurements (performed by others) indicate, however, that the match of the H-bend to the waveguide is very good.

Beam-current measurements can be obtained from either of two toroids, one before the alpha magnet (“GT1”) and one following it (“GT2”), as well as from a “Faraday-spoon” mounted inside the alpha magnet. In addition to being the current monitors that are used in day-to-day operation of the GTL, the toroids find application in the measurement of momentum spectra. As I will discuss in more detail below, by measuring beam transmission from GT1 to GT2 as a function of scraper position, one can obtain the momentum spectrum and the beam power.

The toroids are essentially transformers, with the beam current acting as one winding of the transformer. The name “toroid” derives from the use of a ferrite torus as the core of the transformer. The torus is mounted symmetrically around the path of the beam, so that the beam goes down the axis of the torus. At the position of the torus, there is a ceramic break installed, since otherwise the image currents induced

in the metallic vacuum pipe would cancel the beam current. The other winding of the transformer consists of wire coiled around the ferrite. A shield is also installed around the torus, providing a path for image currents that goes around the outside of the ferrite. Because this image current is equal in magnitude and opposite in sign to the beam current, the effect is equivalent to having the beam current make a loop around the ferrite. Hence, the "turns ratio" of the transformer is $1 :: n$, where n is the number of turns of wire wrapped on the ferrite.

The Faraday-spoon is essentially a copper target that is held inside the alpha-magnet in such a position that it is struck by the beam whenever the alpha-magnet is turned off. The target is supported by copper tubes (which double as conduits for cooling water), which are themselves eventually supported by an electrically isolated vacuum feed-through. Hence, the electrons that are absorbed by the Faraday-spoon do not return immediately to ground, but can rather be made to return to ground through an external resistor. The voltage across this resistor is proportional to the current absorbed by the Faraday-spoon, from Ohm's law. The surface of the Faraday spoon where the electrons impact the copper was not shaped into a cup, since for electrons of 2—3 MeV, back-scattering should be negligible.

Mounted on the front surface of the Faraday-spoon is a phosphorescent screen, which emits visible light when struck by electrons. This screen, referred to as the "alpha-magnet screen", is viewed by closed-circuit TV through an optical window in the alpha-magnet vacuum chamber. This screen is heat-sunk to the Faraday-spoon, with the front surface of the Faraday-spoon being very slightly convex in order to ensure good thermal contact between the screen and the copper.

Another phosphor screen is installed down-stream of the alpha-magnet, in front of the chopper. This screen, referred to as the "chopper screen", is retractable and, unlike the alpha-magnet screen, is not water-cooled. Hence, while the alpha-magnet screen can take full beam current (more than 900 mA) without apparent harm, the chopper screen is easily damaged by too much beam current, and in addition will cause an unacceptable increase in GTL and gun vacuum pressures if inserted with more than about 50 mA current exiting the alpha-magnet. Because it follows the alpha-magnet, the chopper screen provides the only way to measure the emittance of the beam without the inaccuracy that would occur if the full momentum spread were

used. These considerations (among others, such as phosphor saturation) combine to militate against measurements of beam-emittance at high currents.

Rather than rely on bench-top calibrations of the toroids, I chose to calibrate the toroid signals (i.e., in amperes of beam current per volt of output signal) relative to the Faraday spoon. In particular, this was done by first optimizing beam transmission to the Faraday spoon. By viewing the beam spot on the alpha-magnet screen, it could be verified that no beam-scraping was occurring, which implies that the current measured by the Faraday cup is the same as that passing through GT1. Simultaneous measurements of the peak Faraday cup signal versus the peak GT1 signal were then taken as the current from the gun was varied, thus providing a calibration of GT1. (Note that since the beam current increases during the RF pulse, the peak for each signal occurs near the end of the pulse.) For a fixed-length and fixed-shape beam pulse, this procedure includes the effect of the L/R time-constant of the toroid response (estimated to be $10\ \mu\text{s}$ [80]), since the toroid is a linear device. For a shorter beam pulse than that used for the calibration, use of the same calibration would result in an over-estimate of the beam current. I will return briefly to this issue in the Section 5.3, where the measurement of spectral distributions is discussed.

5.1.3 Beamline Control and Data Acquisition

External to the concrete vault that houses the GTL is a computer-aided measurement and control system, based partly on an IBM PC compatible and partly on a DEC MicroVax II. The PC, in concert with a LeCroy 9450 digital oscilloscope (accessed via GPIB) and a MetraByte DAS-20 Data Acquisition Board, collects and stores data and controls the alpha-scrapers through a stepper-motor driver. On-line, real-time analysis of data is available through software that I wrote specifically for the experiments, and through a subset of the `mp1` Scientific Toolkit (described in Appendix 1). In particular, any waveform acquired from the oscilloscope may be plotted or subjected to various types of analyses and transformations (such as fitting, Fourier analysis, integration, differentiation, and noise subtraction) on the PC. Scope parameters may be stored on the PC and later restored to the scope under user or program control. Data taken for momentum spectra may be immediately analyzed and plotted on the PC.

The LeCroy 9450 oscilloscope can be synchronized with the sweep of the close-circuit TV cameras that are used to view the phosphorescent screens. Hence, it is possible to use the combination of the scope and PC as a "frame grabber", allowing storage of screen images for later analysis. As I will describe in more detail below, these frames were transferred to SSRL's VAX 8700 for image analysis to determine beam sizes.

The MetraByte Data Acquisition Board is used for sampling relatively slow signals and for controlling the position of the alpha-scraper. The board has eight differential A/D converter inputs, with a maximum sampling rate of 100 kHz (distributed over however many channels are sampled), as well as digital I/O and 2 D/A convertors. I have developed software to provide versatile measurement capabilities using this board. For example, an eight-channel "chart recorder" (`chart`) is available, as is a 100-kHz digital oscilloscope program (`scope`), and several programs (`dchart`, `ramp`) for automated and semi-automated magnetic measurements (or analogous measurements) using a stepper-motor or computer-controlled power supply. I used the later programs for all the magnetic measurements on the GTL. The chart-recorder program is used to monitor the gun filament current and voltage, as well as vacuum pump currents; this is particularly useful during cathode processing. For RF processing, a program (`bursts`) is available that counts vacuum bursts, to help the experimenter assess progress; as bursts are seen to decrease (or increase) in frequency, the experimenter can increase (or decrease) the RF power.

While the PC was used for all data acquisition and some control functions, primary control of GTL components was through the Injector Control System (ICS). Only the alpha-scraper was controlled from the PC. No link was available between the PC and the ICS, and hence some experiments were only semi-automated. For example, emittance all measurements required grabbing screen images as a quadrupole was varied. The experimenter was required to act as the "link" between the PC and the ICS, telling the PC when to grab a frame, and the ICS when to change the quadrupole strength. Also, data transfer from the PC to SSRL's main computer, a VAX 8700, was accomplished by copying the data from the PC to diskettes, from which they could be transferred from another PC to the VAX 8700 over a terminal line. This is not a trivial matter, since the TV frame files are quite large, so that the transfer

might take several hours for the data from a single shift of experiments. Since the floating-point representations on the PC and the VAX 8700 are different, the frame files were converted from the binary format used by the LeCroy 9450 to a packed ASCII format before being transferred.

5.1.4 The Preinjector Linear Accelerator

The SSRL Preinjector utilizes three SLAC-built 30 MW, XK5 S-Band klystrons, each driven by a separate modulator, with all the modulators sharing a single high-voltage power supply. Each klystron supplies RF power to one of the linear accelerator sections, with the second klystron (i.e., the klystron for the second accelerator section) also supplying RF to the gun via a 7-dB coupler. (Since the experiments, the coupler has been replaced with a 5-dB coupler, to supply more power to the gun.) Downstream of the 7-dB coupler is a high-power attenuator, followed by a high-power phase-shifter and then the gun. The RF drive for the second klystron is derived from an oscillator which drives a 1 kW RF amplifier. The RF drive for the other two klystrons is derived from couplers inserted in the waveguide from the second klystron. This configuration has the advantage that only one RF amplifier is needed. Also, since the power for the gun is taken from the power going to the second linac section, the first section has the full power of the first klystron, giving rapid initial acceleration in the first section.

The disadvantage of this configuration is that all RF phases are referenced to the second section, when a more congenial configuration would have all RF phases referenced to the gun. In order to phase up the linac, one must first phase the first section relative to the gun, in order to get beam into the second section; this is done by adjusting the low-power phase-shifter for the RF drive to the first klystron in order to maximize the signal on a toroid between sections 1 and 2. One then phases the gun to the second section using the high-power phase-shifter, while adjusting the phase of the first section to keep it in phase with the gun. Finally, one phases the third section to accelerate the beam exiting the second section. Any change in the phase of the bunches coming from the gun, such as will occur whenever the beam momentum changes due to beam-loading or whenever the alpha-magnet gradient is

changed, requires rephrasing all three sections. This creates difficulties for certain experiments, as I will discuss later in this chapter.

5.2 Gun-to-Linac Optics

In this section, I discuss the GTL optics. While this topic is not really an experimental one, it is relevant to the experiments, and so I have chosen to treat it in this chapter. I will present some experimental data, namely magnetic and optics measurements on the GTL quadrupole.

5.2.1 Modeling of the Quadrupoles

The optical properties of the alpha-magnet are discussed in Chapter 3. The remaining optical elements are the five quadrupoles. While I will not go into the details of magnetic measurements on these quadrupoles, Figure 5.2 shows the gradient as a function of z , the longitudinal position. Also shown in the Figure is a trapezoidal approximation to this distribution. This trapezoid was obtained by first setting the endpoints of the trapezoid to lie at the same z as the 10% points of the actual gradient. The flat-top of the trapezoid was required to be of the same height as the actual flat-top, with the length of the flat-top adjusted to make the area under the trapezoid the same as the area under the actual distribution. That is,

$$\int g(z)dz = g_o l_{\text{top}} + g_o l_{\text{fringe}}, \quad (5.1)$$

where $2l_{\text{fringe}} + l_{\text{top}}$ is the distance between the two z locations where $g = g_o/10$. For the GTL quadrupoles, $l_{\text{fringe}} = 3.28\text{cm}$ and $l_{\text{top}} = 4.43\text{cm}$. There is no compelling reason for choosing l_{fringe} as I did (i.e., based on the points at which $g = g_o/10$): it simply seemed a “reasonable” choice. Later in this section, l_{fringe} will be adjusted based on beam-optics experiments.

The equation of motion (see [6, 10] for background material) in the entrance fringe-field of the trapezoidal model is

$$x'' = -\frac{k_o}{l_{\text{fringe}}} \frac{xz}{1 + \delta}, \quad (5.2)$$

where primes represent derivatives with respect to z ,

$$k_o(\text{m}^{-2}) = 0.029979 \frac{g_o(\text{kG/m})}{\text{pc}(\text{GeV})}, \quad (5.3)$$

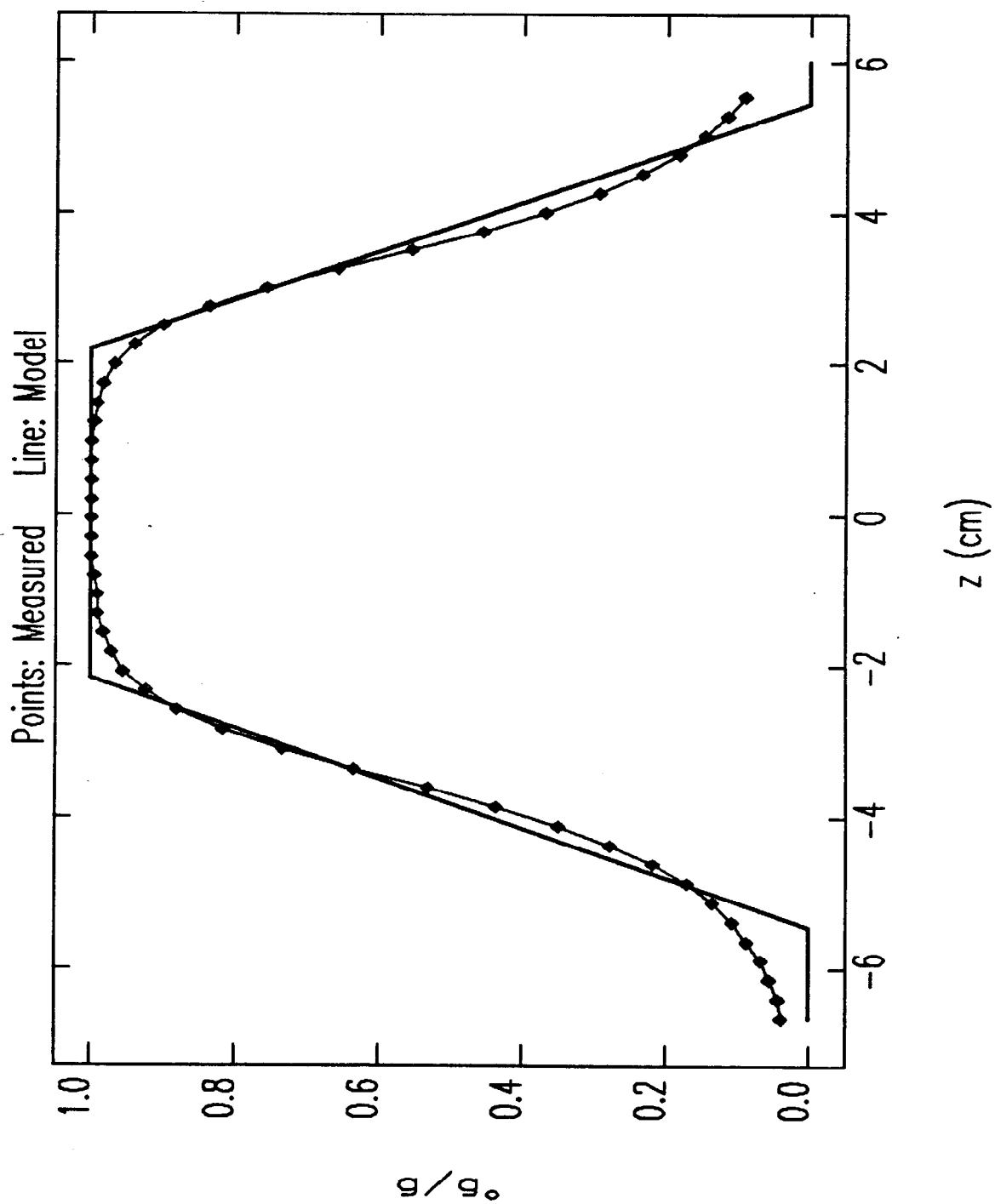


Figure 5.2: GTL Quadrupole Gradient vs Longitudinal Position

and where $\delta = (p - p_o)/p_o$ is the fractional momentum deviation. Equation 5.2 is valid for either positive or negative k_o , i.e., for either a focusing or defocusing quadrupole, respectively. It can be solved by a series of the form

$$x = \sum_{n=0}^{\infty} a_n z^n. \quad (5.4)$$

Inserting this into the differential equation yields

$$a_{3n} = a_0 \left(-\frac{k_o}{1+\delta}\right)^n \prod_{m=1}^n \frac{1}{3m(3m+1)} \quad (5.5)$$

$$a_{3n+1} = a_1 \left(-\frac{k_o}{1+\delta}\right)^n \prod_{m=1}^n \frac{1}{3m(3m-1)} \quad (5.6)$$

$$a_{3n+2} = 0, \quad (5.7)$$

where $n = 1, 2, \dots \infty$. Evaluation of the series and its derivative at $z=0$ reveals that $a_0 = x(0)$ and $a_1 = x'(0)$, which completes the solution. The solution for $x'(z)$ is obtained by simply taking the derivative of $x(z)$.

The first-order matrix-elements ($r_{11}, r_{12}, r_{21}, r_{22}$) are found by taking derivatives of $x(z)$ and $x'(z)$ with respect to $x(0)$ or $x'(0)$, with $\delta = 0$. The non-zero second-order matrix elements (t_{126}, t_{216}) are found by taking derivatives with respect to δ and then with respect to either $x(0)$ or $x'(0)$. For the exit fringe fields, one obtains the matrix by finding the reverse matrix[6] of the matrix for the entrance fringe fields. The chromatic terms clearly swap in the same way as the first-order matrix terms from which they derive. (I use the unconventional lower-case letter "r" for the transport matrix for consistency with Chapter 3.)

I have incorporated these results into the tracking/integrating code **elegant**[49], which I wrote specifically for the SSRL RF gun project. For matching purposes, I have used the program MAD[71], modified to include alpha-magnets. The quadrupole fringe-fields in MAD were simulated by breaking up each of the fringe regions into four constant-gradient sections. This was found to give good agreement with trials done with up to 50 constant-gradient sections (which were also used to confirm the exact solution given above). Later in this section, I will show results of experimental tests of this quadrupole model.

5.2.2 Optical Matching

Matching of the optics in the GTL proceeded from several assumptions and under several constraints:

1. The output phase-space of the gun varies with beam current and fields in the gun. Hence, for matching, I used an initial betatron ellipse that enclosed all of the useful beam (as defined in Chapter 2) for the full range of operating conditions. This ellipse has parameters $\beta = 0.074\text{m}$, $\alpha = 0$, and $\epsilon = 27\pi\text{mm} - \text{mrad}$.
2. Various beam-pipe and other chamber apertures must be accommodated:
 - (a) The beam-pipe radius is 18mm throughout most of the GTL, except where otherwise noted in this list.
 - (b) For 11 cm before and after the alpha-magnet, the beam-pipe radius is 11mm.
 - (c) Inside the alpha-magnet, the aperture is highly irregular (due to the shape of the magnet poles) but large enough to safely ignore.
 - (d) The horizontal aperture in the chopper is $\pm 10\text{mm}$ and the vertical aperture is $\pm 4\text{mm}$.
 - (e) There is a 30mm-long, 4mm-diameter differential pumping aperture immediately after the gun, and a slightly-constricting aperture near toroid GT1, which acts as shield for the ceramic. (The later was added well after the matching studies, and as it does not alter them, I have ignored it.)
3. A gently convergent beam in both planes is desirable at the entrance to the linac, in order to match to the linac transverse acceptance (i.e., to avoid scraping beam on the apertures inside the linac). In addition, the vertical beam size should be less than 2mm at the final chopper slits (just before the linac) in order to obtain proper chopping[77], and the horizontal beam size at the linac entrance should be less than 9mm
4. The alpha-magnet gradient is dictated solely by the needs of bunch compression (see Chapter 4), and hence the rest of the optical elements must be adjusted to

accommodate the alpha-magnet. The alpha-magnet matrix can be expressed as a function of the size of the alpha-shaped loop made by the central particle, \hat{q}_1 (which is inversely proportional to the parameter α used in Chapter 3, and which is also called x_{\max} in some of the literature[45, 32]). Similarly, the compression is related to this parameter, so that in order to accommodate a wide range of alpha-magnet settings, I did the matching for a number of values of \hat{q}_1 between 9cm and 15cm. Some results of this matching are shown below.

5. It was desired that the momentum resolution of the alpha-magnet momentum filter be a few percent. The momentum resolution is roughly[6]

$$\delta_{\text{res}} = \frac{\sqrt{\epsilon\beta}}{D}, \quad (5.8)$$

where the dispersion at the midpoint in the alpha-magnet is $D = \hat{q}_1/2$, and is typically 4-8 cm, depending on how the alpha-magnet is set for pulse compression and what the central momentum is. Hence, β at the midpoint is required to be less than 0.006 m for 1% resolution. Typically, I achieved better than 2% nominal resolution. Baring excessive second-order effects, the actual resolution should be better than the nominal resolution, since the initial phase-space is smaller than what I used for the matching. Second-order simulations with elegant confirm this expectation, as I shall show in the next section.

Table 5.1: Quadrupole Strengths for GTL Optics Solutions for Various Values of \hat{q}_1

\hat{q}_1 (cm)	k_o for Q1 (1/m ²)	k_o for Q2 (1/m ²)	k_o for Q3 (1/m ²)	k_o for Q4 (1/m ²)	k_o for Q5 (1/m ²)	$\delta_{\text{res,nom}}$ (%)
9.00	244.04	-142.95	150.50	107.71	-84.24	2.0
10.00	234.39	-142.05	150.08	105.61	-83.54	1.9
11.00	229.30	-141.17	148.96	104.01	-83.04	1.9
12.00	224.88	-140.36	147.76	102.54	-82.55	1.8
13.00	222.18	-139.60	146.37	101.25	-82.12	1.8
14.00	210.71	-138.74	145.92	99.43	-81.31	1.7
15.00	225.68	-138.36	142.71	99.44	-81.58	1.7

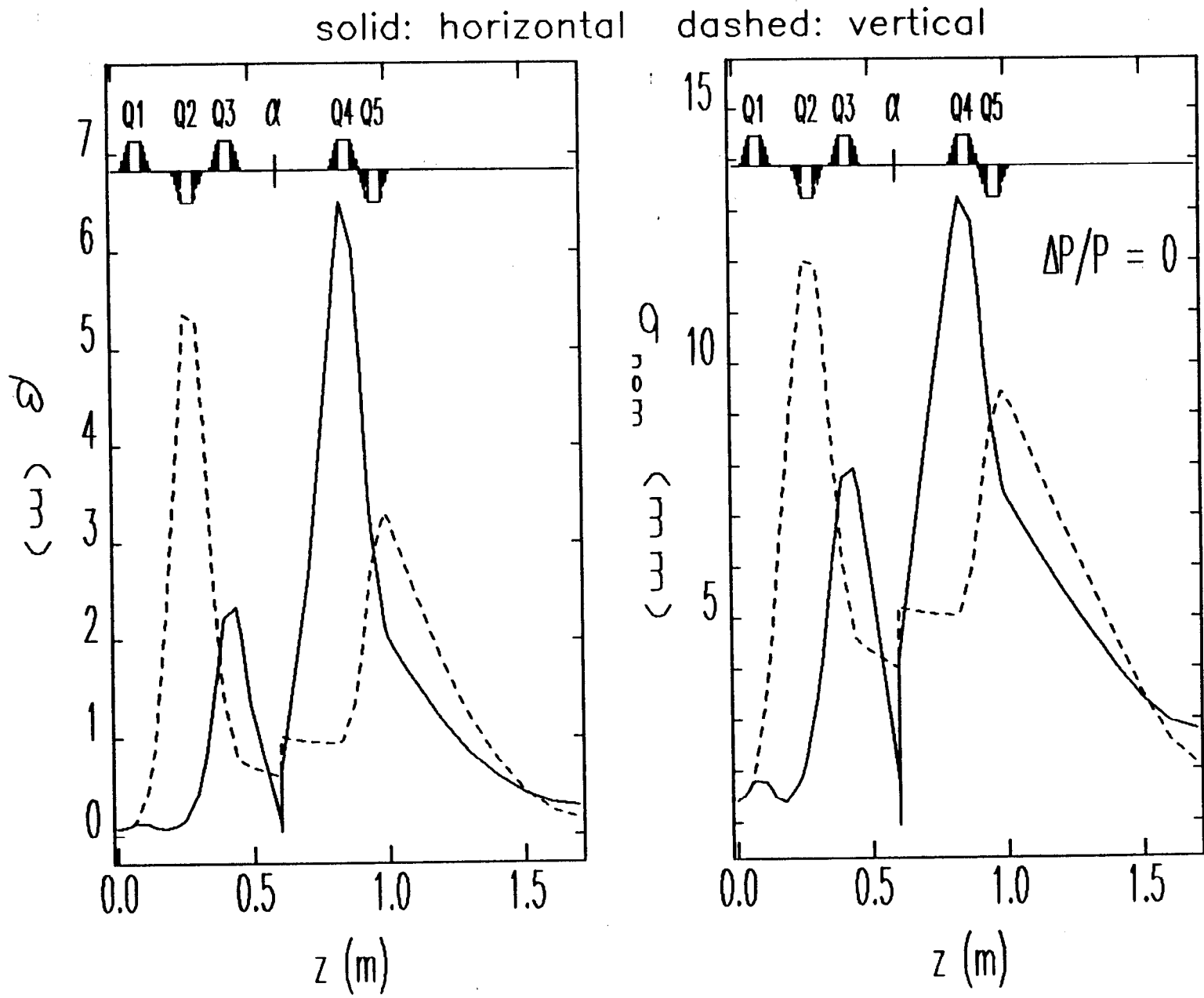


Figure 5.3: GTL Optics Solution for $q_1 = 11\text{cm}$

Using the results of Chapter 3, I have added alpha-magnets to MAD. Figure 5.3 shows a “typical” optics solution for the GTL, in this case for $\hat{q}_1 = 11\text{cm}$. The alpha-magnet appears as a zero-length element at $z = 0.6\text{m}$. The quadrupole strengths for this solution and several similar ones for different values of \hat{q}_1 are listed in Table 5.1. These optics solutions are designed for the case when one wants to accelerate the beam in the linac. When one is interested only in doing experiments in the GTL, some of the constraints are changed or eliminated, resulting in qualitatively different solutions. I will discuss such optics solutions as needs dictate.

5.2.3 Higher-Order Effects

These optics solutions assume that a first-order treatment of the beam-optics problem is adequate. This is known not to be the case for the GTL, because of the large momentum spread of the gun beam. One of the design goals, as discussed in Chapter 2, was to be able to make use of $\pm 10\%$ momentum spread out of the gun, in order to increase the useful beam current. Because the focal length of a quadrupole of a given gradient is inversely proportional to the momentum, a $\pm 10\%$ variation in momentum implies a $\pm 10\%$ variation in quadrupole focal length. Hence, a lattice that is matched for the “on-momentum” particles in the beam may well be seriously mis-matched for the off-momentum particles in the beam. The best way to investigate the seriousness of this problem is to do second-order tracking, which I have done using *elegant*.

In particular, Figure 5.4 shows the results of first- and second- order tracking with *elegant*. The initial particle distribution was obtained from a MASK simulation (with $E_{p2} = 75\text{MV/m}$ and $J = 10\text{A/cm}^2$, with the particle momenta being pre-filtered to ensure that the beam-sizes refer to the desired $\pm 10\%$ momentum spread all along the beamline. (Had this not been done, the beam-sizes would have dropped dramatically after the alpha-magnet, due to the filtering action of the scraper.) The optics is the same as that used to make Figure 5.3; note, however, that the beam-sizes will not agree, since the initial conditions assumed for Figure 5.3 are general acceptance parameters which do not match the initial conditions for any particular beam from the gun.

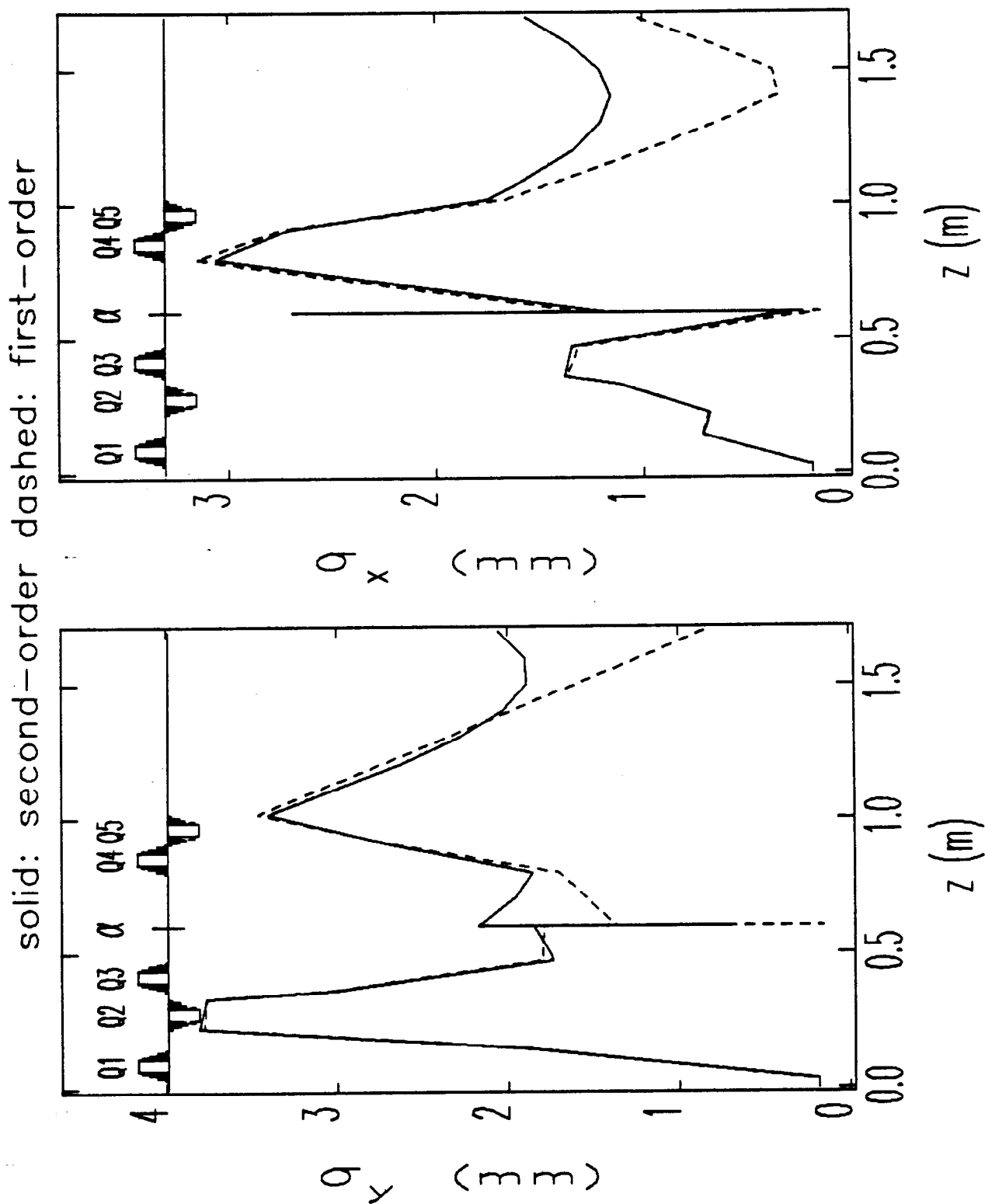


Figure 5.4: Beam-sizes for GTL Optics Solution for $\hat{q}_1 = 11\text{cm}$, from First- and Second-Order Tracking with *elegant*, for MASK-generated Initial Particle Distribution, $\Delta P/P = 10\%$.

Because the focusing is different for different momenta, the transverse beam emittance must change as the beam goes through the GTL. To see this, consider a beam with initial phase-space described by $x' = \alpha x$ and some spread of momentum deviations, $\delta = (p - p_o)/p_o$, where I assume that $\langle x\delta \rangle = 0$. The RMS emittance for such a distribution is zero, as can be verified using the definition of the emittance:

$$\epsilon = \pi \sqrt{\langle x^2 \rangle \langle x'^2 \rangle - \langle x'x \rangle^2} \quad (5.9)$$

If this beam goes through a thin-lens quadrupole with focal length f_o for the central momentum, then the coordinates after the quadrupole are

$$\bar{x} = x \quad (5.10)$$

$$\bar{x}' = x \left(\alpha - \frac{1 - \delta}{f_o} \right), \quad (5.11)$$

where I have expanded the focal length to first order in δ . The emittance for this new distribution is

$$\bar{\epsilon} = \pi \frac{x_{rms}^2 \delta_{rms}}{f_o}. \quad (5.12)$$

For a beam with δ uniformly distributed on $[-\delta_o, \delta_o]$, $\delta_{rms} = \delta_o/\sqrt{3}$. Thus, for example, if $x_{rms} = 10\text{mm}$ and $\delta_o = 0.1$, then for $f_o = 0.5\text{ m}$, one sees that $\bar{\epsilon} \approx 12\pi \cdot \text{mm} \cdot \text{mrad}$. This indicates that emittance blow-up due to chromatic aberrations should be significant in the GTL, as the simulations confirm. In particular, Figure 5.5 shows the emittance for the x and y planes as a function of position in the GTL, for the same lattice and beam conditions used in the previous Figure. Note that the changes in the emittance are much more apparent than the changes in the beam sizes. There are several reasons for this. First, the chromatic aberrations in the quadrupoles change the emittance by changing the angular coordinates, so that a large change in the emittance at the exit of a quadrupole does not entail a large change in the beam-size. Only after the beam has traveled some distance down the beam-line will the beam-size change significantly. Second, the beam-size scales like the square-root of the emittance, so that fractional changes in the beam-size are expected to be generally less than fractional changes in the emittance.

It is difficult to characterize the emittance degradation in general, since it depends on the initial phase-space, the lattice, and the momentum spread under consideration.

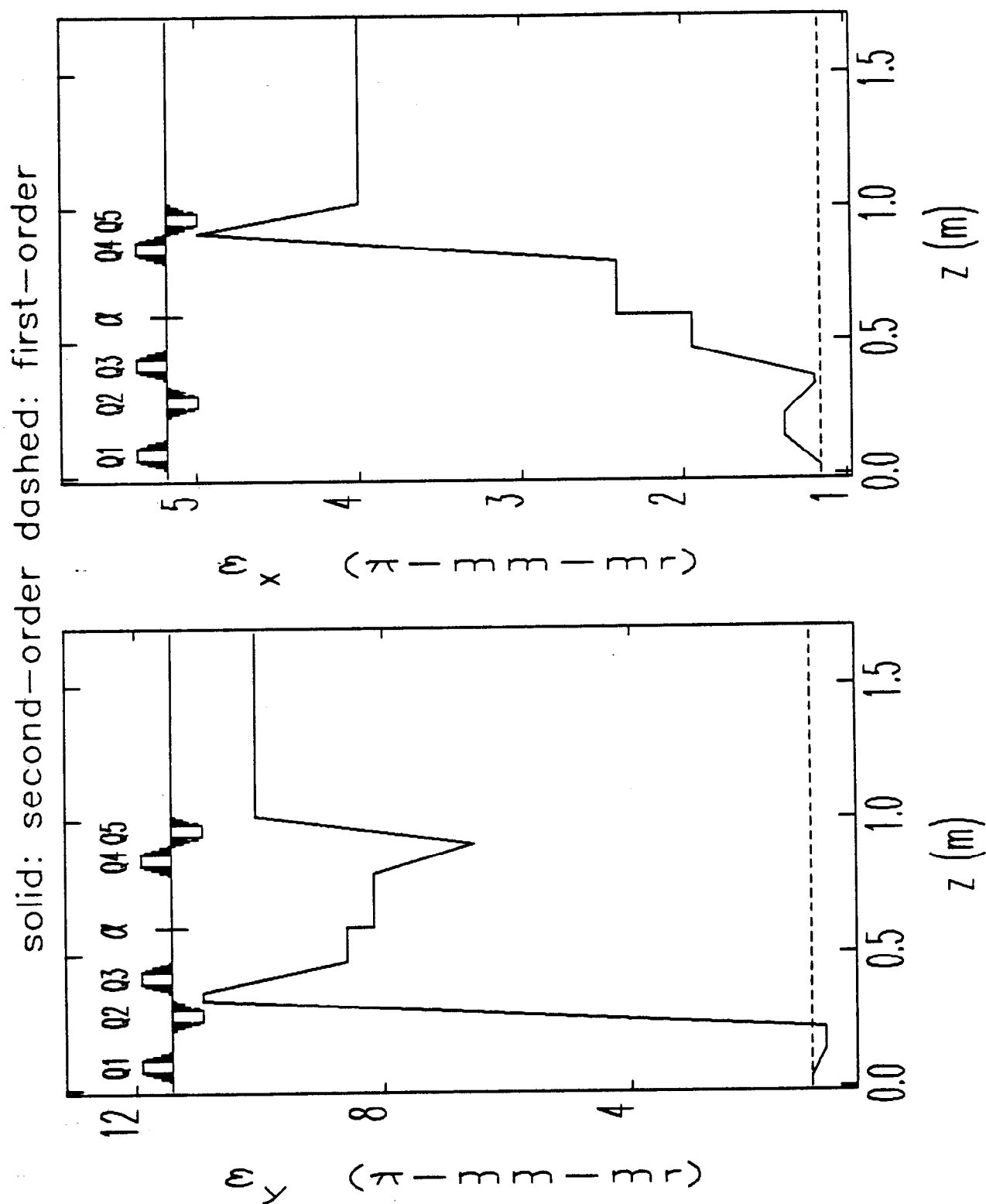


Figure 5.5: Emittance Degradation for GTL Optics Solution for $\hat{q}_1 = 11\text{cm}$, from First- and Second-Order Tracking with *elegant*, for MASK-generated Initial Particle Distribution, $\Delta P/P = 10\%$.

However, the results shown in Figure 5.5 are typical of the effects on MASK-generated initial particle distributions for the lattices listed in Table 5.1, when $\pm 10\%$ momentum spread is taken from the initial distribution. In general, these lattices blow up the x-plane emittance to about twice what the y-plane emittance is blown up to. Later in this chapter, I will show comparable data to that in Figure 5.5 for the lattice used in the emittance measurements, where in contrast the relative degradation of the two planes is reversed. Because of such difficulties, I will simply give a rough characterization of the emittance at the end of the GTL by stating that the geometric mean of the x- and y-plane emittances, $\epsilon_m = \sqrt{\epsilon_x \epsilon_y}$, is $5\text{--}6 \pi \cdot \text{mm} \cdot \text{mr}$. This result is independent of the current density used in the MASK simulation, because chromatic effects after the gun overwhelm space-charged induced emittance growth in the gun.

I have not investigated the possibility of finding a lattice that has a minimal effect on the emittance while still satisfying the constraints listed above. The optics is to a large extent dictated by the need for small horizontal beam-sizes at the vertical midplane in the alpha-magnet (for momentum filtration), and by the long drift-space between Q5 and the linac (required for the chopper). Creating a small horizontal beam-waist inside the alpha-magnet requires a large beam-size at Q3, which requires strong Q1 and Q2. Similarly, to create beam-waists at the linac entrance requires large beam-sizes at Q4 and Q5, which in turn requires strong focusing prior to Q4 and Q5. As equation (5.12) illustrates, the emittance-degrading effect of a quadrupole increases with increasing beam size and quadrupole strength.

5.2.4 Experimental Tests of the Quadrupole Model

Finally for this section, I discuss the results of experiments designed to test the modeling of the GTL quadrupoles. This is important, since the quadrupoles are used for emittance measurements, as reported in a later section of this chapter. The present experiment involved GTL quadrupoles Q4 and Q5, as well as the steering magnet (GTL-CORR3, which provides independent horizontal and vertical steering) between the alpha-magnet and Q4. The current in the steering magnet was varied in order to vary the angular “kick” it imparted to the beam. This kick in turn causes the beam position at the chopper screen to vary. By measuring the movement of the

beam spot as a function of the kick, one can probe the optics of the elements between the steering magnet and the screen. In particular, by making vertical deflections one can determine the r_{34} matrix element for beam transport from the steering magnet's principle plane to the screen[6, 10]. I confine myself to the vertical plane, since the horizontal and vertical planes are equivalent in this case (the quadrupoles have bipolar power supplies), and since there were problems with the steering magnet power supply for the horizontal plane when I took the data.

The measurements made use of the LeCroy 9450 oscilloscope's ability to trigger off of and digitize TV signals, so that the position of the center of the beam spot could be determined accurately using the cursors on the scope. This yields positions in terms of sweep time, which can be converted to Δy relative to the position for zero kick-angle by making use of a calibration of the sweep obtained by noting the positions in the sweep of two identifiable features on the screen, the distances between which are known. For the present work (both for the r_{34} measurements and the emittance measurements reported later), the sweep was calibrated by directing the beam to the edge of the screen, thereby producing a sharp feature that was readily identified on the oscilloscope. Since the calibration changed from experiment to experiment (usually because the camera was "adjusted" or bumped), I will not record the calibrations here.

With quadrupoles Q4 and Q5 turned off (and degaussed), the transport matrix from GTL-CORR3 is simply that for a drift space, and hence $r_{34} = z_s - z_k$, where z is the longitudinal coordinate and the subscripts stand for Screen and Kick, respectively. Ideally, one would like to know z_k and z_s accurately, and use the measurement with Q4 and Q5 off to calibrate the kick vs current. This is what was done for the experiments reported on in the last section of Chapter 3, where I discuss how to calculate the offset of z_k from the geometric center of the steering magnet (the offset occurs because of the long fringe fields). Unfortunately, mechanical difficulties prevented GTL-CORR3 from being placed at the expected location, and it instead had to be placed much closer to Q4 and to toroid GT2 (which has a ferrite core) than was expected. Hence the magnetic measurements made for this steering magnet prior to installation are not valid, and I simply assumed that the principle plane is $1.8 \pm 1\text{cm}$ ahead of the mechanical center the steering magnet (the offset for GTL-CORR2 was found to

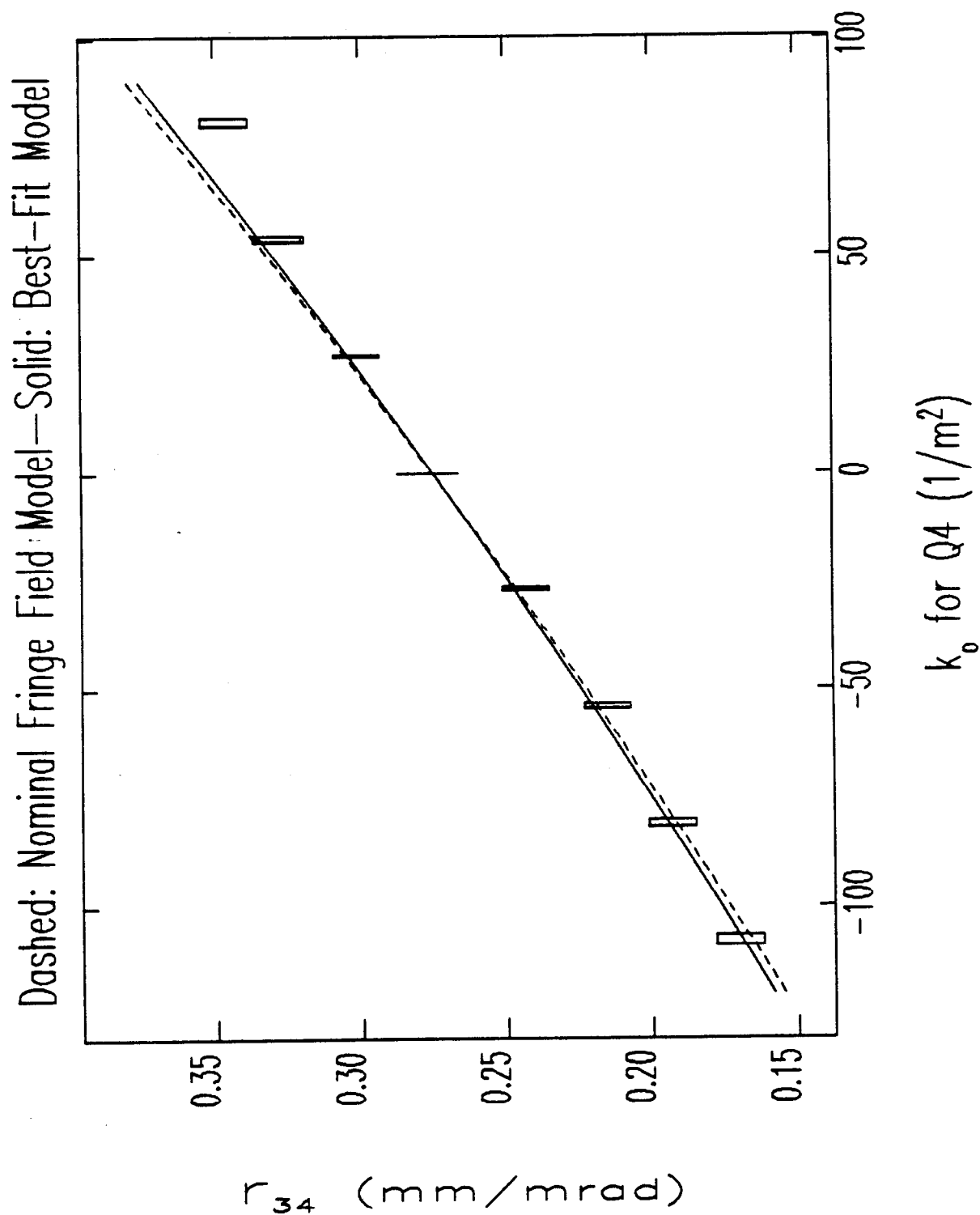
be 1.8cm). With this assumption, I calibrated the steering kick vs current from data taken with Q4 and Q5 off by requiring that $r_{34} = z_s - z_k = 0.274 \pm 0.010\text{m}$ and assuming the kick to be linear in the current (a reasonable assumption for these low-field steering magnets).

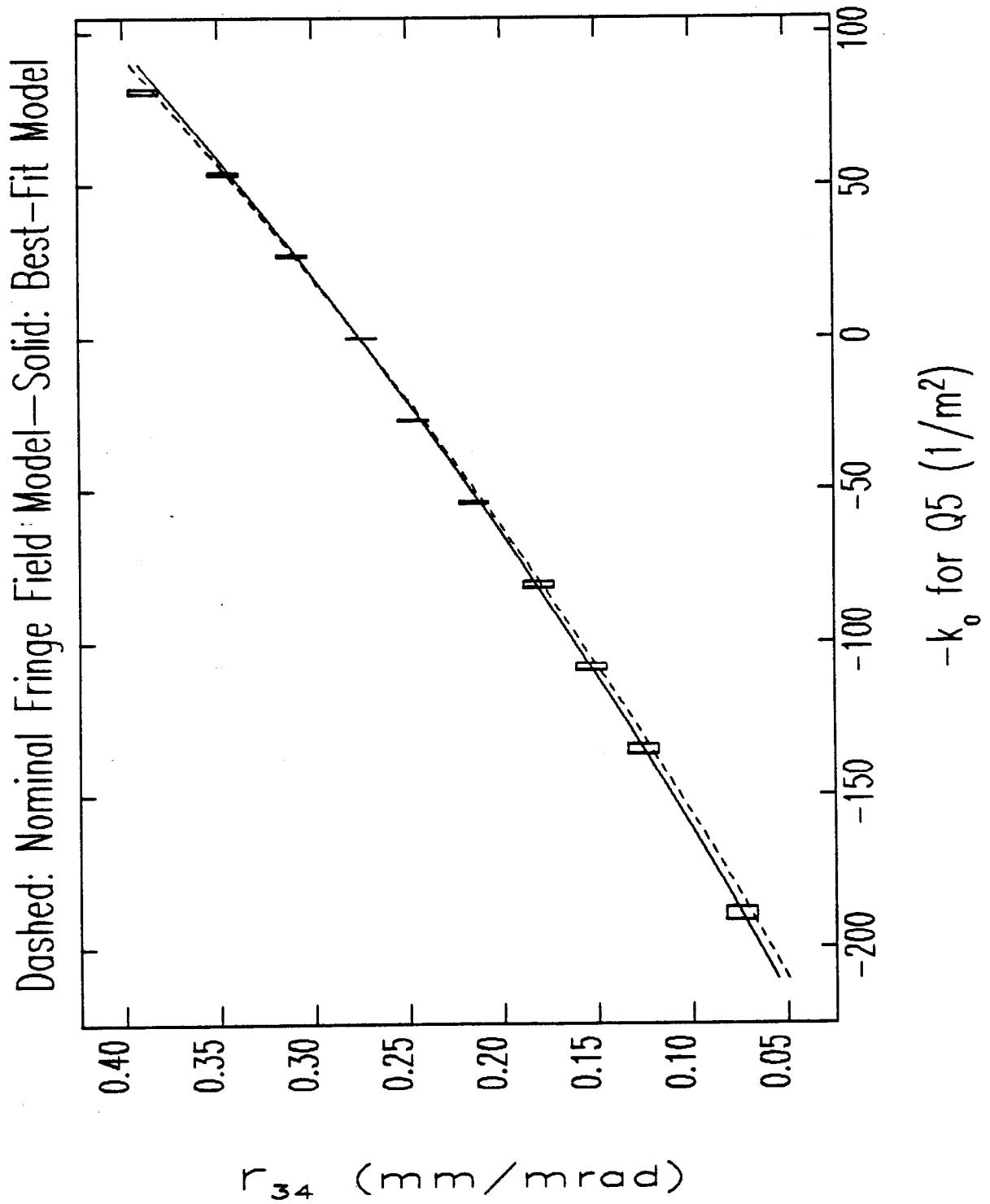
Several factors need to be taken into account in assessing the results with the quadrupoles on. The beam from the gun has a very large momentum spread (see Chapter 2, and the next section of this chapter), and hence I set the alpha-scraper to filter out a fairly small momentum spread (about $\pm 3\%$), consistent with getting a sufficiently intense beam spot. The magnet settings (i.e., the nominal k_0 values of the quadrupoles) were referenced to some nominal “lattice” momentum that was not the same as the actual beam momentum. Correction for this small effect is made by multiplying the nominal quadrupole strengths by 0.97 ± 0.01 to get the actual k_0 values. This also introduces the uncertainty in the beam momentum into the quadrupole strength.

Figures 5.6 and 5.7 show the results two sets of measurements. The first set (Figure 5.6) was made with quadrupole Q5 turned off and degaussed; the strength of quadrupole Q4 was varied, and data was taken to allow r_{34} to be deduced by fitting a line to $(\theta, \Delta y)$. Similarly, the data in Figure 5.7 was taken with quadrupole Q4 turned off and degaussed, with the strength of Q5 being varied. Also shown in the Figures are the results of matrix calculations (done with *elegant*) made using the trapezoidal quadrupole model discussed above. Each figure shows the simulation result for the quadrupole model with the nominal parameters given above (i.e., $l_{\text{fringe}} = 3.28\text{cm}$ and $l_{\text{top}} = 4.43\text{cm}$), as well as a simulation result obtained with l_{fringe} changed to 3.00 cm.

This latter result is an approximate best fit (in the least-squares sense) to the data, taking l_{fringe} as the parameter to be fit. This best-fit model has approximately 4% less integrated strength than the model with nominal parameters. It is a compromise between best fits for the individual data sets, and hence isn’t a best fit for either data set by itself. While it is possible to fit the two data sets separately, I decided to find a single fit that matched both reasonably, to make subsequent work less complicated.

The point at $k_0 = 81 \text{ m}^{-2}$ for Q4 was considered spurious and was ignored in the fitting; it would appear that the quadrupole was set incorrectly when this data point was taken. It may appear that this point could be the result of saturation. However,

Figure 5.6: r_{34} vs Strength of Quadrupole Q4, with Q5 off.

Figure 5.7: r_{34} vs Strength of Quadrupole Q5, with Q4 off.

saturation was taken into account in the calibration of k_0 versus driving current, and is in any case a negligible consideration for these quadrupoles at the currents used.

There are a number of possible explanations for the discrepancies between the model and the experimental results. The measurements were made on a magnetically isolated quadrupole, whereas the quadrupoles are installed with other magnetic materials in close proximity. Both Q4 and Q5 have a magnet-steel picture-frame steering magnet less than 30 mm away. The magnets are supported by rails that are made of magnetic steel. Finally, Q4 and Q5 are close enough that the fringe field of one quadrupole extends into the other quadrupole. Also, the nominal fringe-field model was itself guess, and should not be expected to agree exactly with the experimental data. The fact that I have fit the data using l_{fringe} as a parameter does not, of course, mean that the length of the fringe fields is actually responsible for the discrepancy, though it is the most likely choice. Whatever the source of the quadrupole strength error, the data are consistent with $l_{\text{fringe}} = 3.00\text{cm}$, and I shall use this value in the all of the analysis in this chapter.

5.3 Momentum Spectra

5.3.1 Principle of Spectrum Measurements

As I mentioned in the previous section, measurement of momentum spectra made use of current-measuring toroids GT1 and GT2 and the alpha-scraper. If the alpha-magnet gradient is g (in G/cm), then the size of the alpha-shaped trajectory executed by an on-axis particle with momentum $p = \beta\gamma$ is (see Chapter 3)

$$\hat{q}_1(\text{cm}) = 75.05 \sqrt{\frac{p}{g}}, \quad (5.13)$$

where q_1 is measured from the inner surface of the alpha-magnet front plate. (I will ignore the effects of less-than-perfect momentum resolution introduced by the non-zero beam emittance for now.) Thus, if the outer edge of the alpha-scraper is at $q_1 = q_{1,\text{outer}}$, then momenta above

$$p_{\text{outer}} = g \left(\frac{q_{1,\text{outer}}}{75.05} \right)^2 \quad (5.14)$$

will be allowed through the alpha-magnet. The inner edge of the alpha-scraper is at $q_1 = q_{1,\text{inner}} \approx q_{1,\text{outer}} - l_s$, where $l_s = 7.3\text{cm}$ is the length of the absorbing copper block that does that actual scraping of the beam. (These relations are only approximately true, since the scraper swings in an arc rather than moving linearly in q_1 , as I shall discuss presently.) As the scraper is moved toward larger q_1 , low momentum particles can in principle begin to pass through the alpha-magnet by virtue of having $\hat{q}_1 < q_{1,\text{inner}}$. Particles with momenta below

$$p_{\text{inner}} = g \left(\frac{q_{1,\text{inner}}}{75.05} \right)^2 \quad (5.15)$$

will be able to pass through. Hence, the scraper acts as a notch momentum filter, eliminating momenta between p_{inner} and p_{outer} . The current through GT2 (which is ideally proportional to signal measured on GT2) as a function of the "scraper position", $q_s = q_{1,\text{outer}}$, is thus given by

$$S_2(q_s) = \int_0^{p_{\text{inner}}(q_s - l_s)} \rho_p(p) dp + \int_{p_{\text{outer}}(q_s)}^{p_{\text{max}}} \rho_p(p) dp \quad (5.16)$$

where p_{\max} is the maximum momentum that can be transmitted through the alpha-magnet and $\rho_p(p)dp$ is proportional to the number of particles in the range $[p, p + dp]$. p_{\max} is determined by the position of the outer wall of the vacuum chamber, and is typically well beyond the upper momentum in the beam. $\rho_p(p)$ is, of course, "the spectrum" and is what is to be determined. For convenience, I choose to normalize $\rho_p(p)$ in such a way that

$$\int_{p_{\min}}^{p_{\max}} \rho_p(p) dp = 1, \quad (5.17)$$

where the integral is over the range of momenta that exit the alpha-magnet. Hence, $S_2(q_s)$ is the transmitted current with the scraper at q_s , normalized to the total transmitted current (i.e., with the scraper moved out of the beam).

5.3.2 Practical Considerations and Simplifications

Because of the limited momentum-acceptance of the beamline leading to the alpha-magnet, and because of the length of the alpha-scraper, it is a very good approximation to ignore the first term in equation (5.16). A typical gradient for a momentum spectrum measurement is 100-200 G/cm, with the maximum momentum in the beam being 2-3 MeV/c, or 4-6 $m_e c$. The worst-case is when the gradient is small and the peak momentum is large, since this produces the largest values of \hat{q}_1 relative to the fixed size of the scraper. Hence, when $p_0 = 6$ and $g = 100$ G/cm, one sees that $p_i \approx 1.9$. That is, when the scraper is in such a position so as to eliminate the highest-momentum particles in the beam, then low-momentum particles of momenta up to 1.9 are also let through. These particles, however, never reach the alpha-magnet, being eliminated by the combined effect of the strong quadrupoles and beam-pipe apertures between the gun and alpha-magnet. This is confirmed by simulations and can be tested experimentally by noting whether transmission increases as the scraper is moved past the point at which the maximum beam momentum is being intercepted. In any given measurement, one can verify that there are no low-momentum particles getting past the scraper on the low-momentum side by verifying that the transmitted current does not increase until one moves well beyond the point where the maximum momentum in the beam is intercepted.

Similarly, by choosing the gradient properly, one can place p_{\max} well beyond the

maximum momentum in the beam. Hence, through judicious choice of the experimental parameters, one can employ a simplified form of equation 5.16, namely

$$S_2(q_s) = \int_{p_{\text{outer}}(q_s)}^{\infty} \rho_p(p) dp \quad (5.18)$$

In order to obtain $\rho_p(p)$, one simply takes the derivative of $S_2(q_s)$ with respect to p_{outer} :

$$\rho_p(p) = - \frac{\partial S_2(q_s)}{\partial q_s} \frac{\partial q_s}{\partial p_{\text{outer}}}. \quad (5.19)$$

Thus, one can find the momentum spectrum, $\rho_p(p)$, from readings of the current on GT2 as a function of scraper position, i.e., by taking $S_2(q_s)$ as a function q_s .

There are several additional points that require discussion here:

1. The current into the alpha-magnet, as measured by the signal on the first toroid, S_1 , is supposed to be held constant during such a measurement. Often there are slight drifts in S_1 , due to slight drifts in RF power or filament power. Hence, it is best to normalize $S_2(q_s)$ to S_1 , with both signals being read simultaneously after each motion of the scraper.
2. Because the gun current varies during the RF pulse, it is necessary to read both toroid signals at the same point in the pulse. Just what point that is depends on what one is interested in. Typically, I was interested in the momentum spectrum for the steady-state, and hence I read the toroids late in the pulse, but before the RF pulse had started to fall off. (This assumes that it is reasonable to neglect the inductive nature of the toroid response—see below.) Figure 5.8 shows two typical pulses for the current toroids, along with the corresponding RF pulses.
3. There is some pulse-to-pulse jitter in the toroid signals, as well as some baseline drift if the linac is not synchronized to the 60-Hz line. Hence, I averaged the toroid signals over (typically) ten pulses, and triggered the oscilloscope in such a way that the baseline could be read from the first part of the waveform (i.e., I pretriggered the scope ahead of the modulator pulse).
4. The toroid pulses in Figure 5.8 look quite clean, because I have subtracted stored RFI (radio-frequency interference) pulses. Had I not done this, the pulses would

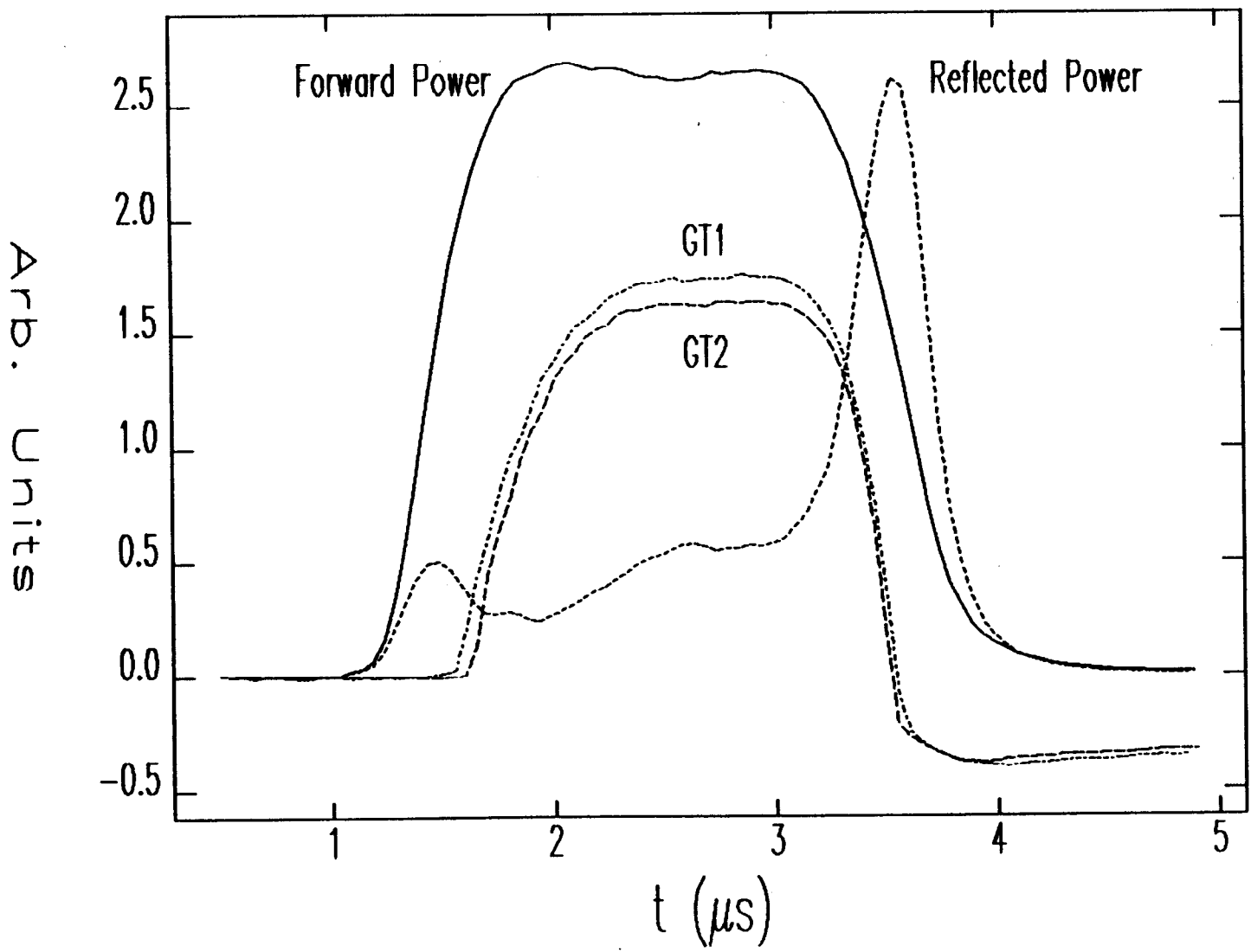


Figure 5.8: Typical Toroid and RF Pulses

show oscillations due to stray signals present in the experimental environment (mostly due to the firing of the thyatrons in the modulators). While the LeCroy 9450 permits subtraction of signals, it cannot simultaneously average a signal and do subtraction. Hence, the subtraction was performed on the PC, using previously sampled toroid “noise” signals taken with the RF drive turned off.

I have incorporated all of these considerations into the program `spect3`, which I have used for all of the spectrum measurements presented in this work. The program first reads an input file that specifies how much to move the scraper between readings, as well as giving other parameters of the measurement. It requests the user to turn off the RF power, after which it reads S_1 and S_2 to get RFI samples, which are subtracted from the toroid signals as the program takes the data. After turning the RF back on and waiting an appropriate interval for the gun emission to restabilize (typically less than 30 seconds, depending on the current), the user lets the program continue. It moves the scraper and reads S_1 and S_2 after each movement, averaging over as many pulses as the user requested in his input file, then subtracting noise. The signals read from the scope are equi-spaced samplings of whatever appears on the oscilloscope screen. The program averages over several (how many is specified by the user) samples at the very beginning of the waveforms to obtain the baseline, and over several samples at the very end of the waveform to obtain the desired current. Hence, the user must set up the scope so that the portion of the pulse he is interested in obtaining the spectrum for comes at the end of the waveform.

Some complexity is introduced into the measurements by the fact that the width of the beam pulse varies with scraper position, since the momentum spectrum changes as the fields build up in the gun. As mentioned in Section 5.1, the toroids have an L/R time-constant of $10\ \mu\text{s}$. The response to a square-wave current pulse is a decaying exponential with this time-constant. For a pulse of length $\tau \ll L/R$, the response falls off to $1 - \tau R/L$ by the end of the pulse. The FWHM of the beam pulse on the Faraday spoon is at most $1.5\ \mu\text{s}$. Hence, the calibration of the toroids against the Faraday spoon, made for a full-length beam pulse, would be at most 15% in error for a very short pulse (i.e., $\tau \rightarrow 0$, provided τ is large compared to 2 ns, which is the response time of the ferrite[80]).

This issue was not appreciated at the time the experiments were done, and I must

content myself with estimating the likely effect on the measurements that have been taken. The measurements could have been taken using a Faraday cup at the alpha-magnet exit, to avoid the toroid response issue altogether. However, this would have interfered with commissioning efforts, and was not possible. In the future, it would be advantageous install an insertable Faraday cup after the alpha-magnet.

The toroid pulses were read near the end of the flat top (see Figure 5.8). Assuming a square current pulse, the signal on GT2 at the end of the pulse is (compare with equation (5.18))

$$S_2(p_s) = \left(1 - \frac{\tau(p_s)}{T}\right) \int_{p_s}^{\infty} \rho_p(p) dp, \quad (5.20)$$

where $T=L/R$ and where $\tau(p_s)$ is the pulse width when particles of momentum greater than p_s are let through the alpha-magnet. (I have expressed S_2 as a function of p_s rather than q_s in order to simplify the analysis.) Taking the derivative with respect to p_s , one obtains

$$\frac{\partial S_2}{\partial p_s} = -\rho_p(p_s) \left(1 - \frac{\tau(p_s)}{T}\right) - \frac{S_2(p_s)}{1 - \frac{\tau(p_s)}{T}} \frac{1}{T} \frac{\partial \tau(p_s)}{\partial p_s}. \quad (5.21)$$

In my analysis, I have equated $\frac{\partial S_2}{\partial p_s}$ with $-\rho_p(p_s)$. To first order in τ , the fractional error made in doing this is

$$\frac{\Delta \rho_p(p_s)}{\rho_p(p_s)} \approx -\frac{\tau(p_s)}{T} + \frac{S_2(p_s)}{\rho_p(p_s)} \frac{1}{T} \frac{\partial \tau(p_s)}{\partial p_s}, \quad (5.22)$$

where $\Delta \rho_p > 0$ corresponds to over-estimation of ρ_p . Since $\tau(p_s)$ and $S_2(p_s)/\rho_p(p_s)$ are decreasing functions of p_s , the error in the spectral density *decreases* as p_s increases toward the maximum momentum in the beam. In fact, both $\tau(p_s)$ and $S_2(p_s)/\rho_p(p_s)$ go to zero as p_s approaches the maximum beam momentum, p_{\max} . Since the peak of the spectral distribution (see subsection 5.3.5) is near p_{\max} , the error in the measurement of ρ_p will become increasingly small as p_s approaches the peak. This indicates that the relative error in the spectral densities measured near the momentum peak is significantly less than the 15% variation in the calibration, so that it is likely that measurements of the widths of momentum peaks are reasonably accurate.

As for the beam power measurements, note that the width of the current pulse varies from 1.5 μ s to essentially zero as the scraper is moved into the beam. Hence,

the error in beam power measurements is less than 15 %, and probably more like half of that.

As I mentioned above, the scraper does not move only in the q_1 direction, but rather swings in an arc from a pivot point on a lever arm $L_a = 46\text{cm}$ long. The length of the chord between the two extremal positions of the scraper is $8.3 \pm 0.14\text{cm}$. Hence, the angular range is 10° , so that the motion in q_1 is linear with the angle to within less than 0.5%. The angular motion is accomplished through a stepper-motor mechanically connected to the scraper-arm in such a way that the motor pivots through the same angle as the scraper. Hence, as the motor pulls itself toward (or pushes itself away from) the pivot block into which its threaded shaft runs, it changes the scraper-arm angle linearly (to within 0.5%) with the distance it pulls or pushes itself. Hence, the motion of the scraper is linearly related to the motion of the motor, which is in turn linearly related to the number of steps taken.

5.3.3 Scraper Calibration and Sources of Error

Two limit switches serve to limit the range of the motion, and additionally provide calibration of the range of motion, which is such that the outer edge of the scraper goes from $q_1 = 8.55\text{cm}$ to 16.9cm (these values are believed good to within $\pm 0.1\text{ cm}$). Since the stepper motor takes 11180 ± 20 steps in going continuously (i.e., without pause) from one limit to the other, the position of the outer edge is seen to be

$$q_1(N_s) = q_1(0) + N_s C_s \quad (5.23)$$

where N_s is the number of steps taken from the inner limit switch (where the scraper is closest to the alpha-magnet front plate), $q_1(0) = 8.55 \pm 0.1\text{cm}$, and $C_s = (7.42 \pm 0.13) \times 10^{-4}\text{ cm/step}$. Since the stepper is accurate to within 100 steps even for a long sequence of short bursts of steps such as are needed for a spectrum measurement, the uncertainty in $q_1(N_s)$ is primarily due to uncertainty in the knowledge of $q_1(0)$ and C_s . In general, the uncertainty in q_1 is given by

$$\sigma_{q_1}(\text{cm}) = \frac{1}{10} \sqrt{1 + \left(\frac{N_s}{1000} \right)^2 0.13^2} \quad (5.24)$$

If the gradient is g , then the momentum being filtered at N_s steps is

$$p(N_s) = g \left(\frac{q_1(N_s)}{75.05} \right) \quad (5.25)$$

Propagating uncertainties through this equation gives

$$\frac{\sigma_p}{p} = \sqrt{\left(\frac{\sigma_g}{g} \right)^2 + \frac{N_s^2 \sigma_{C_s}^2 + \sigma_{q_{10}}^2}{(q_{10} + C_s N_s)^2}}. \quad (5.26)$$

The uncertainty in the gradient, σ_g , is a result of uncertainty in the alpha-magnet current, and is at most $\pm 1\%$. This is as large as it is because the power supply does not have a precision shunt, and I had to rely on the front-panel meter, which has a resolution of 1 A. Since the excitation curve for the magnet was taken using the same meter, there is no concern about the absolute accuracy of the meter. The alpha-magnet is seldom used at gradients below 100 G/cm, which means the current is always greater than 50 A. Gradients of 150-250 G/cm are more typical.

The maximum fractional uncertainty in the momentum will occur either at $N_s = 0$ or $N_s = (N_s)_{\max}$, depending on whether the fractional uncertainty in q_{10} or C_s is larger, respectively. Since it is the fractional uncertainty in q_{10} that is larger, one sees that the maximum value of σ_p/p is 1.6%. Rather than propagate errors through the analysis of every spectrum, I will simply take this value as the uncertainty in any momentum measurement. This uncertainty is not the same as the momentum resolution of the momentum filter, which is determined solely by the mono-energetic beam size and the dispersion, as discussed in the last section.

A check of the accuracy of the momentum measurements can be made by taking spectra at several alpha-magnet gradients for the same beam conditions. One expects that if the calibration of the alpha-magnet gradient (vs driving current) and the scraper are correct, then these spectra should be very nearly the same. In fact, the calibrations were checked and then corrected by doing such an experiment. The weak link in the spectrum measurements is the calibration of the alpha-scraper position. As I discussed above, the scraper is on the end of a long arm, which is moved by means of a stepper motor attached to a much shorter arm. Hence, small motions of the short arm produce much larger motions of the scraper, with an amplification

factor of about 4.6. Any accidental movement of the limit switches or bending of the copper cooling tubes that act as the scraper arm would affect q_{10} , leaving C_s unchanged (to a good approximation).

Data taken at several alpha-magnet gradients show very clearly that there is a change in the scraper calibration compared to that done in before installation of the alpha-magnet vacuum chamber. Spectra were taken at fixed beam conditions (i.e., at fixed beam current and RF power) for a series of gradients between 170 and 340 G/cm. The peaks of these spectra were found by analysing the data as discussed above. Figure 5.9 shows the inferred momenta of the spectral peak for the $q_{10} = 8.1\text{cm}$ (the “nominal” value from the pre-installation calibration) and for $q_{10} = 8.55\text{cm}$ (the corrected value). The data reduced with the corrected value of q_{10} are clearly much more consistent than those reduced with the nominal value. I found that I could not bring the inferred momenta of the spectral peaks into agreement by varying C_s , nor could I do so by using a hypothetical gradient miscalibration factor (i.e., $g \rightarrow f \cdot g$, with f a constant).

The data points for the highest gradient are apparently spurious, perhaps because the small trajectories produced by such a strong gradient never go outside the region that is strongly influenced by the hole-induced gradient errors (see Chapter 3). Since the spatial region over which the hole-induced errors strongly effect the field is constant as the gradient varies, one would expect that such errors would have the most effect for the strongest gradients.

Note that, in addition to correcting the spread in the inferred momentum peaks, changing q_{10} from its nominal value increases the inferred momentum of the peaks by about 8%. This shift is consistent with other observations, namely, that if the nominal calibration was used to determine the momentum, then the quadrupoles appeared to be about 12% weaker than would have been expected based on simulations; using the corrected calibration of the scraper reduces this discrepancy to about 4%.

As for the source of the calibration error, there is a strong suspicion that the copper cooling tubes that support the scraper were bent during connection to the water supply system; this may be the source of the offset. The offset might also be a result of rough handling during transport and installation; the scraper arm oscillates quite readily, and hence may have been bent as a result of a resonant oscillation

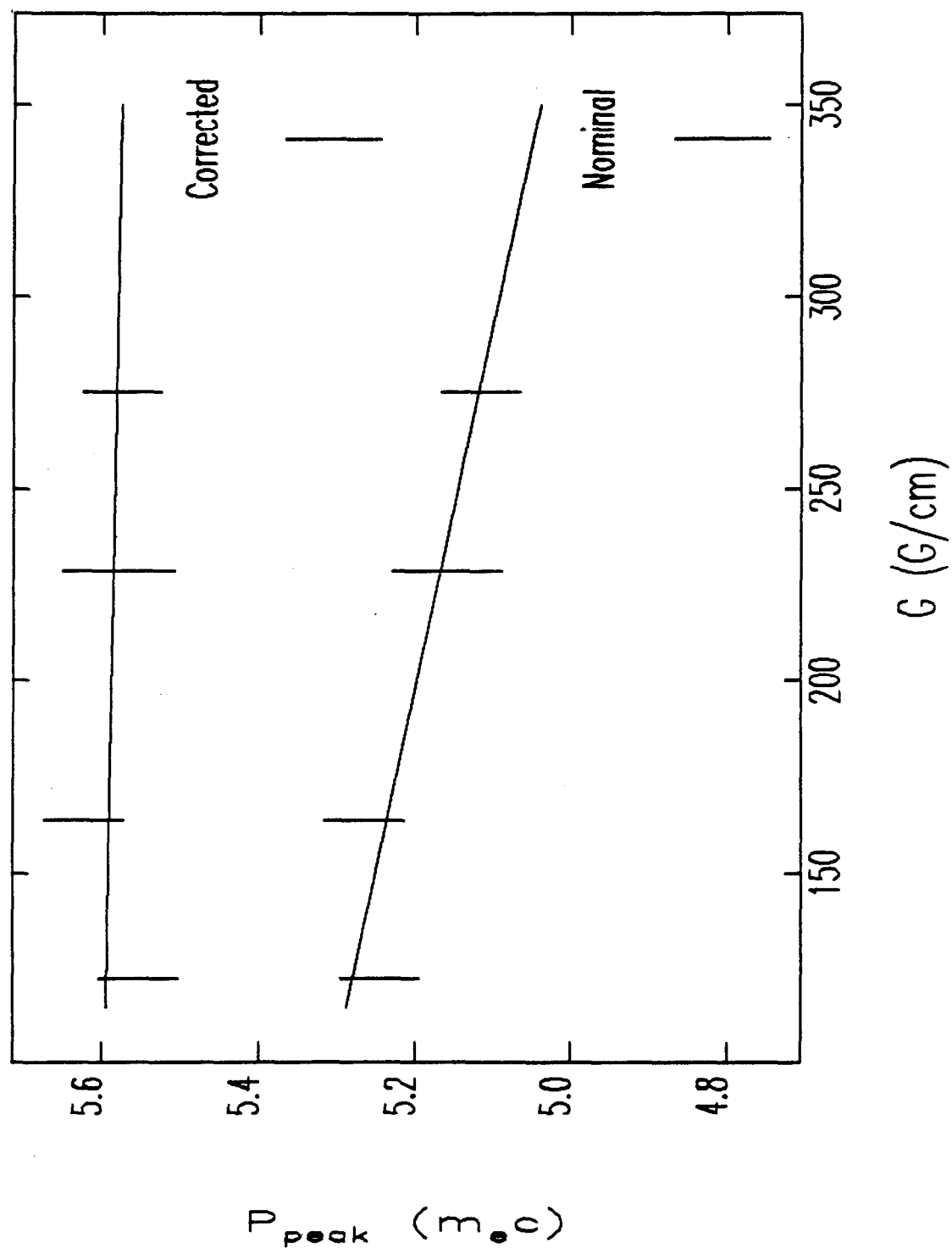


Figure 5.9: Inferred Positions of Spectral Peak for Nominal and Corrected Scraper Calibration

excited during transport.

5.3.4 Measurement of Beam Power

In addition to the momentum distribution of the beam, the data collected by `spect3` can be used to find the beam power transmitted through the alpha-magnet. This is useful in estimating the cavity electric field level, as I will discuss later in this section.

Let I_{tot} be the total current exiting the alpha-magnet, so that the number of electrons in the interval $[p, p + dp]$ passing out of the alpha-magnet during time Δt (where Δt is large compared to the RF period) is

$$dN(p, \Delta t) = \frac{I_{\text{tot}} \Delta t}{e} \rho_p(p) dp. \quad (5.27)$$

The kinetic energy of a single electron is given by $m_e c^2 (\gamma - 1)$, and so the total kinetic energy of the particles exiting the alpha-magnet during Δt is

$$\Delta U = \int_0^{p_{\text{max}}} m_e c^2 (\sqrt{p^2 + 1} - 1) \frac{dN(p, \Delta t)}{dp} dp. \quad (5.28)$$

Hence, the transmitted beam power is

$$P_{\text{beam}} = \frac{\Delta U}{\Delta t} = I_{\text{tot}} \frac{m_e c^2}{e} \int_0^{p_{\text{max}}} (\sqrt{p^2 + 1} - 1) \rho_p(p) dp. \quad (5.29)$$

5.3.5 Experimental Results

I performed two series of spectrum measurements designed to test the validity of simulations of the gun and GTL. For the first series, I took data while varying the RF power for constant cathode filament power, at low gun current ($I_{\text{GT1}} < 100\text{mA}$). For each RF power level, I recorded forward and reflected power waveforms and GT1 and GT2 waveforms. In addition, the program `spect3` was run in order to collect data necessary for determining the spectral distribution and transmitted beam power. For the second series, the RF power was held constant while varying the cathode filament power, and hence the gun current.

Simulation Tests of the Lattice

All relevant magnetic elements (i.e., quadrupoles Q1 through Q3 and the alpha-magnet) were kept at the same settings throughout both sets of measurements. While better spectra would have been obtained for the lower-momentum beams had the lattice momentum (i.e., the central momentum the lattice is designed to transport) been varied to match the beam momentum, this would have greatly increased the time needed for the experiment. It would have been necessary to measure the beam momentum for each RF power level or cathode filament power level, then turn off the RF to allow standardization of the magnets, ramp them to the proper central momentum, turn the RF back on and wait for the gun to equilibrate, and only then take the final scans. This would roughly have tripled the time required for each measurement, and since experimental time was short, I elected instead to use a lattice with a fairly weak alpha-magnet (170 G/cm) and relatively gentle quadrupole settings, and therefore relatively large momentum acceptance.

Simulations with *elegant* verify that this lattice provides reasonably accurate momentum spectra, and, in particular, accurate determination of the position of the spectral peak, for a wide range of beam momenta, for a fixed lattice momentum. *elegant* includes alpha-magnets with moveable inner and outer scrapers in the vertical midplane, which idealizes the experimental situation. For the simulations, I placed the outer scraper at $q_1 = 20$ cm, which is the position of the outer vacuum chamber wall, and directed the program to vary the inner scraper from $q_1 = 8.55$ cm to $q_1 = 17.05$ cm, in 1 mm steps (the experiments used 1mm steps also). The simulations ended at the position of toroid GT2, and included all beam apertures. The output from *elegant* was then post-processed by another program (*alpha_spect*) that is nearly identical to the program (*spect_proc*) used to process experimental data collected with *spect3* (the only significant difference is the data format the programs accept). In this way, I am able to make valid comparisons of simulation and experiment.

Figure 5.10 shows the results of two sets of *elegant* simulations, performed using initial particle distributions generated by *rfgun* for E_{p2} between 50 MV/m and 90 MV/m. (Note that, as always, the areas under the spectral distributions are normalized to unity.) The first set included transverse dynamics to second order, while for

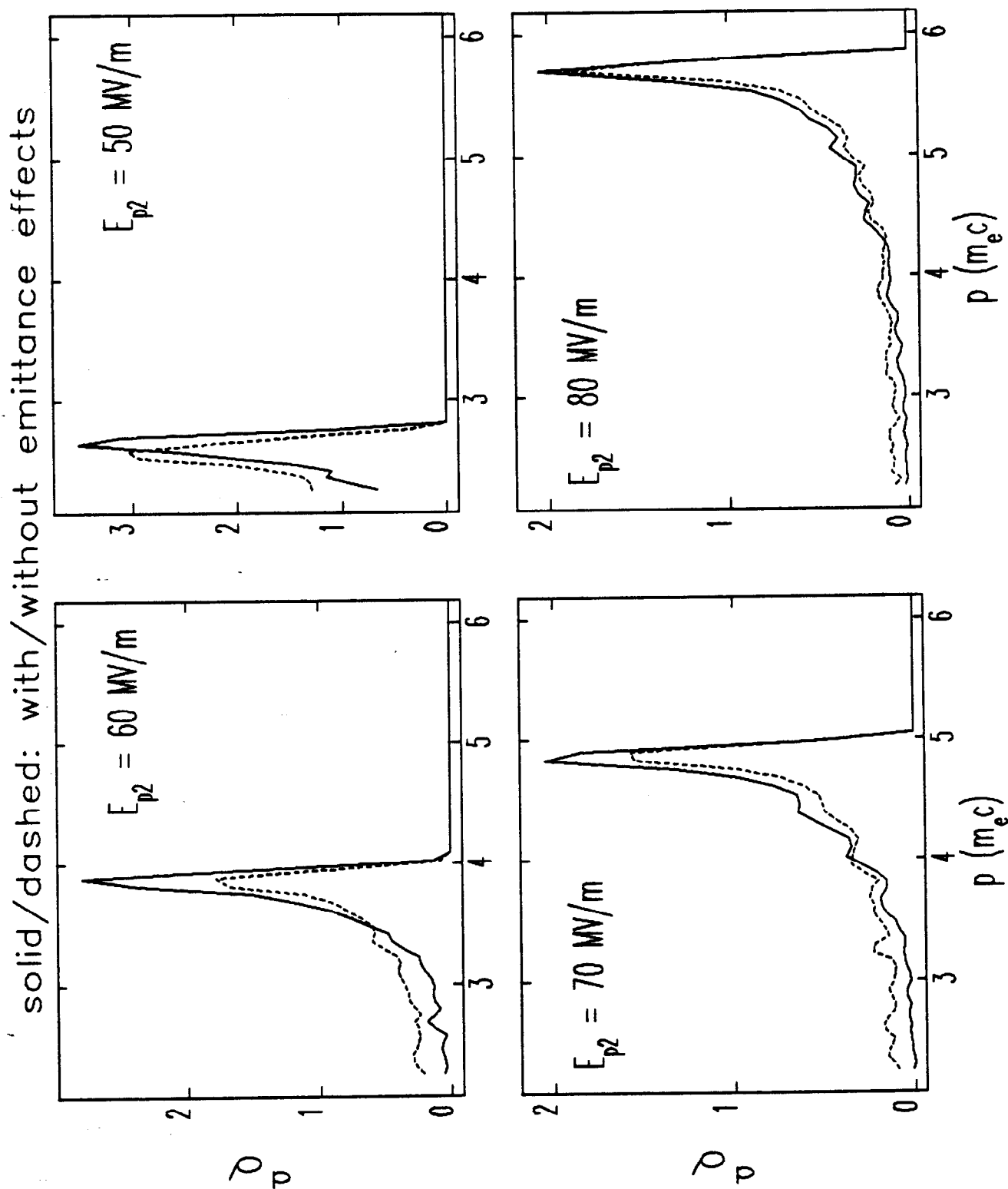


Figure 5.10: elegant-Simulated Spectrum Measurements for Various E_{p2} , Using rfgun-Generated Initial Particle Distributions

the second set I directed *elegant* to set all transverse coordinates to zero (i.e., $\epsilon \rightarrow 0$) before tracking. In both cases, the alpha-magnet was simulated to third order, with the expansion being done about the median momentum of the initial particle distribution. It is not a foregone conclusion that the results for the two cases should be the same. First, for $\epsilon \neq 0$, the momentum resolution of the system must be expected to degrade as the momentum of the highest-momentum particles being intercepted by the scraper becomes significantly less than the central momentum of the beamline (for which the matching for good momentum resolution was done). Second, the simulations with $\epsilon \rightarrow 0$ will not include the effects of apertures in the beamline, which will cause particle losses before and after the alpha-magnet.

One sees from the Figure that for the higher values of E_{p2} , the spectral distributions for the two sets of simulations are quite similar, while for the lower values of E_{p2} there are significant differences. For the $\epsilon \rightarrow 0$ simulations, the spectra include more low-momentum particles, indicating that in the simulations including transverse dynamics, low-momentum particles are being lost between the gun and alpha-magnet (or even after the alpha-magnet but before GT2). This is because the low-momentum particles are over-focused by the quadrupoles (which are optimized for higher momenta), and hence get scraped off on beamline apertures. Similar results are obtained when this comparison is done with MASK-generated initial particle distributions.

The conclusion is that for a valid comparison of experimentally-measured spectral distributions and predictions, the predictions must take the form of a simulation of the actual measurement. That is, one cannot simply compare the measured spectral distribution to the predicted spectral distribution at the gun exit. However, from Figure 5.10 also shows that the *positions* of the spectral peaks are quite close for the two cases, with a definite difference appearing only for $E_{p2} = 50\text{MV/m}$. Hence, an experimentally-determined momentum peak at $p \geq 3m_e c$ can be assumed to be at the very close to the position of the spectral distribution of the beam from the gun; this conclusion will help to simplify some of the analysis that follows.

Comparison of Measured and Simulated Spectra

Figure 5.11 shows representative spectral distributions from the first series of measurements. The forward RF power was varied between 2.6 MW and 1.3 MW. Though

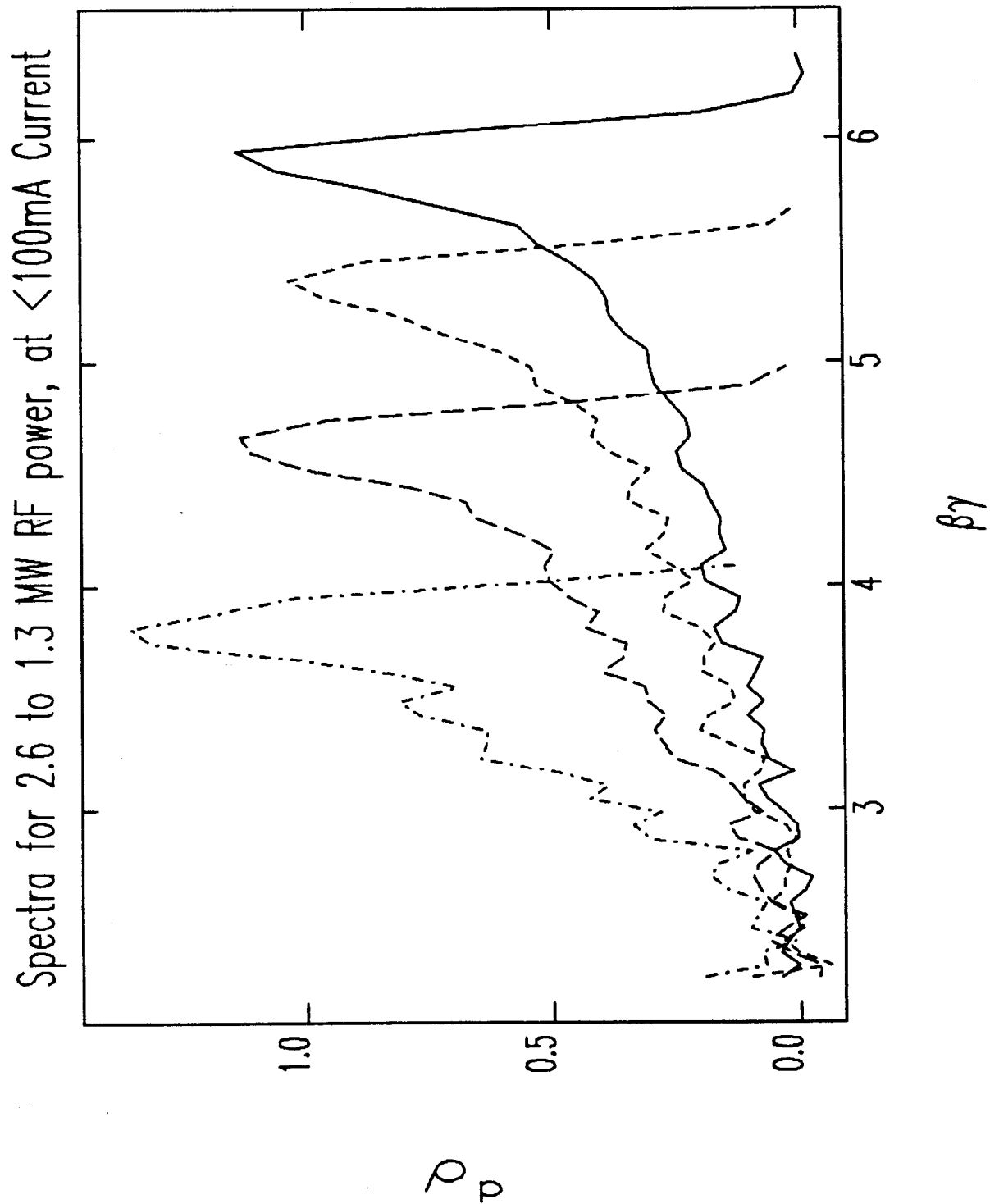


Figure 5.11: Experimentally-Measured Spectral Distributions at Low Current for 1.3 to 2.6 MW Forward Power

the cathode filament power was kept fixed, the beam current varied between 100 mA and 50 mA (respectively) as a natural result of the different cavity fields that prevail at different RF power levels. One sees that these are similar to the simulated spectra shown in Figure 5.10, but noticeably broader.

Better agreement between experiment and simulation is obtained when MASK-generated initial particle distributions are used, as seen from Figure 5.12. The MASK runs used for these simulations were done with very small current densities, so that no space-charge effects are present. Note that the horizontal scale is the same as that used in Figure 5.11. (I did not attempt to match the positions of the peaks between the simulations and the experiments, since this would have required additional MASK runs with little gained.)

In order to further investigate the issue of the broadness of the momentum peaks, I used the results of the *elegant*/*rfgun* simulations just described (for $\epsilon \neq 0$), along with additional simulations for MASK-generated initial particle distributions. I computed the full-width-at-half-maximum (FWHM) for the spectral peak from every simulation. The results are displayed in Figure 5.13, where the FWHM is plotted against the position of the spectral peak. The results of the same analysis for the experimental data is shown as well.

It is clear from this Figure that *rfgun* seriously underestimates the broadness of the spectrum. This was discussed in Chapter 2, as well, where I pointed out the differences in the spectral distributions predicted by *rfgun* and MASK. The fact that the MASK results correspond more closely to experiment lends support to the conclusion I drew in Chapter 2, namely, that the off-axis expansion used by *rfgun* is of too low an order to accurately model the important non-linear fields near the cathode. Note that the differences persist even for MASK runs done with $J = 0$ (i.e., without space-charge), implying that the difference is not a result of the fact that *rfgun* does not include space-charge effects.

Figure 5.13 also indicates that, according to the simulations done with MASK-generated distributions, it should be possible to detect current-related (i.e., space-charge induced) broadening of the spectral peak. Indeed, there seems to be some difference between the experimental points for variable RF power (done at < 100 mA) and variable filament power (where in excess of 300 mA was used in some cases),

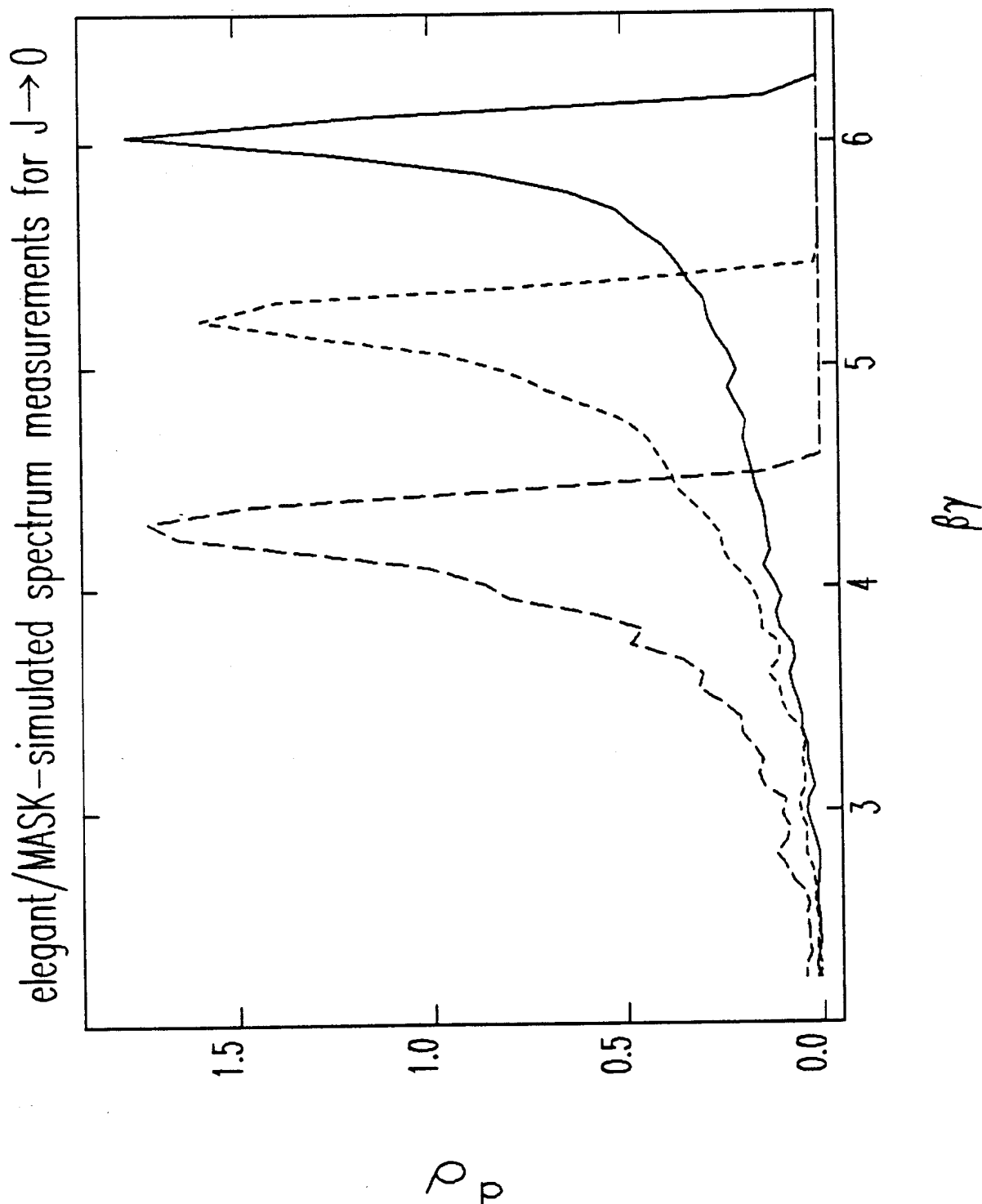


Figure 5.12: **elegant**-Simulated Spectral Distribution Measurements for MASK-Generated $J \rightarrow 0$ Initial Particle Distributions

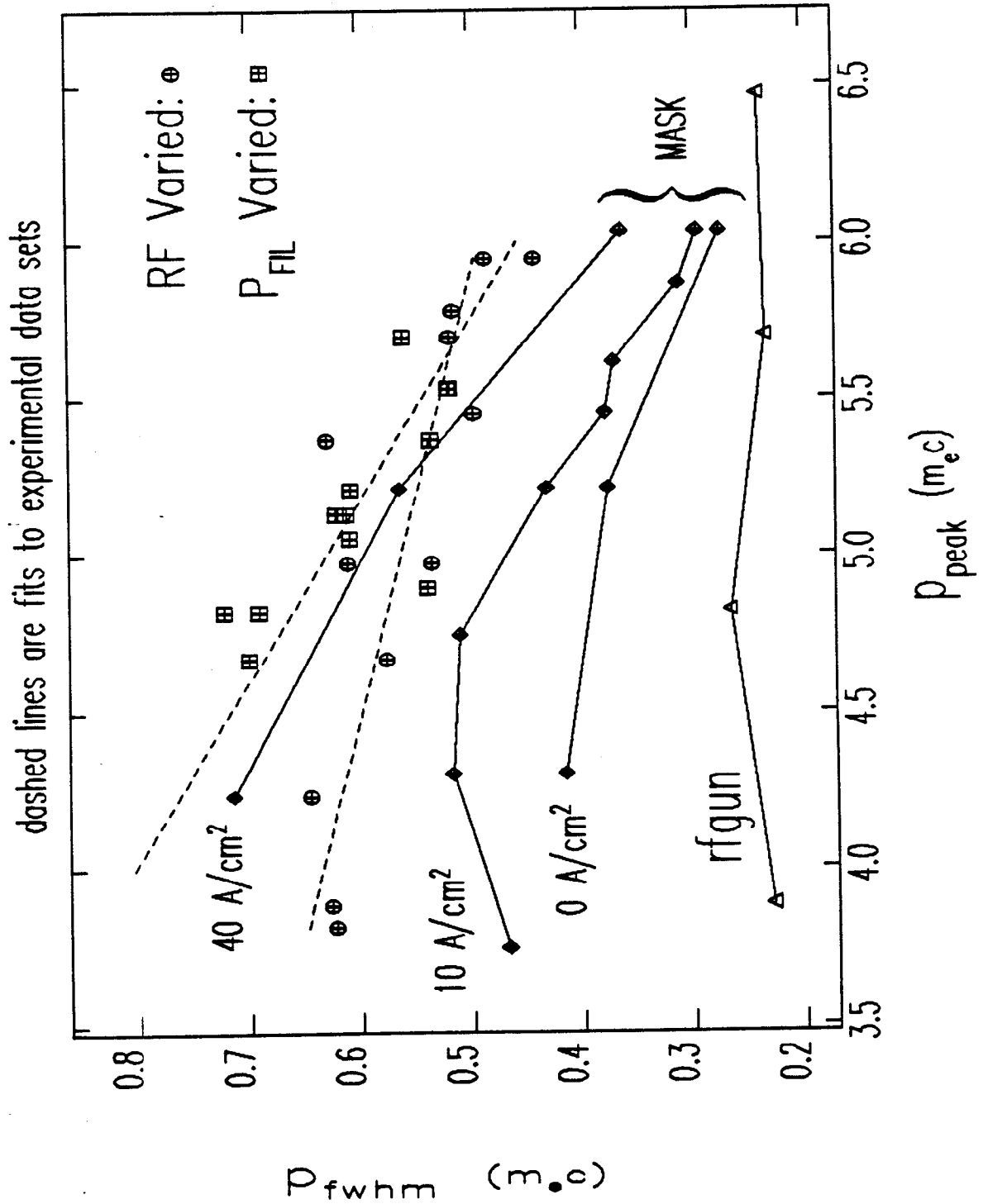


Figure 5.13: FWHM of the Momentum Peak from Experiments and from Simulated Experiments with *elegant*, *rfgun*, and MASK

in that the slope of p_{fwhm} versus p_{peak} is greater in magnitude for the latter set of data than for the former. The comparison of the two series of experimental points is unclear however, in that (unlike the MASK runs) the current density (i.e., the filament power) was varied in one set.

A clearer measurement of the effect of current density on the broadness of the spectrum could have been done by taking two data sets versus RF power at two different filament power levels. If one runs at sufficiently low currents, then the only difference between two such data sets would have been the cathode current density (running at lower currents is required in order to prevent back-bombardment from heating the cathode and thus making the current density vary with RF power). This experiment was, however, not carried out.

Of course, the current density could be inferred for each of the experimental measurements based on the momentum, the current seen at GT1, and simulations of beam-losses in between the gun and GT1. However, this is likely to be very uncertain, for reasons to be seen presently. Still, it is interesting to see how the current density can be estimated.

Inferring the Current Density

Figures 5.14 and 5.15 show additional data from the two series of measurements. While this data is not directly useful for comparison with simulations, it is useful in that it gives an indication of the quality of the measurements, in terms of the reproducibility and smoothness of the dependence of the various quantities on the varied quantity. (I chose I_1 as the independent variable for the second series because it is more physically meaningful than the cathode filament power.)

Returning now to the issue of inferring the current density, recall that in Chapter 2, I used the effective cathode area,

$$A_{\text{eff}} = \frac{I_{\text{gun-exit}}}{J}, \quad (5.30)$$

to indicate the efficiency with which charge is extracted from the gun. Similarly, I now define an effective cathode area for transmission to GT1:

$$A_{\text{GT1}} = \frac{I_{\text{GT1}}}{J}. \quad (5.31)$$

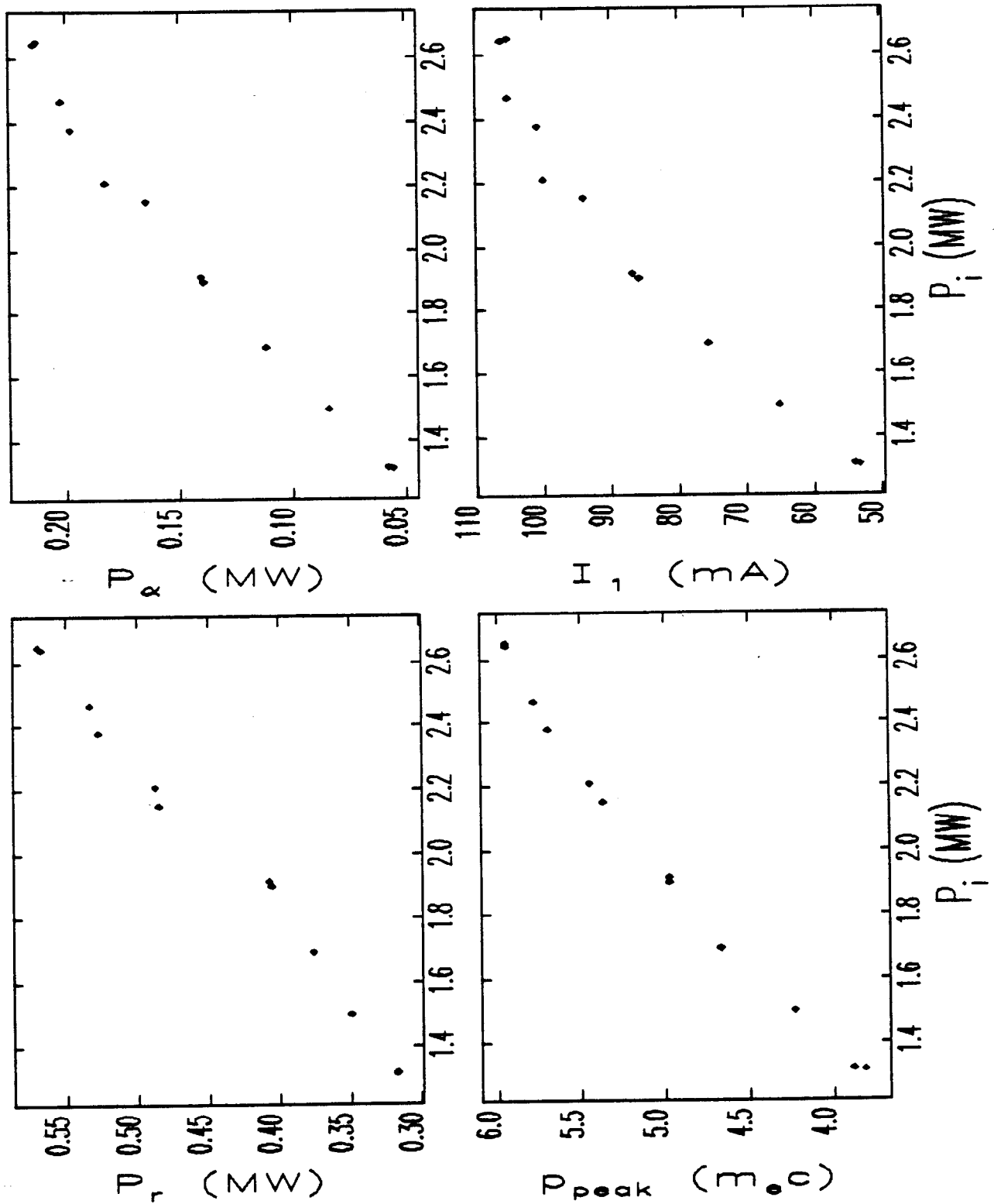


Figure 5.14: Selected Experimentally-Measured Parameters as a Function of Incident RF Power, for Constant Cathode Filament Power

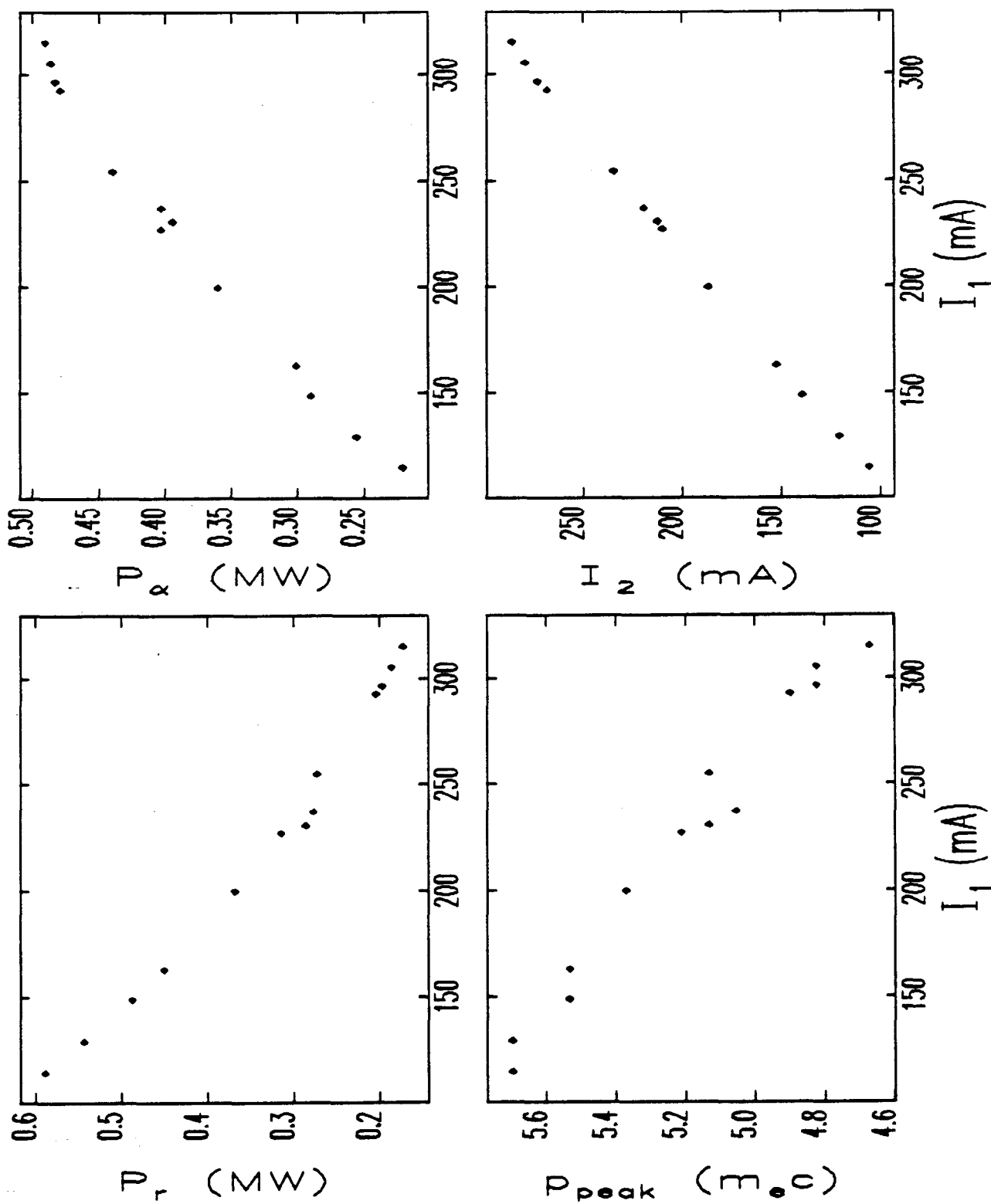


Figure 5.15: Selected Experimentally-Measured Parameters as a Function of GT1 Current, for Constant Incident RF Power

I_{GT1} is a function of the fields in the gun (which determine the beam momentum) and the GTL optics (including the effects of apertures). For a fixed optical configuration, one can parametrize I_{GT1} as a function of p_{peak} , the position of the spectral peak. (I_{GT1} is also a function of J through the effects of space-charge on the emittance and the momentum spectrum, and hence on the transport, but I shall ignore this for simplicity.) Equivalently, one may invert the relationship and calculate J from

$$J = \frac{I_{GT1}(p_{peak})}{A_{GT1}(p_{peak})}. \quad (5.32)$$

The experiments provide measurements of I_{GT1} versus p_{peak} , as shown in the Figures 5.14 and 5.15. $A_{GT1}(p_{peak})$ may be obtained from *elegant* simulations, and I have done this using MASK-generated initial particle distributions calculated for $J = 10 \text{ A/cm}^2$ (again, I'll ignore any dependence of the transport on J , which is acceptable since, as will be seen, J varies over a small range). The result is shown in Figure 5.16, along with the analogous result for transport to GT2. (I note in passing that these results *do not* indicate the best achievable transmission for the GTL, since the lattice was not matched to each momentum, as discussed above. It is not uncommon to obtain 90% transmission between GT1 and GT2 with a properly tuned lattice.)

Figure 5.17 shows the inferred current density for the experimental data shown in Figures 5.14 and 5.15. One sees that the current densities are apparently quite modest compared to 140 A/cm^2 , which is the upper limit for the cathode. As I will discuss presently, there is reason to believe that these results may underestimate the current density by perhaps a factor of two. Some indication that there may be a problem here is the fact that the current density clearly varies for the case of constant filament power, even though the current is low enough to make back-bombardment negligible. (I estimate that there is about 0.5 W of average back-bombardment power for 800 mA to GT1 and 2.6 MW RF, while the heater power is in the range of 9–11 W. Hence, for less than 100 mA, I expect the back-bombardment power to be less than 1% of the filament power.)

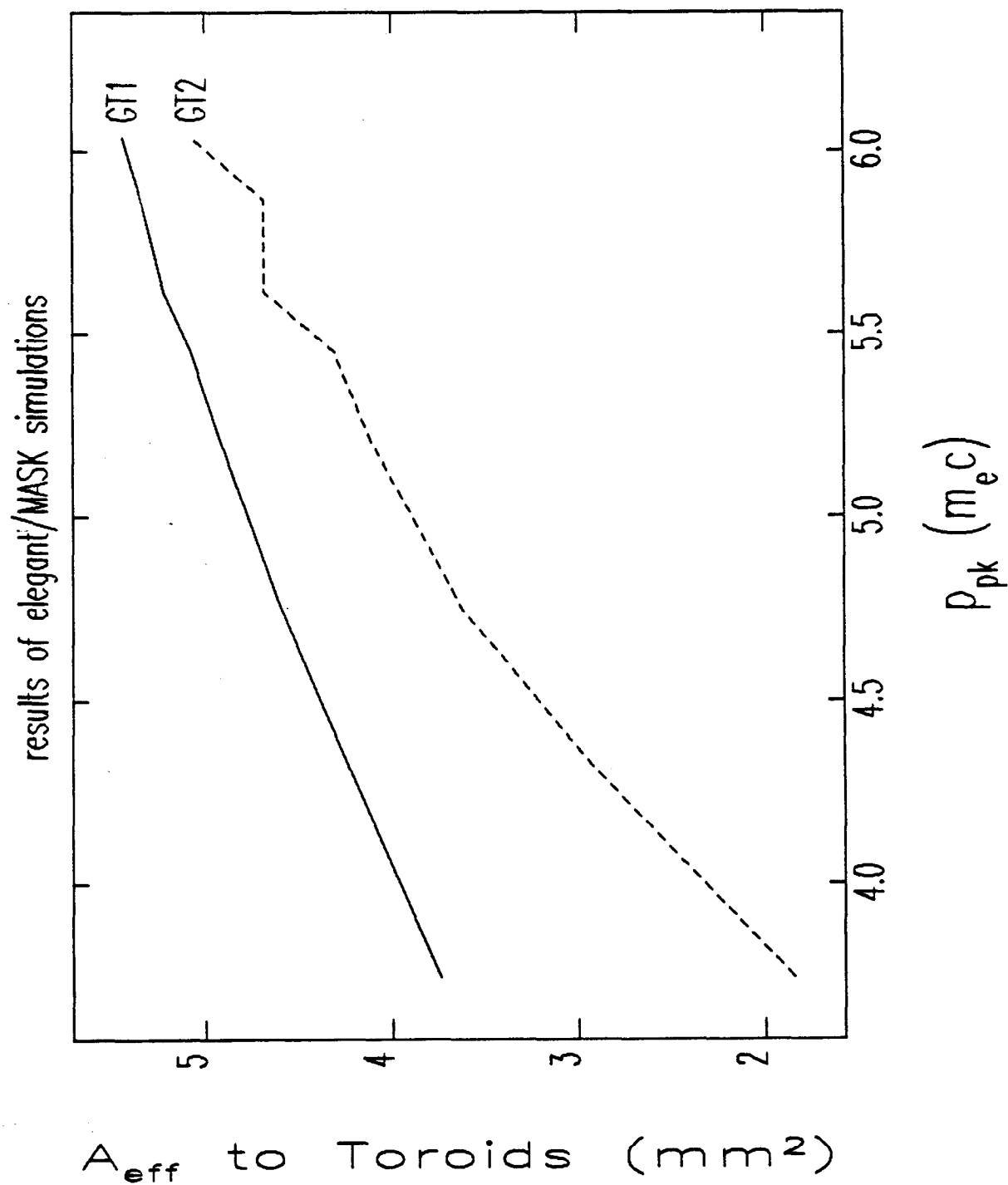


Figure 5.16: Effective Cathode Areas for Transmission of Current to GT1 and GT2, as a Function of the Momentum Peak, from *elegant*/MASK Simulations.

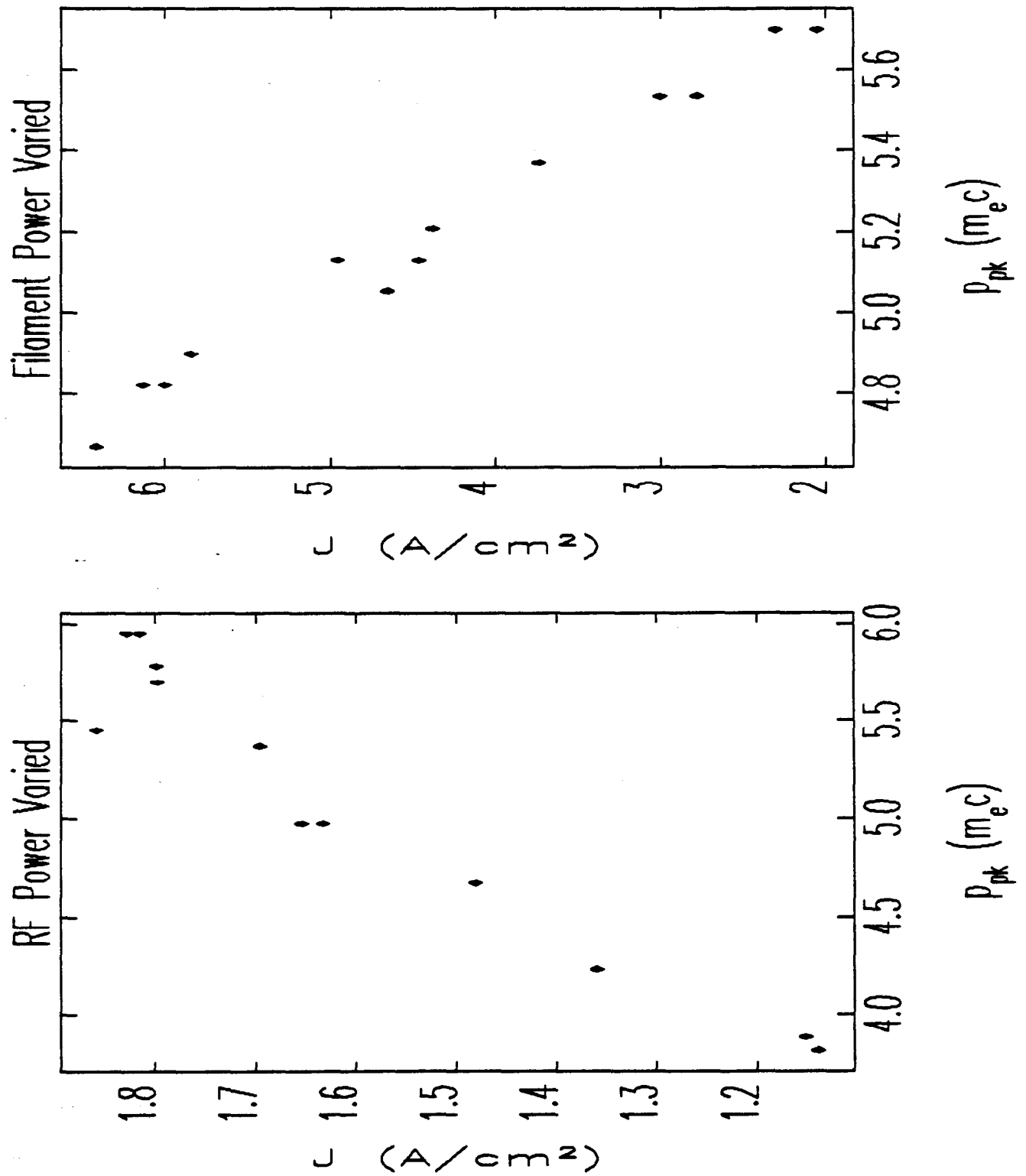


Figure 5.17: Current Density for Experiments, as Inferred from Experimental Data and Simulations

Inferring the Gun Field Level

In Chapter 2, I gave predictions of how the beam momentum is expected to depend on the fields in the cavity, which I parametrized in terms of the peak on-axis field amplitude, E_{p2} . In order to check these predictions against experiment, it is necessary to measure or deduce the E_{p2} levels during the experiments. Since there are no field probes in the gun cavity, I have had to rely on the relationship between E_{p2} and the power dissipated in the cavity walls

$$E_{p2} = K_f \sqrt{P_w}, \quad (5.33)$$

where the nominal value of K_f (obtained from a combination of cold-test measurements and simulation results, as discussed in Chapter 2), is $70.5 \text{ MV/m}/\sqrt{\text{MW}}$.

To see how to make use of this, note that conservation of energy dictates that

$$\frac{dU_s}{dt} = P_f - P_r - P_w - P_p, \quad (5.34)$$

where U_s is the energy stored in the cavity fields, P_w is the RF power dissipated in the cavity walls, P_f is the incident RF power, P_r is the reflected RF power, and P_p is the power into particles. P_p includes power into any particles, whether they exit the gun or impact the cathode or the cavity walls. At equilibrium, the cavity fields are constant, and hence so is U_s . Therefore

$$P_w = P_f - P_r - P_p. \quad (5.35)$$

Experimentally, P_f and P_r are obtained from calibrated RF detector diodes, which produce a voltage signal that can be related to the applied RF power.

P_p must be obtained by a more circuitous route, since there is no way to measure the power that goes into particles hitting the cathode, the cavity walls, or apertures between the gun and the alpha-magnet. What can be measured, as discussed above, is the beam power transmitted through the alpha-magnet. To relate this to P_p , I have used simulations to model the particle losses in the gun and between the gun and alpha-magnet. For the latter simulations, I used `rfgun`-generated particle distributions as input to `elegant`, which tracked the particles through the GTL lattice using the beam-optics used in the actual experiment (with the quadrupole model

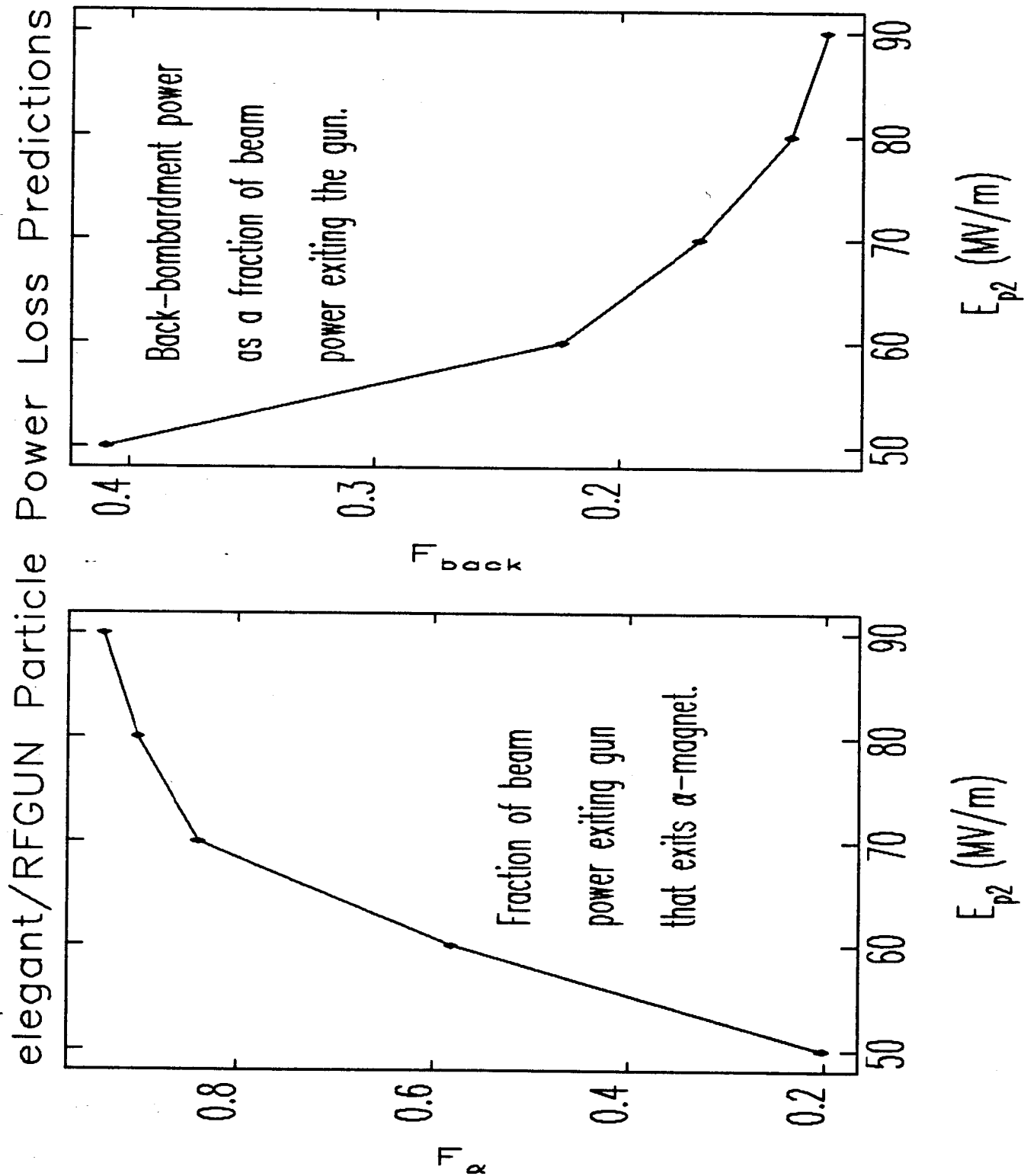


Figure 5.18: Particle Power Loss Parameters as a Function of the Spectral Peak

adjusted as per the previous section). I did such simulations for E_{p2} between 50 and 90 MV/m. (Essentially the same results are obtained using MASK-generated initial particle distributions for $J=10$ A/cm².) These simulations allowed me to deduce the ratio of initial beam power (i.e., the power in the particles that exit the gun) to transmitted beam power as a function of E_{p2} , or, equivalently and more usefully, as a function of p_{peak} . Figure 5.18 shows the results of these calculations, which I will represent formally as

$$P_{\text{ib}} = \frac{P_{\alpha}}{F_{\alpha}(p_{\text{peak}})}, \quad (5.36)$$

where P_{ib} is the initial beam power, P_{α} is the beam power transmitted through the alpha-magnet, and F_{α} is the fraction of the initial beam power that exits the alpha magnet.

Next, I used `rfgun` to simulate back-bombardment as a function of E_{p2} , allowing me to deduce the ratio of back-bombardment power to initial beam power as a function of the spectral peak:

$$P_{\text{back}} = P_{\text{ib}} F_{\text{back}}(p_{\text{peak}}). \quad (5.37)$$

These results are shown in Figure 5.18. Simulations with MASK and `rfgun` indicate that it is a good approximation to equate the beam power lost in the gun with the beam power lost by particles hitting the boundary at $z = 0$ (i.e., the plane of the cathode), and I will employ this approximation, so that

$$P_{\text{p}} = P_{\text{ib}} + P_{\text{back}}, \quad (5.38)$$

or

$$P_{\text{p}} = \frac{P_{\alpha}}{F_{\alpha}(p_{\text{peak}})} (1 + F_{\text{back}}(p_{\text{peak}})). \quad (5.39)$$

The quantities P_{f} , P_{r} , P_{α} , and p_{peak} can all be measured, and thus it is now possible to calculate the cavity wall power for the experiments, using

$$P_{\text{w}} = P_{\text{f}} - P_{\text{r}} - \frac{P_{\alpha}}{F_{\text{meas}}(p_{\text{peak}})}, \quad (5.40)$$

where

$$F_{\text{meas}}(p_{\text{peak}}) = \frac{F_{\alpha}(p_{\text{peak}})}{1 + F_{\text{back}}(p_{\text{peak}})} \quad (5.41)$$

is the fraction of the power going into particles that is actually measured (i.e., at the exit of the alpha-magnet). Equation (5.40) can then be used in equation (5.33) to find the peak, on-axis electric field for each RF power level used in the experiment.

Figure 5.19 shows the results of this analysis for the two sets of data. From the data at constant filament power, one might conclude that there was a calibration error in the RF power measurements or that K_f was in error. However, the data for variable filament power, where beam-loading is significant (and is indeed the cause of the variation of p_{peak}), show that the error is most likely to be in the calculation of F_{meas} . Figure 5.20 shows the results of repeating the analysis with $F_{\text{meas}} \rightarrow F_{\text{meas}}/1.47$ and $K_f = 66\text{MV/m}$, a combination that was found to bring both sets of data into reasonable agreement with simulation results. I found that I could not obtain a similar level of agreement for both data sets by modifying only K_f or by modifying only F_{meas} by a multiplicative constant. Hence, it would appear that the beam losses are considerably greater than predicted, and that the Q of the cavity (which is related to K_f) is lower than predicted.

Possible Explanations of Discrepancies

Several explanations of the higher-than-expected beam power losses are possible:

1. If the emittance is larger than predicted, then more particles would be lost on the apertures between the gun and alpha-magnet. In particular, there is a 2mm radius aperture constriction at the exit of the gun, designed to isolate the gun vacuum from the GTL vacuum. This is observed to be a significant source of radiation[81], suggesting that, contrary to expectations, significant beam power is lost here. Simulations predict that only about 10% of the beam power should be intercepted by this aperture.
2. Space-charge effects in the gun or GTL might alter the momentum spectrum sufficiently to falsify the beam-power-loss predictions. I do not believe this is the explanation, as the effect of space-charge on the position of the momentum peak is slight.

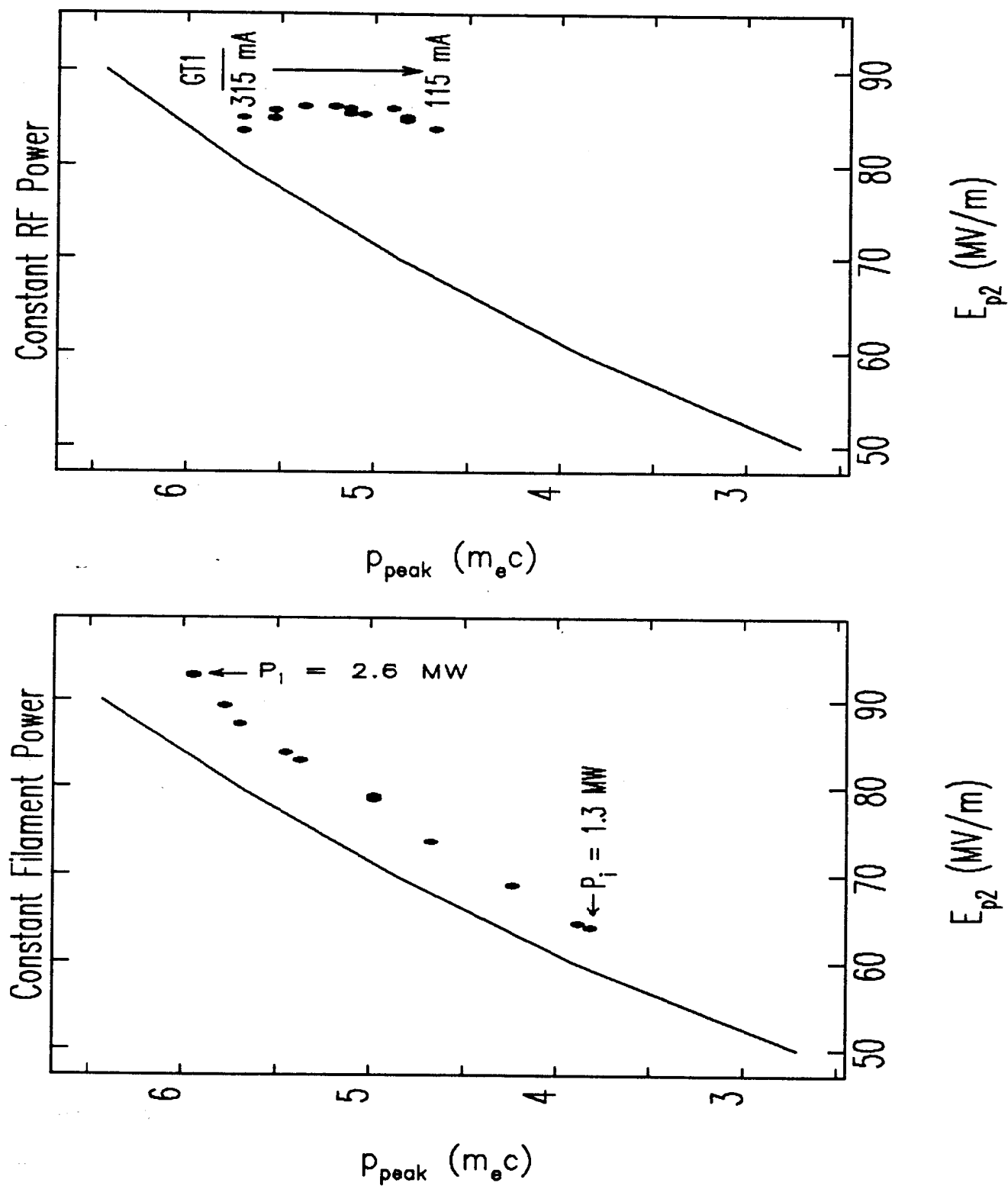


Figure 5.19: Spectral Peak as a Function of Inferred E_{p2} , for Constant Filament Power and Constant RF Power Series

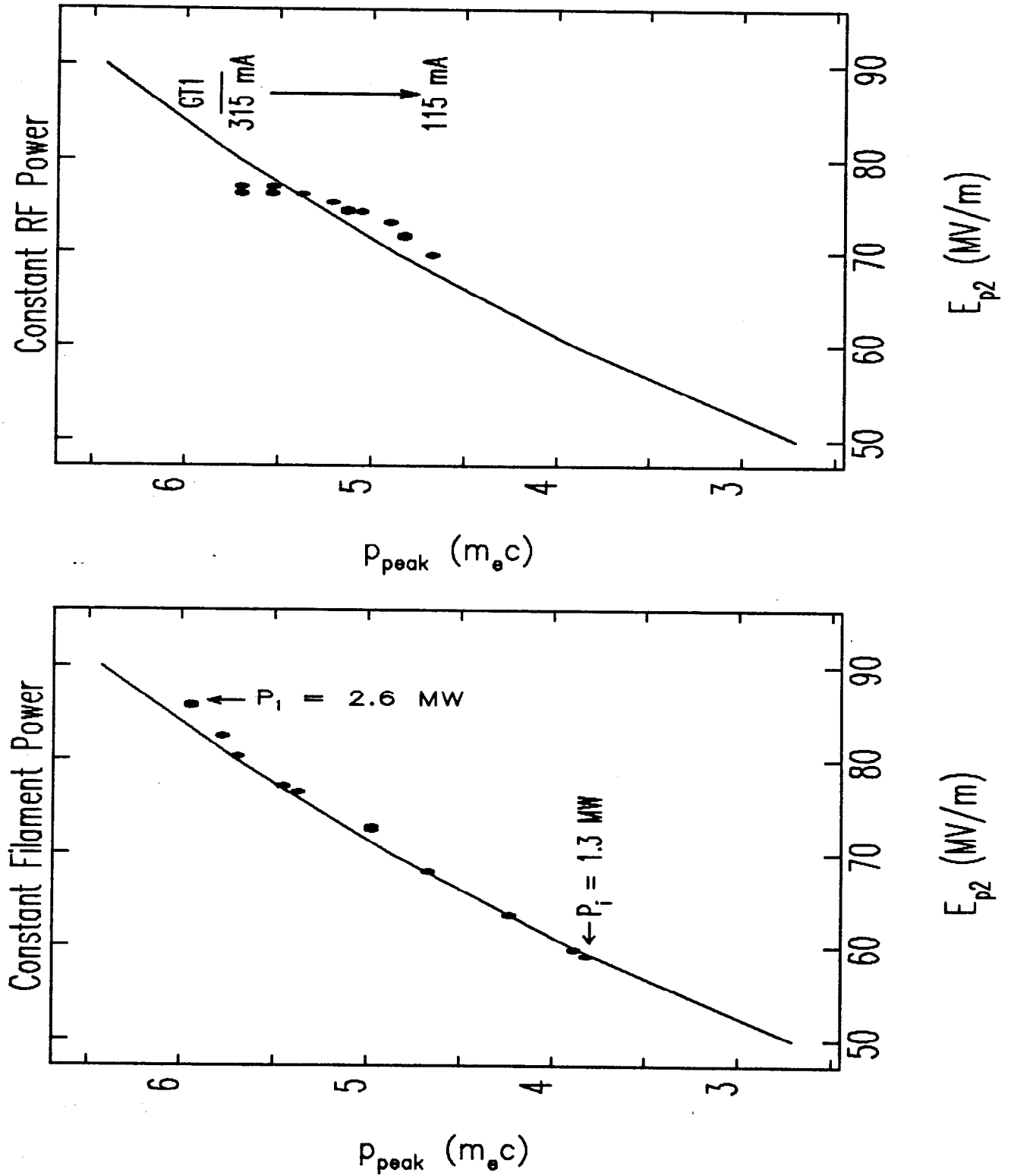


Figure 5.20: Spectral Peak as a Function of Corrected E_{p2} , for Constant Filament Power and Constant RF Power Series

3. Dark-current electrons or secondary electrons created by electrons hitting the cavity walls could be absorbing RF power, without contributing to the beam[82]. There is evidence that secondaries (or dark-current electrons) are present in significant quantities, in that shape of the initial part of the reflected power pulse is seen to be very unstable when there is no beam. This suggests that electrons are being emitted sporadically in sufficient quantities to load the cavity, though no observable beam reaches GT1. This sporadic emission appears to stabilize (i.e., become continuous) when the cathode is heated by the filament, suggesting that the addition of a primary beam brings about continuous emission of these useless electrons.
4. The estimation of K_f does not include losses in the side-coupling cavity, though clearly there must be some in actual operation if net power is to flow from the second on-axis cell to the first. This issue remains to be investigated.
5. Miscalibration of the reflected power diode could cause over-estimation of the amount of "left-over" power, and hence over-estimation of the amount of power that must have gone into the beam. I have made several tests of the calibrations of the forward and reflect power diodes:
 - (a) The combined diodes, loads, attenuators, and cabling for the two RF signals are identical to within 5%.
 - (b) Simultaneously sampled forward and reflected power waveforms as a function of the RF drive show that the dependence of the reflected power on the forward power is fairly linear, except at low power, where the secondary problem just mentioned has a serious effect on the reflected power and also where the forward RF power waveform began to change shape (a property of the particular klystron being used). Figure 5.21 shows the pulse-average forward power and various parameters of the reflected power pulse (pulse average, power level at the second peak, power level at equilibrium), as a function of the average forward power. Also shown is the peak forward power as a function of the pulse-average forward power, which provides a test of the accuracy of the experiment and the effect of distortion of the

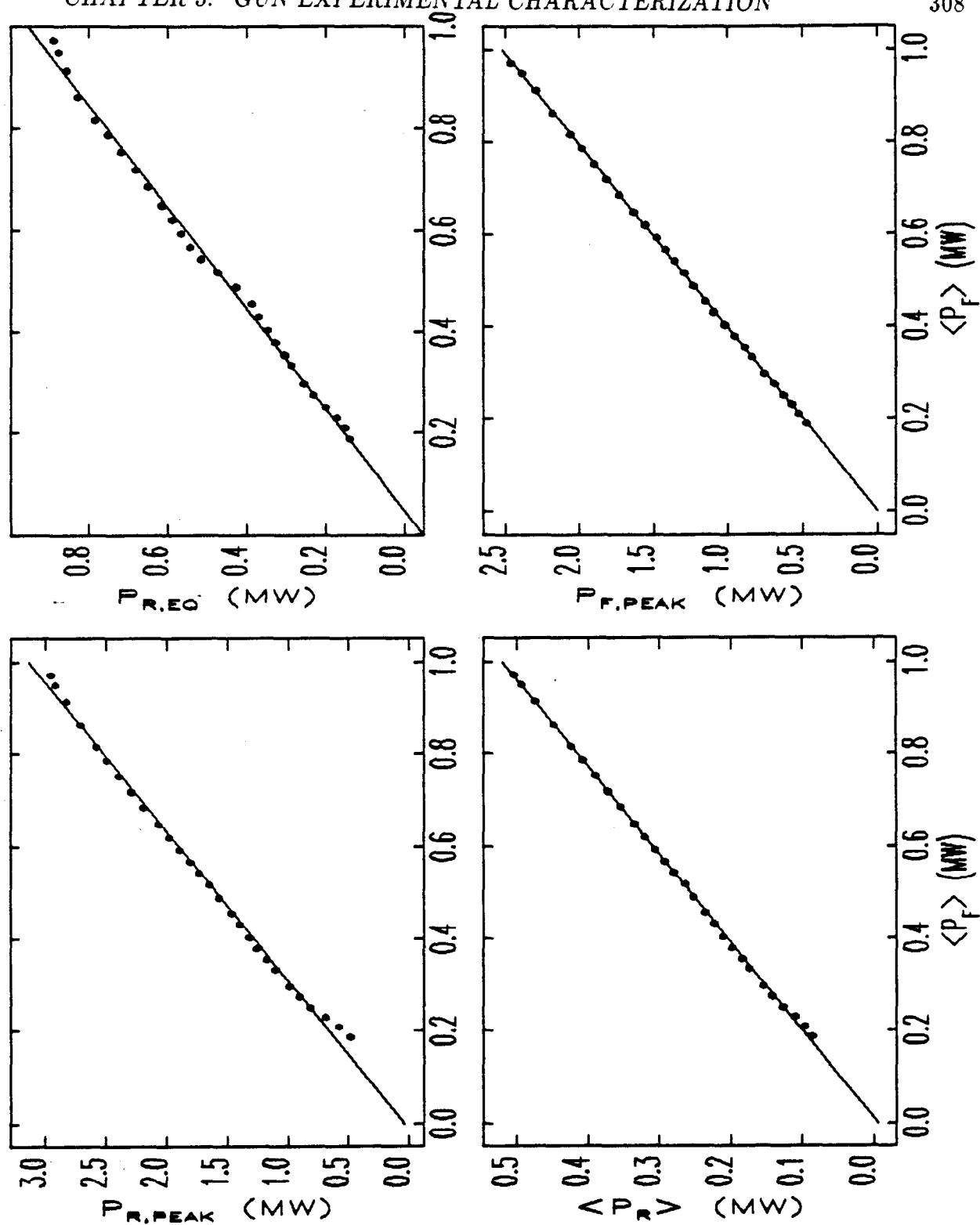


Figure 5.21: RF Calibration Test Results (See Text for Explanations)

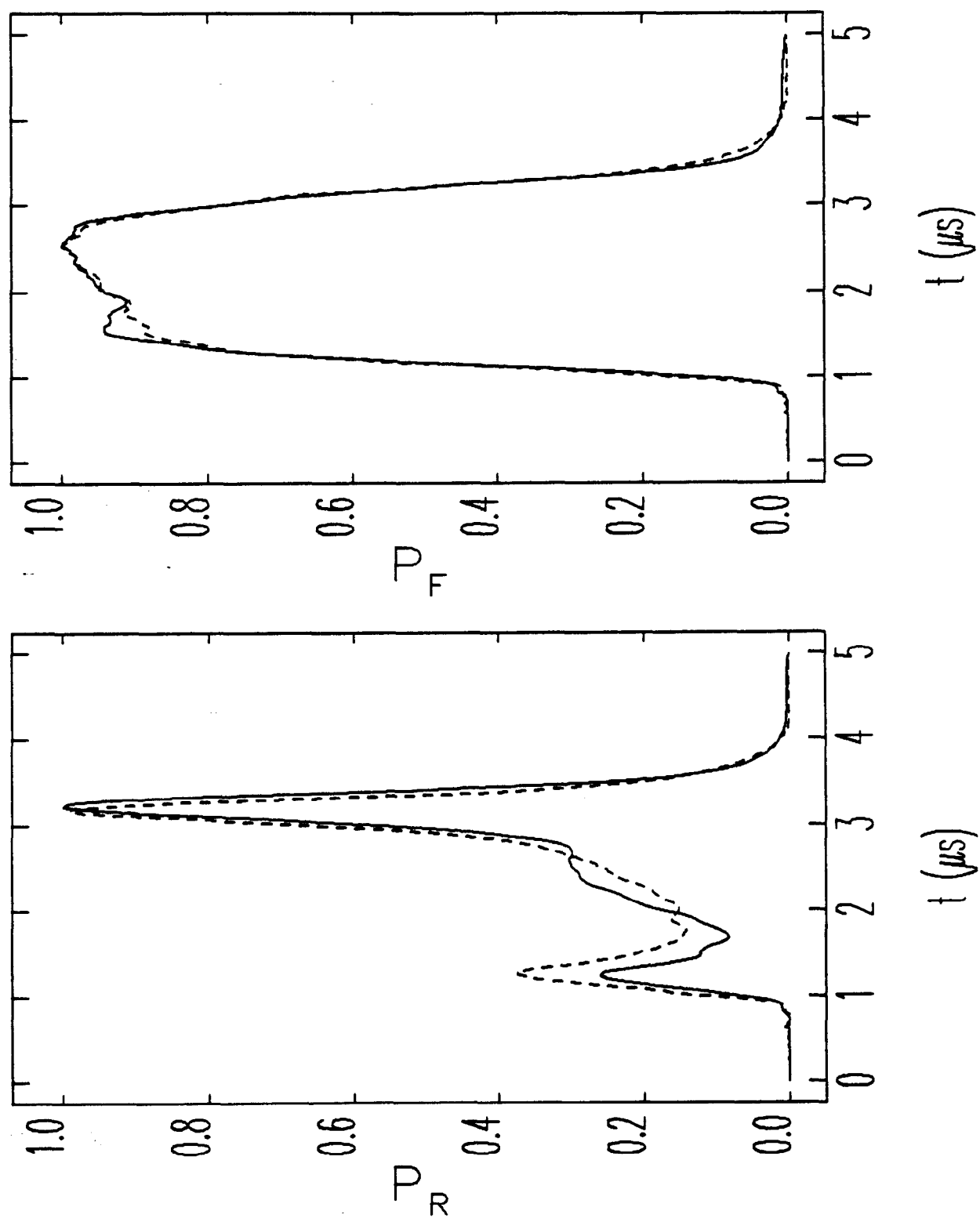


Figure 5.22: Normalized Forward and Reflected RF Power Waveforms for High and Low Forward Power

forward power pulse. For perfectly linearized detectors (and ignoring the other effects just mentioned), the data points should be scattered about the fit lines. The average reflected power appears quite linear in the average forward power, as does the peak forward power. The equilibrium reflected power appears to deviate at higher power levels, and to show some non-statistical wobble about the best-fit line; this is not surprising, since the shape of the reflected power pulse changes considerably over the range of forward power used. Normalized forward and reflected power waveforms for the highest and lowest power waveforms are shown in Figure 5.22.

One sees that the "emitted" power (at the second peak in the reflected power pulse) seems to deviate from linearity seriously in the lower ranges. This could explain some of the discrepancies seen above, in that the value of P_r used in equation (5.35) is quite small when the gun is heavily beam loaded, as was the case in the second of the two series of measurements. I have not attempted to correct for this effect, as recalibration of the forward and reflected power detection circuitry, starting with the directional couplers in the waveguide, would have required partial disassembly of the waveguide leading to the gun. It is clear that this is not the only problem, since it would not explain the discrepancies for the first series of measurements.

5.4 Emittance

The emittance, like the bunch length, is one of the most important parameters of the gun beam, for it helps to determine the brightness of the beam and hence its suitability for applications, such as FELs, requiring high brightness. In this section, I discuss the measurements I did of the emittance of the RF gun beam, and compare these with expectations based on simulations. Ideally, one would like to measure the emittance as a function of beam current and momentum over the entire range of gun operation. Unfortunately, this did not prove possible, and emittance data is only available for a rather limited range of gun operating conditions. The reasons for this will become clear as I proceed. It is necessary first to discuss the principle of the measurements.

A number of methods are used for measuring emittance; a review of some of the commonly-used methods appears in one of the references[11]. The method I employed made use of existing hardware, and involved the variation of a quadrupole upstream of a beam-profile measuring device, in this case a phosphorescent screen. By measuring the beam-size at the screen as a function of the quadrupole strength, one can deduce the RMS geometric emittance, defined by equations (5.42) and (5.43) below. (Note that when I use the word “emittance” in this section, I mean the RMS *geometric* emittance, unless otherwise stated.)

5.4.1 Principle of the Emittance Measurements

The theory of the method as it is usually developed (see, for example, [83]) assumes a mono-energetic beam described by the so-called Σ -matrix[84], which for the x-plane is

$$\Sigma = \begin{pmatrix} \Sigma_{11} & \Sigma_{12} \\ \Sigma_{21} & \Sigma_{22} \end{pmatrix} = \begin{pmatrix} x_{\text{rms}}^2 & \langle xx' \rangle \\ \langle x'x \rangle & x_{\text{rms}}'^2 \end{pmatrix}. \quad (5.42)$$

(Often, the beam is assumed to be gaussian, and hence completely characterized by the Σ -matrix, but this assumption is unnecessary, as discussed in subsection 5.4.6.) The RMS geometric emittance in terms of the Σ -matrix is simply

$$\epsilon = \sqrt{\det \Sigma} = \sqrt{\Sigma_{11}\Sigma_{22} - \Sigma_{12}^2}, \quad (5.43)$$

where I have used the fact that $\Sigma_{12} = \Sigma_{21}$.

An arbitrary Σ -matrix, Σ_0 , is transformed by a beamline with a transport matrix \mathbf{r} according to:

$$\Sigma_1 = \mathbf{r} \Sigma_0 \mathbf{r}^T, \quad (5.44)$$

where Σ_1 is the Σ -matrix at the end of the beamline and where \mathbf{r}^T is the transpose of \mathbf{r} . The spatial beam sigma at the end of the beamline—e.g., at a phosphorescent screen—is given by

$$\sigma = \sqrt{(\Sigma_1)_{11}}. \quad (5.45)$$

Clearly, σ is a function of the original Σ -matrix, Σ_0 , and the matrix \mathbf{r} , that is, of the initial beam phase-space and the properties of the beam-transport system between points 0 and 1.

In the experiment, one varies a beamline element—e.g., the strength of a quadrupole—thus obtaining a series of n matrices \mathbf{r}_i . Corresponding to each of these matrices is a spatial sigma, σ_i , at the end of the beamline. By explicitly writing out equations (5.44) and (5.45), one can express the results of the whole series as

$$\begin{pmatrix} \sigma_1^2 \\ \sigma_2^2 \\ \vdots \\ \sigma_n^2 \end{pmatrix} = \begin{pmatrix} r_{1,11}^2 & 2 \cdot r_{1,11} \cdot r_{1,12} & r_{1,12}^2 \\ r_{2,11}^2 & 2 \cdot r_{2,11} \cdot r_{2,12} & r_{2,12}^2 \\ \vdots & \vdots & \vdots \\ r_{n,11}^2 & 2 \cdot r_{n,11} \cdot r_{n,12} & r_{n,12}^2 \end{pmatrix} \times \begin{pmatrix} \Sigma_{11} \\ \Sigma_{12} \\ \Sigma_{22} \end{pmatrix} \quad (5.46)$$

or

$$\mathbf{M} = \mathbf{T} \times \mathbf{S}. \quad (5.47)$$

From this, one obtains a solution for the elements of the Σ -matrix:

$$\mathbf{S} = (\mathbf{T}^T \mathbf{T})^{-1} \mathbf{T}^T \mathbf{M} \quad (5.48)$$

from which the emittance is obtained by (see equation (5.43))

$$\epsilon = \sqrt{S_1 S_3 - S_2^2} \quad (5.49)$$

Note that this procedure gives not only the emittance, but also the beam-correlations.

5.4.2 Inclusion of Experimental Errors

For experimental data, the σ_i are known within some uncertainty $\Delta\sigma_i$. In this case, one can use a weighted least-squares fit [85, 61] instead of the equal-weights fit given by equation (5.48), obtaining

$$\mathbf{S} = (\mathbf{T}^T \mathbf{C}^{-1} \mathbf{T})^{-1} \mathbf{T}^T \mathbf{C}^{-1} \mathbf{M}, \quad (5.50)$$

where \mathbf{C} is the covariance matrix of the experimentally measured quantities, defined by

$$\mathbf{C}_{ij} = \delta_{ij} \Delta\sigma_i \Delta\sigma_j, \quad (5.51)$$

with δ_{ij} being the Kronecker delta-function, and where I use Δ to indicate the uncertainties to avoid confusing multiple uses of the letter σ . The uncertainties in the elements of \mathbf{S} (i.e., in the Σ -matrix derived from the fit) are found by computing the covariance matrix of the fit parameters:

$$\mathbf{K} = \mathbf{U}^T \mathbf{C} \mathbf{U}, \quad (5.52)$$

where \mathbf{U} is defined as

$$\mathbf{U} = (\mathbf{T}^T \mathbf{C}^{-1} \mathbf{T})^{-1} \mathbf{T}^T \mathbf{C}^{-1}. \quad (5.53)$$

The uncertainties in the elements of \mathbf{S} are related to the diagonal elements of \mathbf{K} , by

$$\Delta S_i = \sqrt{K_{ii}} \quad (5.54)$$

The uncertainty in the emittance is then given by propagation of errors through equation (5.49), which, when expressed in terms of the Σ -matrix yields

$$\begin{aligned} \Delta\epsilon = & \left(\frac{\Sigma_{11}}{2\epsilon} \right)^2 K_{33} + \left(\frac{\Sigma_{22}}{2\epsilon} \right)^2 K_{11} + \left(\frac{\Sigma_{12}}{2\epsilon} \right)^2 K_{22} + \\ & 2 \frac{\Sigma_{11}\Sigma_{22}}{4\epsilon^2} K_{13} + 2 \frac{\Sigma_{11}\Sigma_{12}}{2\epsilon^2} K_{12} + 2 \frac{\Sigma_{12}\Sigma_{22}}{2\epsilon^2} K_{12}. \end{aligned} \quad (5.55)$$

Note that I have used the off-diagonal terms of the covariance matrix in an attempt to obtain better accuracy. As I will discuss below, this sort of error analysis gives dubious results and I have used a Monte-Carlo method [61] instead for my final results.

5.4.3 Thin Lens Treatment

It is instructive to write equation (5.48) out for the case of a thin lens quadrupole followed by a drift space of length L . In this case, the transport matrix is given by

$$\mathbf{r} = \begin{pmatrix} 1 & L \\ 0 & 1 \end{pmatrix} \begin{pmatrix} 1 & 0 \\ -\kappa & 1 \end{pmatrix}, \quad (5.56)$$

where $1/\kappa$ is the focal length of the quadrupole. The beam-size at the end of the drift space as a function of the quadrupole focal-length is (from one line of equation (5.46))

$$\sigma^2 = (1 - \kappa L)^2 \Sigma_{1,11} + 2L(1 - \kappa L) \Sigma_{1,12} + L^2 \Sigma_{1,22}. \quad (5.57)$$

As pointed out by Ross, *et. al.*, [86], this can be written in a more transparent form as

$$\sigma^2 = \sigma_o^2 L^2 (\kappa - \kappa_m)^2 + \frac{L^2 \epsilon^2}{\sigma_o^2}, \quad (5.58)$$

where σ_o is the beam-size at the entrance to the quadrupole and where

$$\kappa_m = \frac{\Sigma_{1,12}L + \Sigma_{1,11}}{\Sigma_{1,11}L} \quad (5.59)$$

is the value of κ that gives the minimum spot-size at the screen.

Since σ_o is presumably unknown, one must find both the second derivative and the minimum of σ^2 as a function of κ in order to find the emittance. If one rewrites equation (5.58) as

$$\sigma^2 = D^2 (\kappa - \kappa_m)^2 + \sigma_m^2, \quad (5.60)$$

where

$$D = \sqrt{\frac{1}{2} \left(\frac{\partial^2}{\partial \kappa^2} \sigma^2 \right)} \quad (5.61)$$

then the emittance is given by

$$\epsilon = \frac{\sigma_m D}{L^2}. \quad (5.62)$$

One can appreciate from this equation that in order to determine the emittance it is important to probe the minimum of the beam-size versus κ , in order to get σ_m , and that it is also important to vary κ over a sufficiently wide range to get a reliable value for D . For noiseless data, the emittance can be reliably extracted even without

probing the minimum. This shouldn't be surprising, since for ideal data one only needs three data points for any three different values of quadrupole strength in order to completely constrain the fit. For real (i.e., noisy) data, however, it is important to both probe the minimum beam-size and the "wings" where the beam-size becomes quite large.

5.4.4 Emittance Measurement Lattice and Procedure

The design of measurement systems to minimize the error in the emittance determination is discussed in the literature[86, 11, 87]. In order to minimize the effect of the finite resolution of the imaging system, one wants a large distance between the quadrupole being varied and a small beam-size at the quadrupole[86]. For a fixed emittance, this yields a larger value of σ_m relative to the fixed resolution of the imaging system. However, since the placement of the quadrupoles and phosphor screen was dictated by the requirements of the GTL as an operational—as opposed to experimental—system, these considerations are largely academic for the present work.

The emittance measurements for the RF gun made use of quadrupoles Q4 and Q5 and the chopper-screen. The alpha-magnet scraper was used to determine the momentum spectrum of the beam and to filter the momentum of the beam allowed to reach the screen. In this way, measurements could be made as a function of momentum spread, for comparison with the simulation results of Chapter 2.

The optics up to the alpha-magnet was designed so as to produce a reasonably small beam spot on the chopper-screen, even with Q4 and Q5 off. Q1, Q2, and Q3 were set at 98.9 m^{-2} , -90.4 m^{-2} , and 63.1 m^{-2} , respectively. These are considerably weaker quadrupole strengths than those for the running lattices listed in the earlier section of this chapter. The alpha-magnet strength was set so as to produce $\hat{q}_1 = 14.431 \text{ cm}$.

For the horizontal emittance measurements, Q4 was varied while keeping Q5 off. Following this, Q4 was degaussed and set to (nominally) $K_1 = 90 \text{ m}^{-2}$, and Q5 was varied. Ideally, the data from the variation of Q4 would have been used to obtain ϵ_x while that from the variation of Q5 would have been used to obtain ϵ_y . Unfortunately, saturation problems invalidated the Q5 data, as will be seen below.

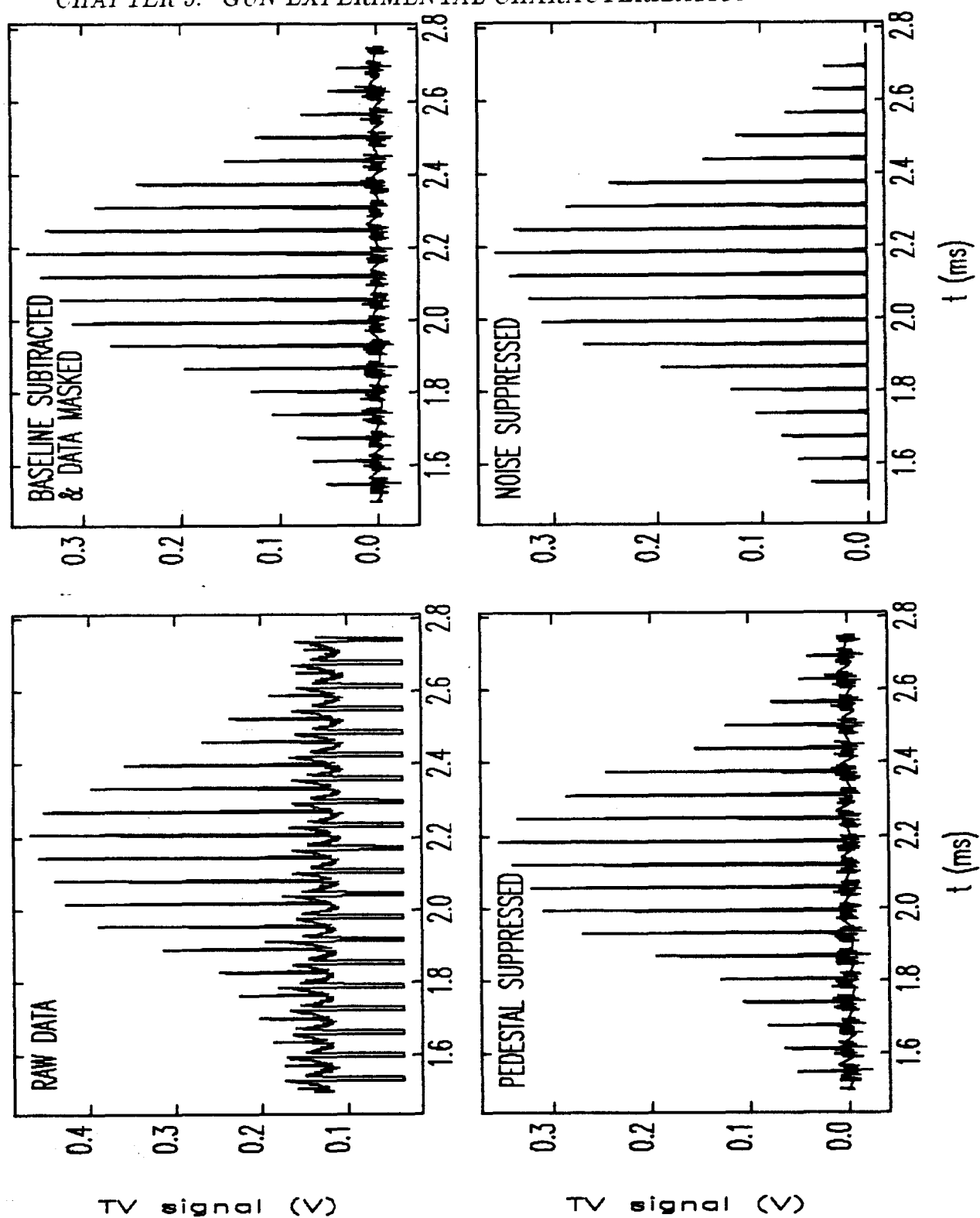


Figure 5.23: Signal Analysis for a Video Scan

For each quadrupole setting, the LeCroy 9450 oscilloscope was used to digitize a full screen sweep from the camera—i.e., a full two-dimensional intensity map of the beam—and the resultant waveform was transferred to the PC and stored there. Because of the large number of data points ($\sim 50K$) in each waveform, on-line processing of the data was neither possible nor would it have been efficient. Rather, data was collected and stored for later analysis on SSRL's VAX 8810. Figure 5.23 shows a section of a raw video scan taken in the course of one of the emittance measurements. The envelope of this signal is essentially the vertical beam profile, while the “sub-scans” (separated by regions where the signal falls to < 0.05 V) are horizontal slices through the beam at successive vertical positions. This data has a clear baseline variation that largely repeats through successive horizontal scans.

5.4.5 Analysis of Digitized Beam-Spot Images

To analyse the large amount of data that came from even a single emittance measurement, it was desirable to have a computer program that would process the raw video scans and reconstruct the two-dimensional beam-profile. I have employed several stages in the processing of such scans, as illustrated in Figure 5.23, and as implemented in the program `hvsan`:

1. Organization—The beginning and end of each horizontal sub-scan was located, and the data organized into a two-dimensional intensity map (or “pixel map”).
2. Baseline subtraction—The first horizontal sub-scan of every complete scan was used as the baseline for all subsequent horizontal sub-scans. (Even with no beam impinging on the screen, the signal from the camera was seen to vary over each horizontal sweep, rather than becoming the flat signal that one would expect in an ideal circumstance.) This involves assuming that this sub-scan is free of any beam-related signal, which is invariably true for the data I have taken. Since the height of the baselines for the sub-scans were seen to be vary slowly from sub-scan to sub-scan, the baseline scan was scaled by a smoothly-varying function of the scan number before subtraction.

In hindsight, a better procedure would probably have been to store a complete screen scan taken with no beam, and to subtract it in its entirety from all the other complete scans. This would have eliminated concerns about the variation of the baseline from sub-scan to sub-scan, assuming that the baseline scans were taken often enough to track variations in the camera performance with time.

3. Pedestal suppression—Baseline subtraction is sufficient to take out the variation of the baseline across each horizontal sub-scan, and to bring the resultant baseline within a few mV of zero (compared to several hundred mV for a typical beam-related signal). It was found, however, that sometimes there would be a clear pedestal, or voltage offset, remaining after the baseline subtraction. Hence, after baseline subtraction, *hvs* can be directed to find the pedestal of each sub-scan. It then smooths these pedestals as a function of scan number (in order to prevent noise from causing abrupt variations), before subtracting the pedestals. In most cases, pedestal adjustment is unnecessary (the effect of pedestal adjustment cannot even be seen in the Figure), amounting to a few mV compared to a signal of several hundred mV.
4. Masking—the data was masked by a window of user-specified dimensions, to eliminate known non-beam-related features appearing on the images (e.g., reflections from the screen holder). For most of the scans, 10% of the data from around the edges of each scan was masked out. More drastic masking was also necessary for some scans in order to eliminate obviously spurious signals, such might be caused by RFI. Contour graphs of the intensity distributions were used to verify that the signals being masked out were indeed spurious (i.e., obviously not part of the beam).
5. Noise suppression—A sequence of noise-suppression stages was employed:
 - (a) After subtraction of the baseline and pedestal, any pixel values below zero were assumed to be noise, and were set to zero.
 - (b) Any non-zero pixel surrounded with zero pixels above and below, or to the left and right, was assumed to be noise, and set to zero. This proved

invaluable in eliminating spurious peaks due to RFI, though it may have slightly truncated the edges of some beam images.

- (c) The peak pixel was found, which after the previous stages is almost guaranteed to be located in the image of the beam (i.e., to be unrelated to noise or baselines). The program then zeroed all pixels that were not connected to this pixel by a path going through other non-zero pixels.

6. Analysis—various analyses are available on the resultant pixel map:

- (a) Fractional-widths, RMS-widths, intensities, and centroids can be computed for any vertical or horizontal slice through the pixel map. The various width measures are described below.
- (b) The vertical and horizontal slices going through the peak of the pixel map can be written to disk.
- (c) The pixel map can be collapsed vertically into a single horizontal scan, which can be written to disk and analyzed for width, intensity, and centroid.
- (d) The pixel map can be collapsed horizontally into a single vertical scan, which can be written to disk and analyzed for width, intensity, and centroid.
- (e) Diagnostic output on the baseline and pedestal subtraction is available.
- (f) Data for making contour plots can be prepared.

An alternative to the somewhat intuition-based noise-suppression technique used here would be to use digital filtering. Unfortunately, digital filtering is inapplicable because the number of samples per sub-scan is too small, meaning that the noise frequencies are not sufficiently above the signal frequencies to allow suppression of noise without obvious corruption of the signal. The danger of the noise suppression technique used here is that it may eliminate valid information around the edges of the beam image. However, there is no indication that this is a problem in the data I have analysed; examination of the resultant beam profiles show no indication of significant truncation of the actual beam image.

5.4.6 Measures of the Beam Size

The use of “collapsed” vertical and horizontal scans proved particularly valuable in improving the smoothness of the variation of the beam width with quadrupole strength. The use of slices through the beam peak is somewhat problematical in that the location of the peak is in some cases poorly defined and also susceptible to noise. Two measures of beam-width are computed by *hvs*can: the $\pm 34.13\%$ half-width (hereafter the “ $\pm 34\%$ half-width”) about the median and the weighted RMS deviation from the median.

The $\pm 34\%$ beam-width, which I call ω , is identical to σ for a gaussian beam, but is well-behaved and easy to compute for a non-gaussian beam. It is also much less noise-sensitive than the weighted RMS deviation, and hence, initially at least, looked promising as a “robust” beam-size measure. ω for a scan $V(t)$, whether a collapsed scan or a slice, was determined by first normalizing the area under the scan, such that

$$\int_0^T V(t)dt = 1, \quad (5.63)$$

where $t=0$ is the start of the scan and $t=T$ the end. The median, T_m , was then found, defined by

$$\int_0^{T_m} V(t)dt = \frac{1}{2}. \quad (5.64)$$

The $\pm f$ fractional width, $\Delta T(f) = T_u - T_l$, is computed using

$$\int_{T_m}^{T_u} V(t)dt = f \quad (5.65)$$

and

$$\int_{T_l}^{T_m} V(t)dt = f. \quad (5.66)$$

where $f=0.3413$. The interval from $t = T_l$ to $t = T_m$ contains 34% of the intensity, as does the interval from $t = T_m$ to $t = T_u$. If $V(t)$ were a gaussian function of t , then $\omega = \Delta T/2$ would be equal to the sigma of the gaussian.

The RMS-deviation, represented by τ , is also equal to σ for a gaussian beam, but not is necessarily equal to the best-fit σ that one might obtain by fitting a gaussian to an arbitrary distribution. τ for any scan $V(t)$ is given by

$$\tau = \sqrt{\int_0^T V(t)(t - T_m)^2}, \quad (5.67)$$

where, as above, $V(t)$ is normalized to unit area.

The reader may wonder why I did not fit gaussians directly to the data. The reason is that the beam profiles are frequently so non-gaussian that this procedure would make little sense. Examples of beam profiles will be shown below.

Simulations of this method of measuring the emittance show that both ω and τ provide reasonable beam-size measures for use in place of σ in equation (5.48), even for very non-gaussian beams. Indeed, use of τ allows exact recovery of the RMS emittance even for non-gaussian beams. This should perhaps not be surprising, since the theory upon which the method is based deals explicitly with the transformation of the second moments of the particle distribution and since the RMS emittance depends only on the second moments of the particle distribution. The development of the Σ -matrix formalism in no way assumes that the beam being described has a gaussian phase-space distribution[68]. The use of ω , on the other hand, leads to errors for non-gaussian beams, as might have been anticipated. ω is, however, attractive for experimental work in that it is less susceptible to errors introduced by noisy “wings”. Simulations with the lattice used for the experimental measurements shows that use of ω tends to over-estimate the emittance. Since *elegant* calculates τ and ω , it is possible to make direct comparisons of actual measurements and simulated measurements using the two beam-size measures, and I shall report on such comparisons below.

5.4.7 Imaging and Phosphor Resolution

The resolution of the imaging system[88] used to acquire the screen images will effect how accurately the emittance can be measured, primarily by affecting the ability to determine the minimum beam-size. (See the discussion above related to equation (5.62).) The resolution depends on a number of factors: the resolution of the screen material (i.e., how large a emitting area would be activated by a zero-emittance electron beam), the resolution of the camera tube (i.e., how many pixels), the magnification, and the contributions of diffraction in the camera lens.

As a step toward determining the resolution, I used a back-lit slit of variable gap (actually the gap of a set of precision calipers), and measured the FWHM of the

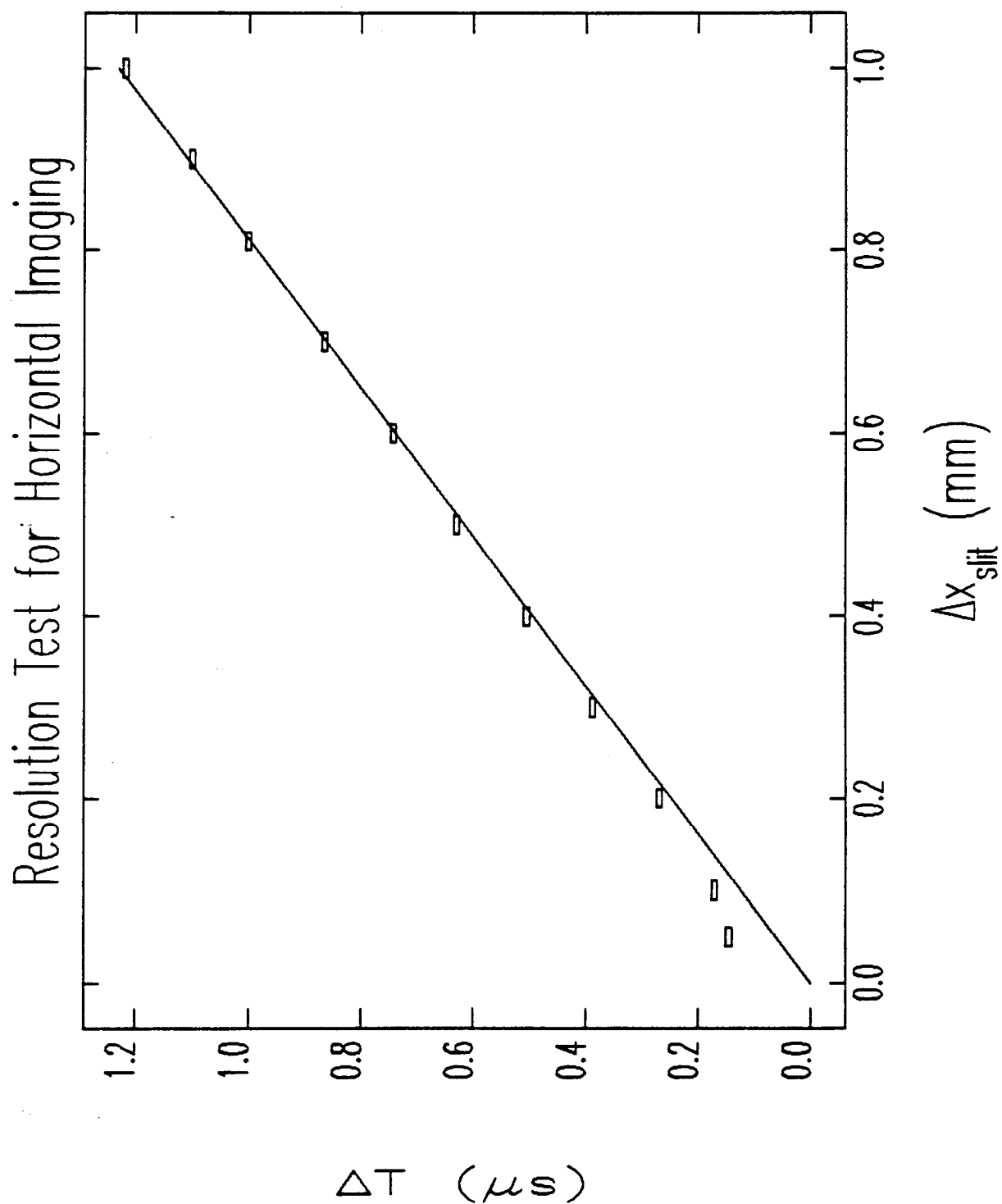


Figure 5.24: Resolution Test for Horizontal Imaging

digitized video signal as a function of the slit spacing. The results for the horizontal scan are shown in Figure 5.24, from which one sees that the resolution (the FWHM ΔT measurement for a hypothetical zero-width slit) is by extrapolation about $0.15 \mu\text{s}$. This corresponds to a half-width resolution of $0.075 \mu\text{s}$.

The corresponding experiment for the vertical scan is dubious, since the TV signal is broken into a sequence of horizontal scans, with each frame containing 240 such scans. The spacing between these scans is $64 \mu\text{s}$, so that the resolution is clearly worse than this; the smallest vertical full width that can be measured is $64 \mu\text{s}$, which I will take to be the vertical resolution. The corresponding half-width resolution is $32 \mu\text{s}$.

For the beam measurements, as just discussed, I have used the parameters ω and τ to characterize the measured beam size. It is necessary that the resolution measurements be cast in an equivalent form, for comparison with ω and τ measurements for the beam.

The imaging resolutions above were given as half-width at half-max (HWHM) values. At the resolution limit, the video trace has a triangular shape, corresponding to the "lighting" of one pixel with the adjacent pixels being off:

$$V_{\Delta}(t) = \begin{cases} 0 & |t| > T \\ \frac{T-|t|}{T^2} & |t| \leq T \end{cases}, \quad (5.68)$$

where the area is normalized to 1. The HWHM is, of course, simply $T/2$, while ω_{Δ} is defined by

$$0.3413 = \int_0^{\omega_{\Delta}} V_{\Delta}(t) dt, \quad (5.69)$$

from which $\omega_{\Delta} \approx 0.87 \cdot \text{HWHM}$. The RMS t value for $V_{\Delta}(t)$ is simply

$$\tau_{\Delta}^2 = \int_{-T}^T V(t) t^2 dt, \quad (5.70)$$

from which I obtain $\tau_{\Delta} \approx 0.82 \cdot \text{HWHM}$. These are close enough to allow simplification of the analysis by taking $\omega_{\Delta} = \tau_{\Delta} \approx 0.85 \cdot \text{HWHM}$.

Using the resolutions given above,

$$\omega_{x,\text{imaging}} = \tau_{x,\text{imaging}} = 0.85 \cdot 0.075 \mu\text{s} \approx .064 \mu\text{s} \quad (5.71)$$

and

$$\omega_{y,\text{imaging}} = \tau_{y,\text{imaging}} = 0.85 \cdot 0.032 \text{ms} \approx .027 \text{ms}. \quad (5.72)$$

For the magnification used in the experiments, these time resolutions in terms of correspond to spatial imaging resolutions of 58 μm horizontally and 55 μm vertically. The fact that these nearly agree is purely coincidental, but I shall take advantage of the coincidence and use 57 μm as the value for both planes.

In the simplest analysis, these resolutions add in quadrature to the actual beam width and the phosphor screen contributions, to produce

$$\omega_{\text{meas}}^2 = \omega_{\text{beam}}^2 + \omega_{\text{imaging}}^2 + \omega_{\text{phosphor}}^2 \quad (5.73)$$

$$= \omega_{\text{beam}}^2 + \omega_{\text{resol}}^2, \quad (5.74)$$

and similarly for τ in this and all subsequent equations. Rewriting this, one sees that

$$\omega_{\text{beam}} = \sqrt{\omega_{\text{meas}}^2 - \omega_{\text{resol}}^2}. \quad (5.75)$$

Thus, the actual beam width can be deduced from the measurements, with the uncertainty being

$$(\Delta\omega_{\text{beam}})^2 = \frac{(\omega_{\text{meas}}\Delta\omega_{\text{meas}})^2 + (\omega_{\text{resol}}\Delta\omega_{\text{resol}})^2}{\omega_{\text{meas}}^2 - \omega_{\text{resol}}^2}, \quad (5.76)$$

from which one sees that this procedure is highly uncertain unless $\omega_{\text{meas}}^2 \gg \omega_{\text{resol}}^2$, i.e., unless the use of equation (5.75) is a small correction. If this is the case, one sees that $\Delta\omega_{\text{beam}} \approx \Delta\omega_{\text{meas}}$. Estimation of $\Delta\omega_{\text{meas}}$ is discussed below.

The screen material used for the measurements I will analyse here (see below), is rather grainy and is reported to have a resolution of 50–100 μm [89]. (My own examination of the material with a microscope reveals pitting on the scale of 100–200 μm . If this is taken to define the “pixel” size, then the half-width resolution would be 50–100 μm , which is consistent with the published figure.) Adding this in quadrature with the imaging resolution gives $\omega_{\text{resol}}^2 = 75\text{--}115\mu\text{m}$. In order to simplify the analysis, it is convenient to use the average (95 μm) of these two limits in what follows.

The minimum measured horizontal beam sizes are about 400 μm , whereas the minimum measured vertical beam sizes are about 220 μm . The use of equation (5.75) is thus acceptable for the horizontal and vertical planes.

5.4.8 Choice of Screen Material and Experimental Limitations

An additional source of uncertainty in the emittance measurements stems from the saturation and linearity of response of the screen material. Two different screen materials were installed for the chopper-screen. The first was $\text{Gd}_2\text{O}_2\text{S} : \text{Tb}$, which is the material chosen by SLAC for the SLC[90]. This material proved insufficiently robust for the beam intensities used in daily operation of the gun. As a result, the screen was damaged, making emittance measurements with it difficult (one had to try to steer the beam to an undamaged part of the screen, and keep it there while varying Q4 and Q5).

More recently, a more robust screen was installed, made of "SLAC chromate" ($\text{Al}_2\text{O}_3(\text{Cr})$, material 4 in [90]). This material is grainy compared to $\text{Gd}_2\text{O}_2\text{S} : \text{Tb}$, but has good light output and (judging from the limited data presented in [90] and the statements made in [89]) linear response (i.e., the amount of light is proportional to the number of electrons). No experiments were done to specifically check the linearity (an oversight).

In an attempt to ensure that neither the phosphor nor the camera was saturating, I focused the electron beam to a very small spot and noted the signal level from the camera. I then decreased the beam intensity, noting when I had reached a beam intensity where the intensity of the video signal was indeed changing as the beam intensity decreased. I then maintained the beam intensity at a sufficiently low level to stay below about half of this signal level. As will be seen below, this precaution proved insufficient, and there is clear evidence of saturation in some of the measurements.

Another limitation on the emittance measurements was due to the thick substrate of the chromate screen, which resulted in unacceptable heating of the screen and out-gassing at beam currents (into the screen) greater than 100 mA. In a test, the vacuum increase for 300 mA was sufficient to cause an alarming increase in the GTL vacuum pressure, and an unacceptable increase in the gun vacuum pressure. As a result, no measurements could be made of the effect of beam current on emittance. The experiments reported on below were done for about 270 mA out of the gun, with the current out of the alpha-magnet further limited by the scraper. In retrospect,

data could have been taken for a larger range of gun currents for a sufficiently small momentum spread. At the time, I was more interested in the emittance for large fractions of the beam, such as were intended to be used in actual operation.

5.4.9 Overview of the Experiments

Having used `hvs` to process the scans for any set of measurements, the resultant beam-widths as a function of quadrupole strength were then available for calculation of the emittance. I wrote the program `emitmeas` to do this analysis, with `elegant` being used to calculate the matrices as a function of quadrupole strength. In addition, `emitmeas` and `elegant` can be used to do simulated emittance measurements, with various types of initial beam phase-space distributions (e.g., gaussian, uniform, or `rfgun`- or MASK-generated).

The experiments I shall report on here are by far the most complete set of results I have to date and give simultaneous horizontal and vertical emittance data as a function of momentum spread allowed through the alpha-magnet. Constant beam and RF conditions were maintained for the entire series, with $E_{p2} \approx 75 \text{ MV/m}$ (estimated from the momentum peak of the beam) and $J \approx 5 \text{ A/cm}^2$ (estimated from E_{p2} , the current at GT1, and simulations of beam-losses in the transport line). The beam current into the alpha-magnet was 230 mA. The momentum peak was $5.026 \pm 0.048 m_e c$ (this value is the average over the all spectrum measurements taken, one for each set of emittance scans).

As in previous chapters, I shall characterize the momentum spread in terms of the parameter f , defined as

$$p_{\min} = p_{\max} \frac{1 - f}{1 + f}, \quad (5.77)$$

where p_{\min} is the minimum momentum allowed to pass through the alpha-magnet by the scraper, and p_{\max} is the maximum momentum in the beam. f is essentially the fractional half-momentum spread of the beam for which the emittance is measured. A total of eight emittance measurements were performed, four involving variation of Q4 and four involving variation of Q5. f was varied from about 0.08 to 0.03.

Unfortunately, the data involving variation of Q5 were seriously affected by camera saturation, as Figure 5.25 shows. The intensities plotted here are the signals

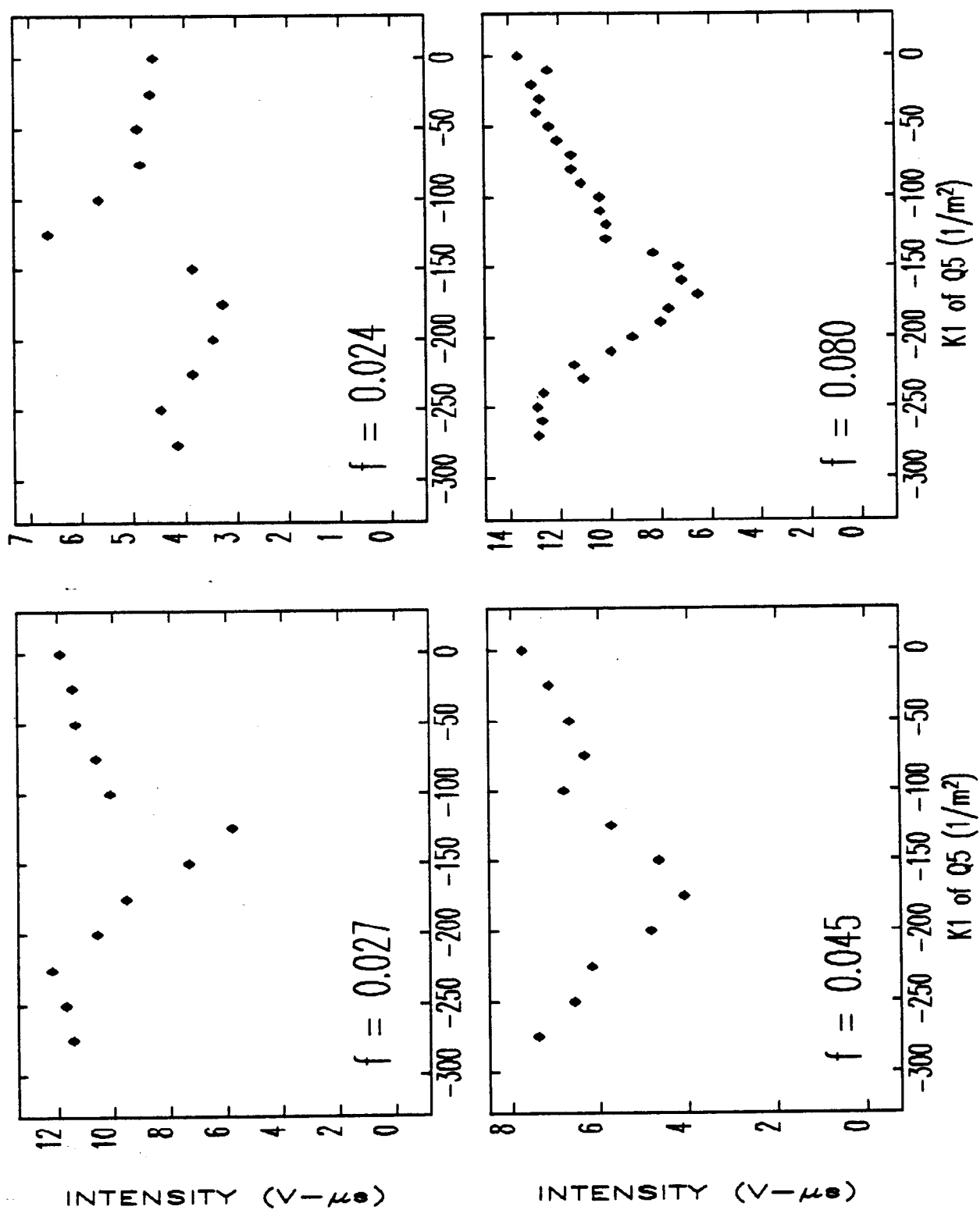


Figure 5.25: Integrated Video-Signal Intensity for Several Q5 Settings, for Various Values of f .

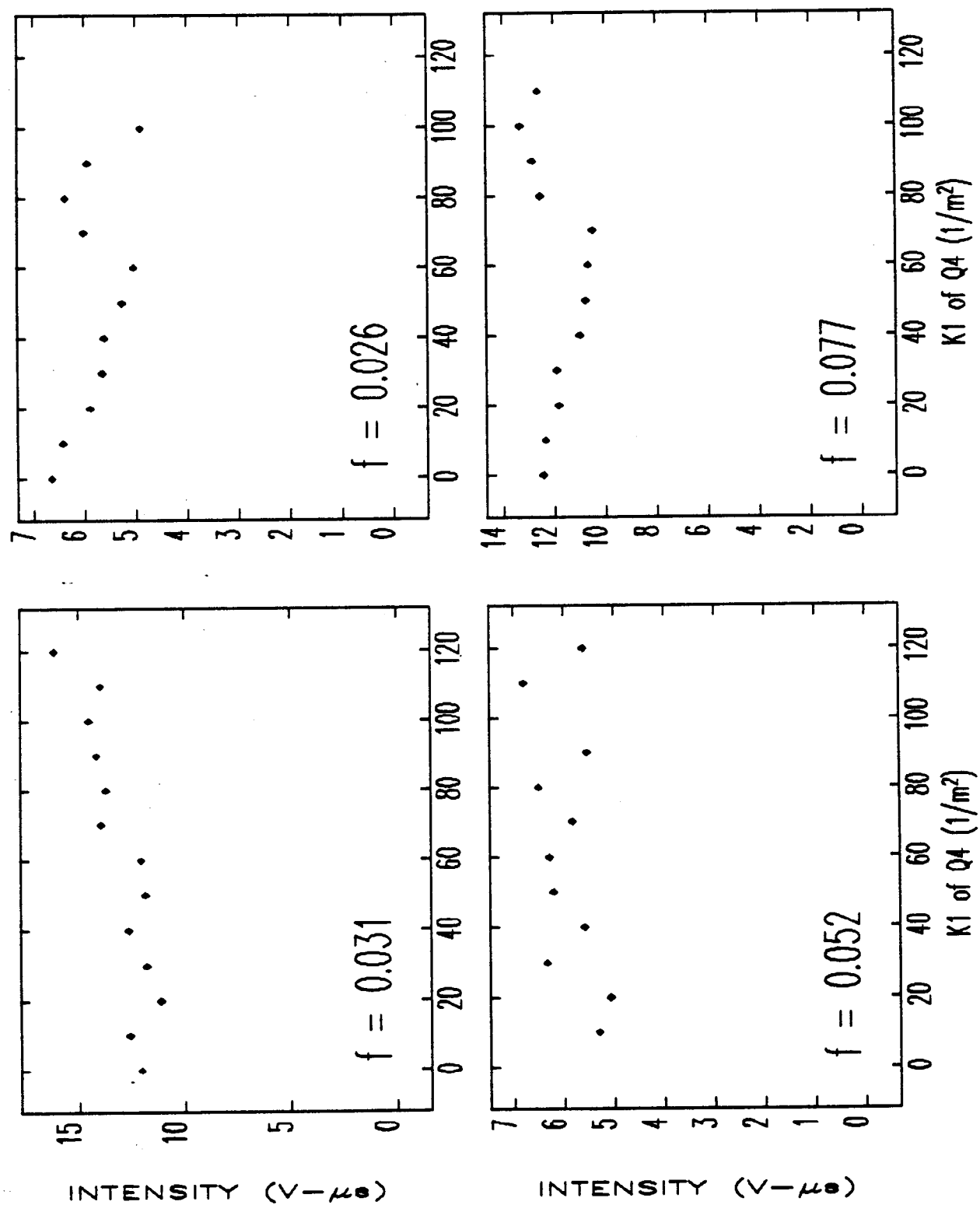


Figure 5.26: Integrated Video-Signal Intensity for Several Q4 Settings, for Various Values of f .

integrated over the pixel maps, and should be constant for a system with no saturation, since the beam current exiting the alpha-magnet was held constant. (Note that the intensity does not decrease monotonically with f , since the camera aperture was opened as f was decreased in order to get a better signal-to-noise ratio.) The dips in intensity in Figure 5.25 coincide with the minimum spot-sizes in the vertical plane, and clearly imply the presence of some saturation effect. While I will not take space to show the data, graphs of the horizontal and vertical beam-sizes versus the strength of Q5 give no indication that saturation is taking place, presumably because the saturation is a smooth phenomenon. Because of the dramatic saturation problem apparent for this data, I will not make further use of it.

Figure 5.26 shows intensity data for the measurements involving variation of Q4. The minimum horizontal beam-sizes occur around 70m^{-2} , while the minimum vertical beam-sizes occur around 20m^{-2} . In some cases, there is apparently systematic variation of the intensity, though the effect is mild compared to the previous Figure. Since the detailed nature of the saturation is not understood, I will simply use the data for Q4 "as is".

Since there is a great deal of data involved in these measurements, I will confine myself to presenting only a sample. In particular, Figure 5.27 shows a series of x - y contour graphs of beam-intensity. Similarly, Figures 5.28 and 5.29 show collapsed x and y beam intensity distributions corresponding to the contour graphs. One sees from these Figures that the intensity distributions are not well described by a gaussian, which is why I did not fit gaussians to the data in order to deduce the beam-size, as discussed above. One can also see how the increasing strength of the horizontally-focusing quadrupole first focuses then over-focuses the beam horizontally, and how the beam is defocused vertically. Note also that the beam is not symmetric in x ; this asymmetry is genuine, and was clearly visible in the TV images during the experiments. It is a result of second-order x - y coupling by the alpha-magnet, and is qualitatively reproduced in simulations.

The axes in these graphs were converted to distances from time intervals using $\Delta x(\text{mm}) = (0.91 \pm 0.02)\Delta T_x(\mu\text{s})$ and $\Delta y(\text{mm}) = (2.05 \pm 0.03)\Delta T_y(\text{ms})$. The calibrations were obtained from noting the positions on the TV scans of known features on the screen. Note that the errors in the calibrations of spatial size in terms of

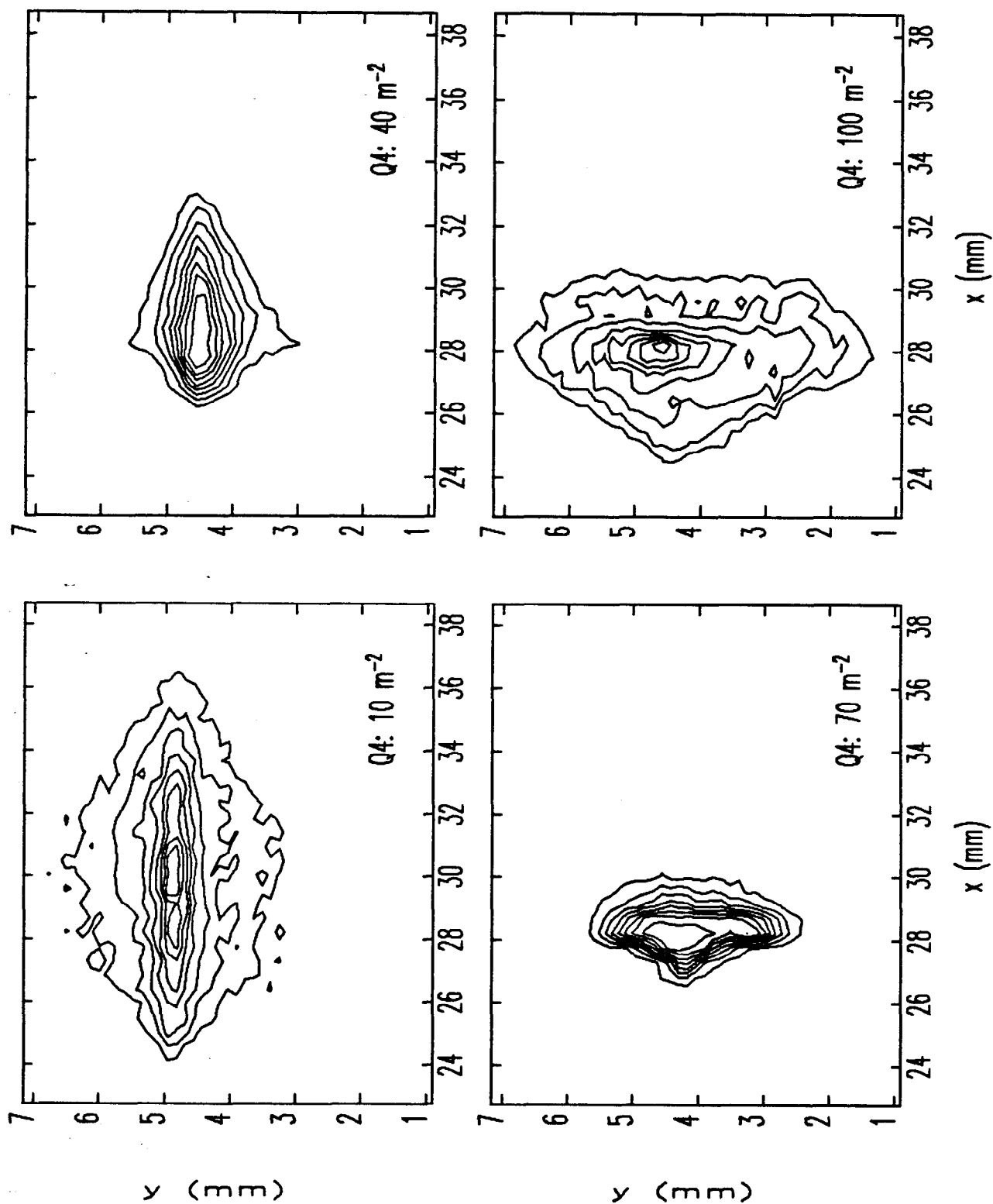


Figure 5.27: 10%-Contour Graphs of for Several Q4 Settings, from Experiments with $f=0.08$.

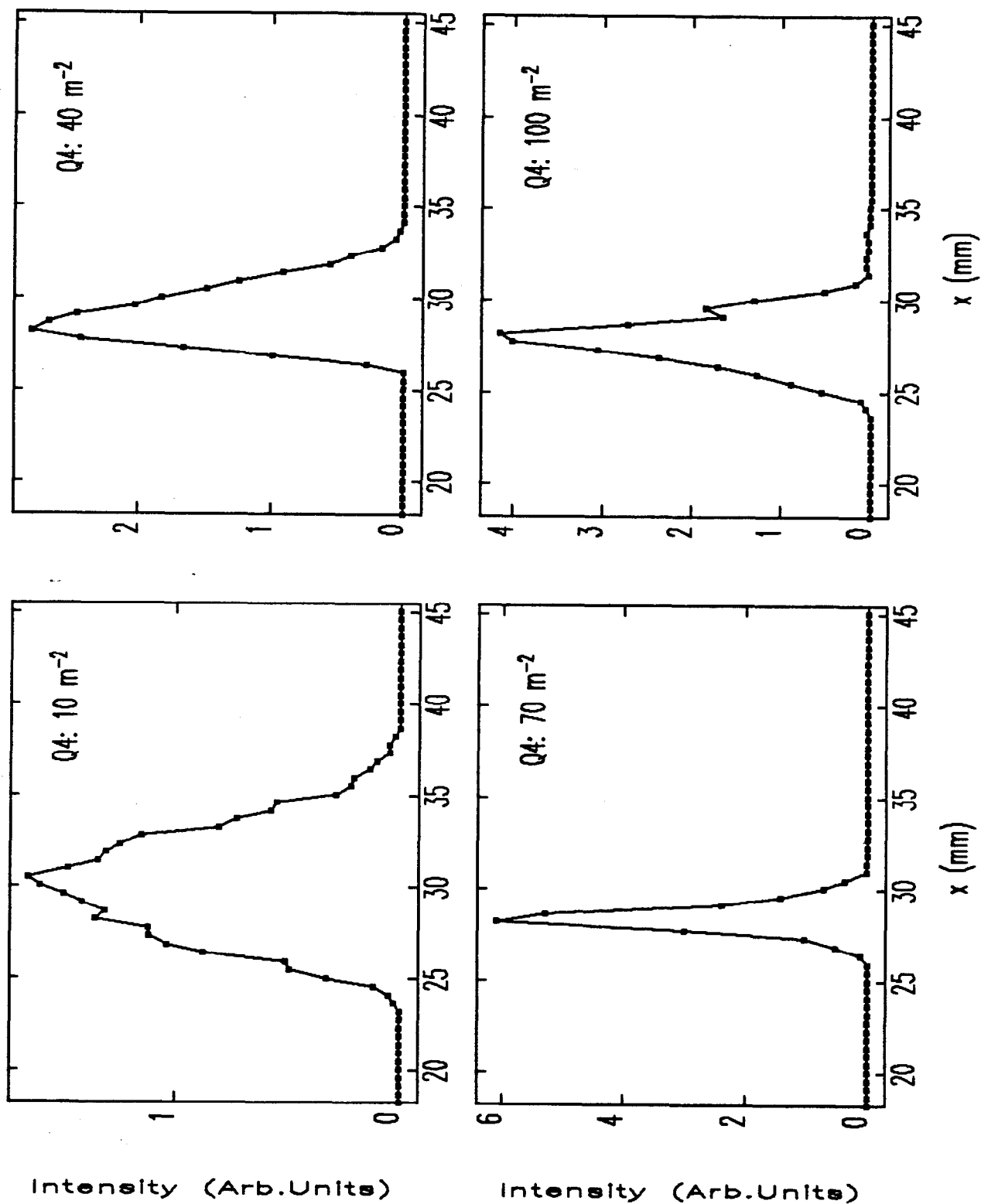


Figure 5.28: Collapsed Horizontal Beam-Intensity Profiles for Several Q4 Settings, from Experiments with $f=0.08$.

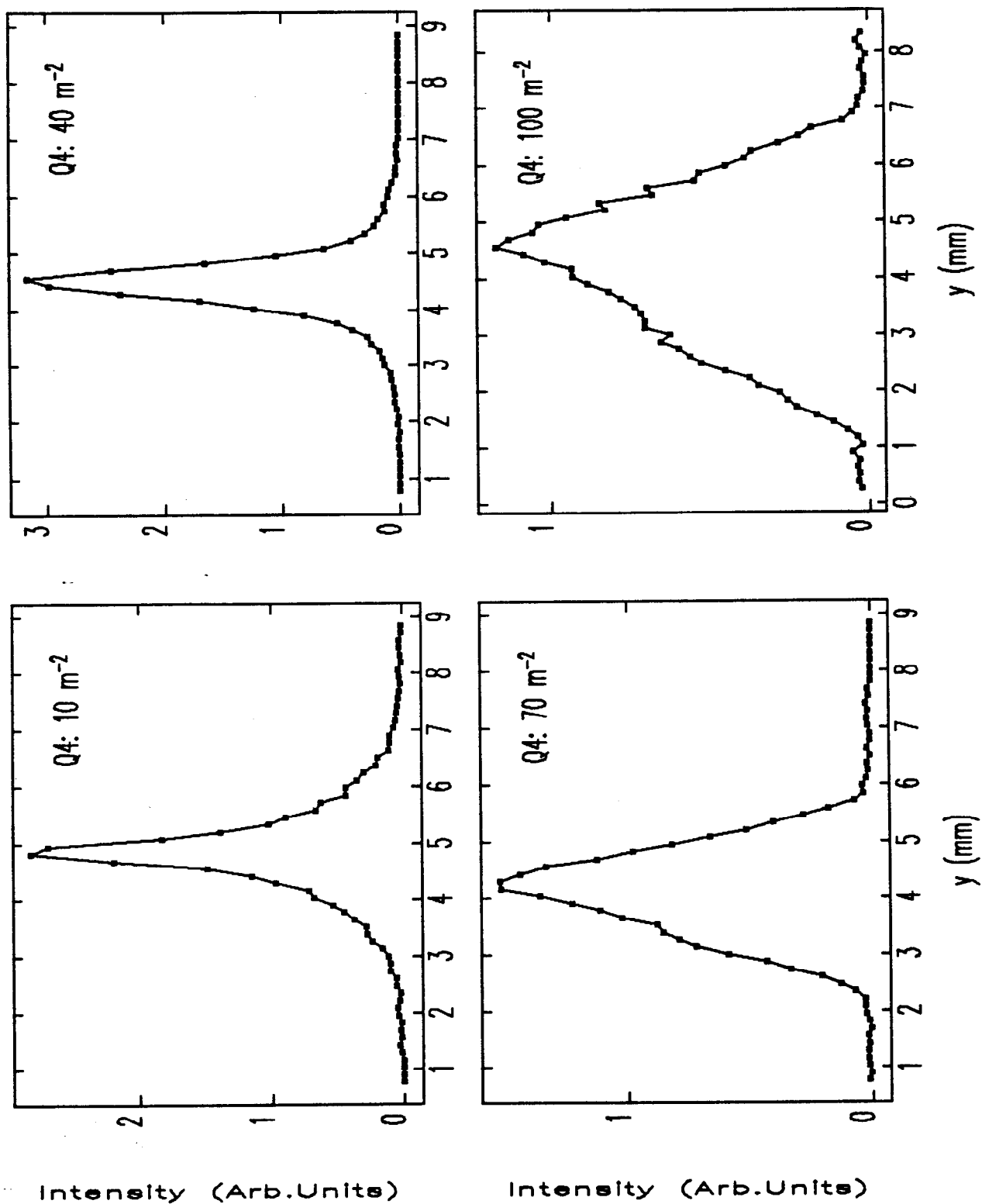


Figure 5.29: Collapsed Vertical Beam-Intensity Profiles for Several Q4 Settings, from Experiments with $f=0.08$.

time-interval imply errors in the measured beam-sizes and hence errors in the emittance derived from these. However, one cannot equate the fractional error in the calibrations with the (supposedly) normally-distributed fractional uncertainty of the measured beam-sizes, since the calibration error is systematic and implies no fluctuation of the measured beam-sizes about the fit.

The effect of calibration errors on the emittance can be estimated using the thin-lens solution given in equation (5.62). $\Delta\sigma_m/\sigma_m$ is equal to the fractional uncertainty in the calibration. Similarly, $\Delta D/D$ is equal to the fractional uncertainty in the calibration, since $D^2 \sim \sigma^2$. Hence, the fractional uncertainty in the emittance is $\sqrt{2}$ times the fractional uncertainty in the calibration. This amounts to about 3% for the horizontal plane and 2% for the vertical, which is insignificant compared to the effects of statistical errors in the beam-size measurements.

5.4.10 Estimation of Uncertainties

Knowledge of the normally-distributed errors in the measured beam-sizes can come only from statistical information gleaned from actual beam-size measurements. In addition, it is reasonable to assume that the resolution with which the beam-size can be measured is a lower limit on the uncertainty in any beam-size measurement.

In order to assess the uncertainty in the beam-sizes, I first fit the data using an assumed uncertainty equal to the resolution (i.e., 95 μm), in order to provide a covariance matrix for the weighted fit. This is important in obtaining good fits to the data near the minima, since the unweighted fit tends to fit the larger beam-sizes disproportionately well. To see why, note that

$$\Delta(\sigma_i^2) = 2\sigma_i\Delta\sigma_i. \quad (5.78)$$

The equal-weights fit to σ^2 assumes that $\Delta(\sigma_i^2)$ is the same for all points, which is equivalent to assuming larger uncertainties for the smaller σ_i . Hence, an equal weights fit should be expected to fit the smaller beam-sizes poorly, as is observed.

Having done the initial fit, I calculated the rms-deviation from the fit, defined by

$$r = \sqrt{\frac{1}{N-3} \sum_{i=1}^N (\sigma_i - \sigma'_i)^2}, \quad (5.79)$$

where σ'_i represents the value returned by the fit, and where $N - 3$ is used because there are 3 parameters in the fit, reducing the number of degrees of freedom. I then used the greater of r and the resolution as the actual uncertainty in the σ_i , and refit the data.

The errors in the Σ -matrix and the emittance can be calculated using equations (5.54) and (5.56). As mentioned above, problems arose in doing this. In particular, the uncertainties in the y-plane emittance were very large, even though the fits were good, in the sense of having small deviations of the data points from the fit. The problem is related to the fact that the y-plane Σ -matrix is such that $\Sigma_{33}\Sigma_{44} \approx \Sigma_{34}^2$, so that small errors in the Σ -matrix can translate into large errors in the emittance. (This is not true for the x-plane, where Σ_{12}^2 is small compared to $\Sigma_{11}\Sigma_{22}$.) However, I am convinced that the error-propagation is inadequate and greatly over-estimates the actual effect. In equation (5.56), I included the effect of off-diagonal terms in the covariance matrix for the Σ -matrix, even though most analyses do not use these terms[85]. I found that the off-diagonal terms made large differences in the computed uncertainties, which is highly unusual.

To diagnose this further, I made use of a feature of `emitmeas` which allows the addition of normally-distributed random deviates to the beam-size data prior to fitting. In particular, I used `emitmeas` to add ensembles of normally-distributed random deviates to data that was known to be perfectly fit by equation (5.46) and to compute the Σ -matrix and emittance for each "tweaked" data set. (I used 500 error ensembles with $4\text{-}\sigma$ gaussian distributions.) Statistics were kept to permit computation of the average Σ -matrix, the rms deviation of the Σ -matrix elements from their averages, the average emittance, and the rms deviation of the emittance from the average. If the first-order error-propagation is adequate, then the average Σ -matrix together with the rms deviation of the elements of the Σ -matrix should, when used in equations (5.49) and (5.56), reproduce the emittance and its rms deviation as computed directly from the results for each ensemble.

For the x-plane data, the two methods agreed very well on the emittance itself, and within 20% on the uncertainty. For the y-plane data, however, the uncertainty in the emittance as computed via error propagation was wildly different from that computed directly from the emittance for the ensembles. Differences of several orders

of magnitude were frequently obtained, even though the emittances themselves agreed to 10%.

Additional skepticism about the error-propagation when applied to the y-plane data comes from observing the effects of eliminating points from the fits. If the calculated emittance is in fact highly uncertain, then elimination of poorly-fit points should reduce the uncertainty and also change the emittance. Neither of these effects was observed. In one case, half of the data was eliminated with little change either in the calculated emittance or the uncertainty computed via error propagation.

I believe that the reason for this failure in the error propagation is the fact that the elements of the Σ -matrix are not independent, being physically constrained by the emittance to have a certain relationship. Hence, in the Monte-Carlo error analysis (to be described presently), the addition of errors causes all of the Σ -matrix elements to change in a constrained way, keeping the emittance approximately unchanged. In the error-propagation analysis, however, the elements of the Σ -matrix are assumed to be independent, which causes over-estimation of the effect of an error in one element of the Σ -matrix by ignoring necessary correlated errors in the other elements. While I have not attempted higher-order error-analysis or pursued this problem beyond what is stated here, it is clear that the Monte-Carlo method is the more reliable method, since it is, in effect, accurate to all orders.

Based on these conclusions, the analysis proceeded by first doing the initial fit and computing the rms deviation, r , as described above. To apply the Monte-Carlo method for the error analysis, I then computed the emittance and its uncertainty from statistics for 100 sets of $4\text{-}\sigma$ normally-distributed errors added to the ω or τ data values, with the sigma of the normal distribution being given by the larger of r and the resolution. This procedure is performed automatically by `emitmeas`.

5.4.11 Experimental Results

Figures 5.30 and 5.31 show the horizontal and vertical beam-sizes as a function of the strength of Q4, for $f = 0.08$. Also shown are the fits to the data, as computed by `emitmeas` (with no errors added to the data). The data for the horizontal plane is quite well matched by the fits, with the results for the collapsed scans being the

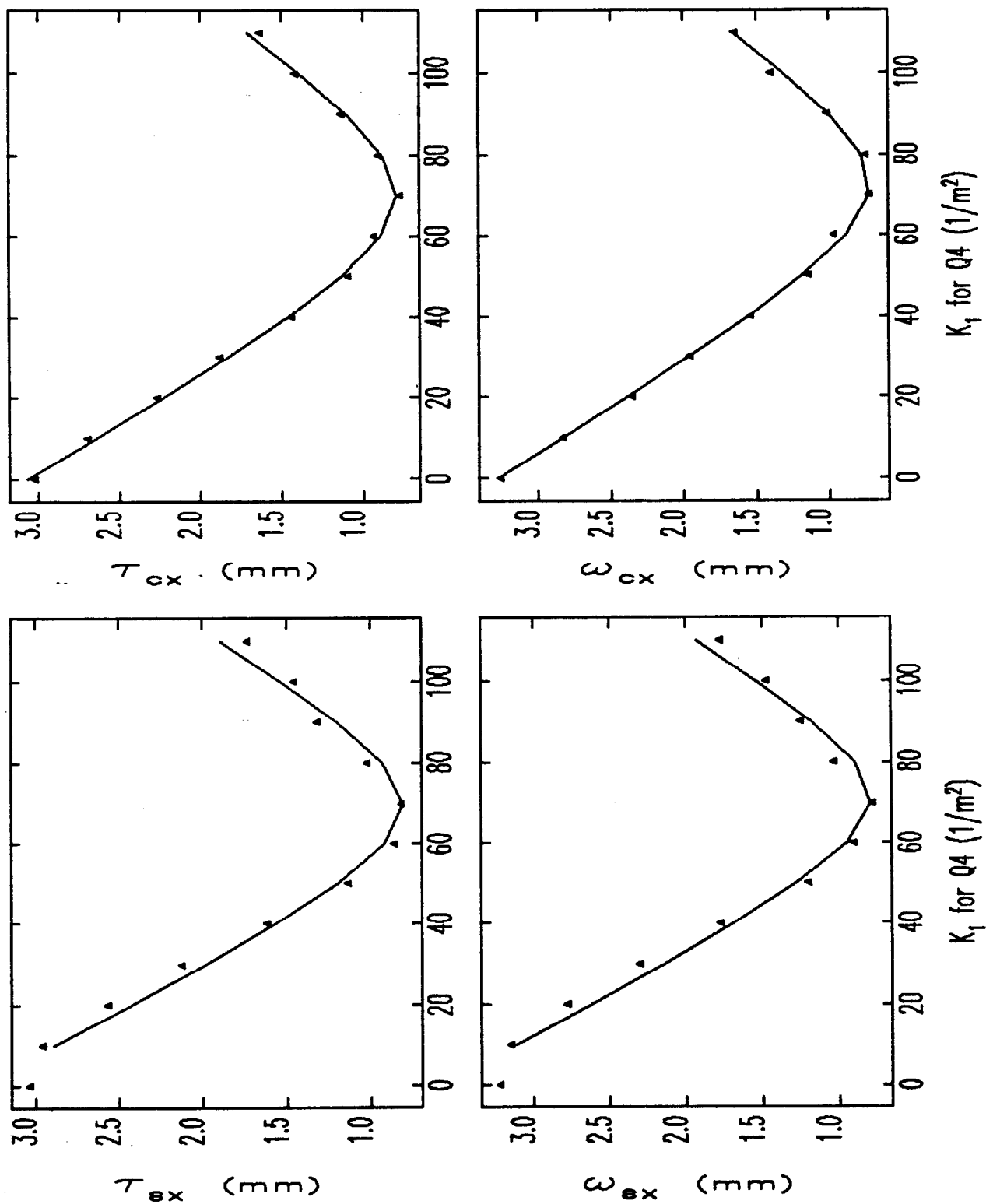


Figure 5.30: Horizontal Beam-Size versus Q4 Strength, for $f = 0.08$. (Points are experimental data, lines are fits.)

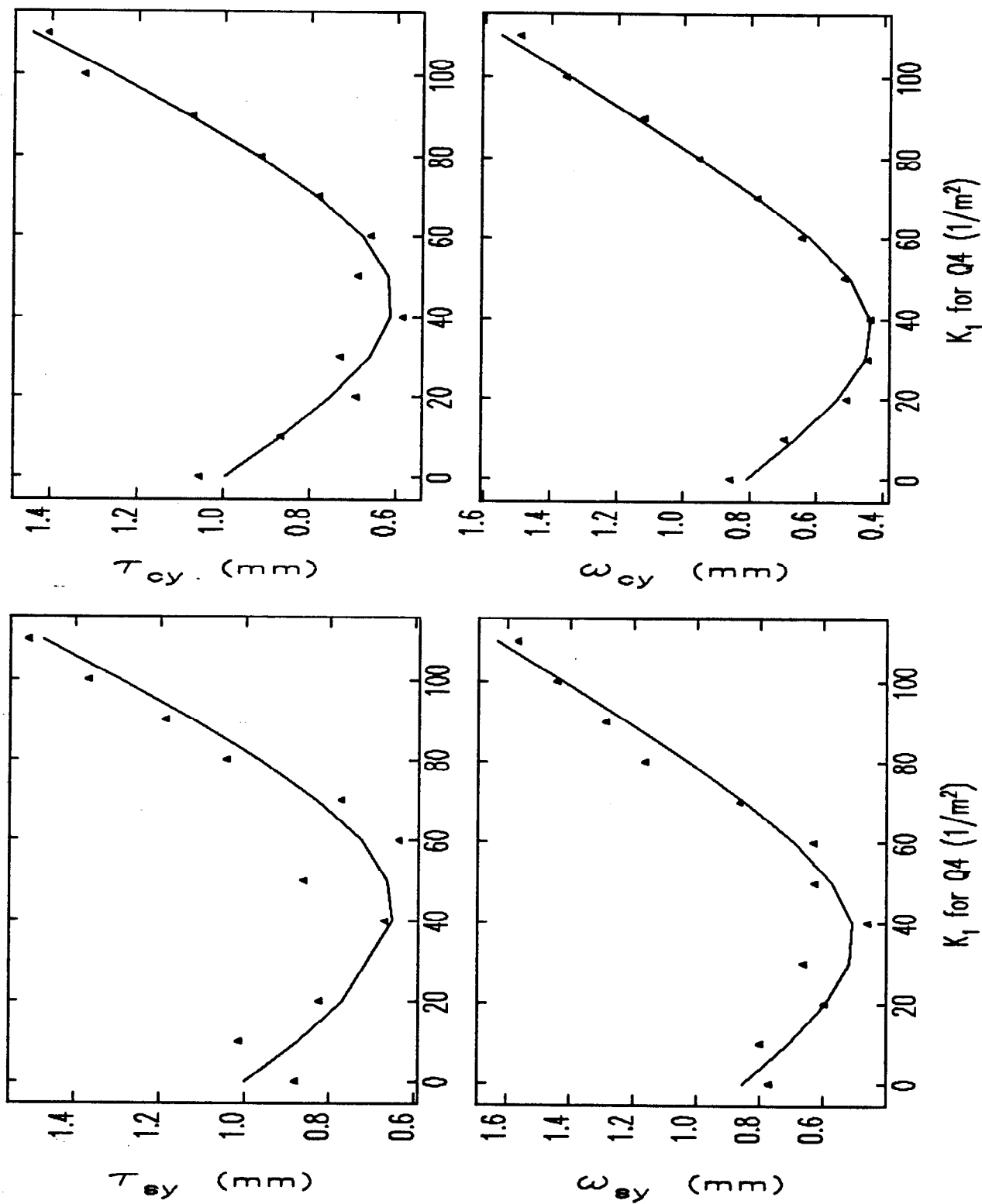


Figure 5.31: Vertical Beam-Size versus Q4 Strength, for $f = 0.08$. (Points are experimental data, lines are fits.)

smoothest. The different beam-size measures, ω and τ , appear to agree reasonably well for the horizontal plane. Similar observations hold for the vertical plane, although the data appears to be noisier because the range of variation of the beam-size is smaller. The vertical τ data is considerably noisier than the vertical ω data, a pattern which holds in general (though not for the data in Figure 5.30).

The reader may wonder why the vertical beam size should decrease as the strength of the horizontally focusing quadrupole is increased. The reason is that the beam is vertically converging when it exits the alpha-magnet. With Q4 turned off, there is a beam-waist in the vertical plane before the beam reaches the screen. As the strength of Q4 is increased, the vertical defocusing causes the vertical waist to move toward the screen, resulting in smaller beam-sizes at the screen.

Figures 5.32 and 5.33 show the measured emittance as a function of the momentum spread, f . For each of the x and y planes, there is a set of four graphs. Each Figure shows the emittance as deduced from ω and τ beam-sizes for the central slice through the beam and for the collapsed scan. One sees that there is good general agreement between the emittances as deduced from the four different measures, with a clear trend toward smaller emittances at smaller momentum spreads. (In some cases, only three data points appear, because the beam-size data was too noisy to fit.)

5.4.12 Comparison of Experiments and Simulations

The mathematical basis for the emittance measurements, given in equations (5.42) through (5.50), assumes a mono-energetic beam. Until now, I have not dealt with the question of the validity of the method in the presence of significant momentum spread in the beam. At issue here is the effect of chromatic aberrations in the quadrupole that is varied.

The MASK data I shall use for all simulations in the remainder of this section is for $E_{p2} = 75\text{MV/m}$ and $J = 10\text{A/cm}^2$, which is close to the experimental conditions of $E_{p2} \approx 75\text{MV/m}$ (determined from the position of the momentum peak) and $J \approx 5\text{A/cm}^2$. Since the emittance is a weak function of J at low current densities (see Chapter 2), the difference between 5 and 10 A/cm^2 is negligible.

As a preliminary illustration of the importance of chromatic aberrations in the

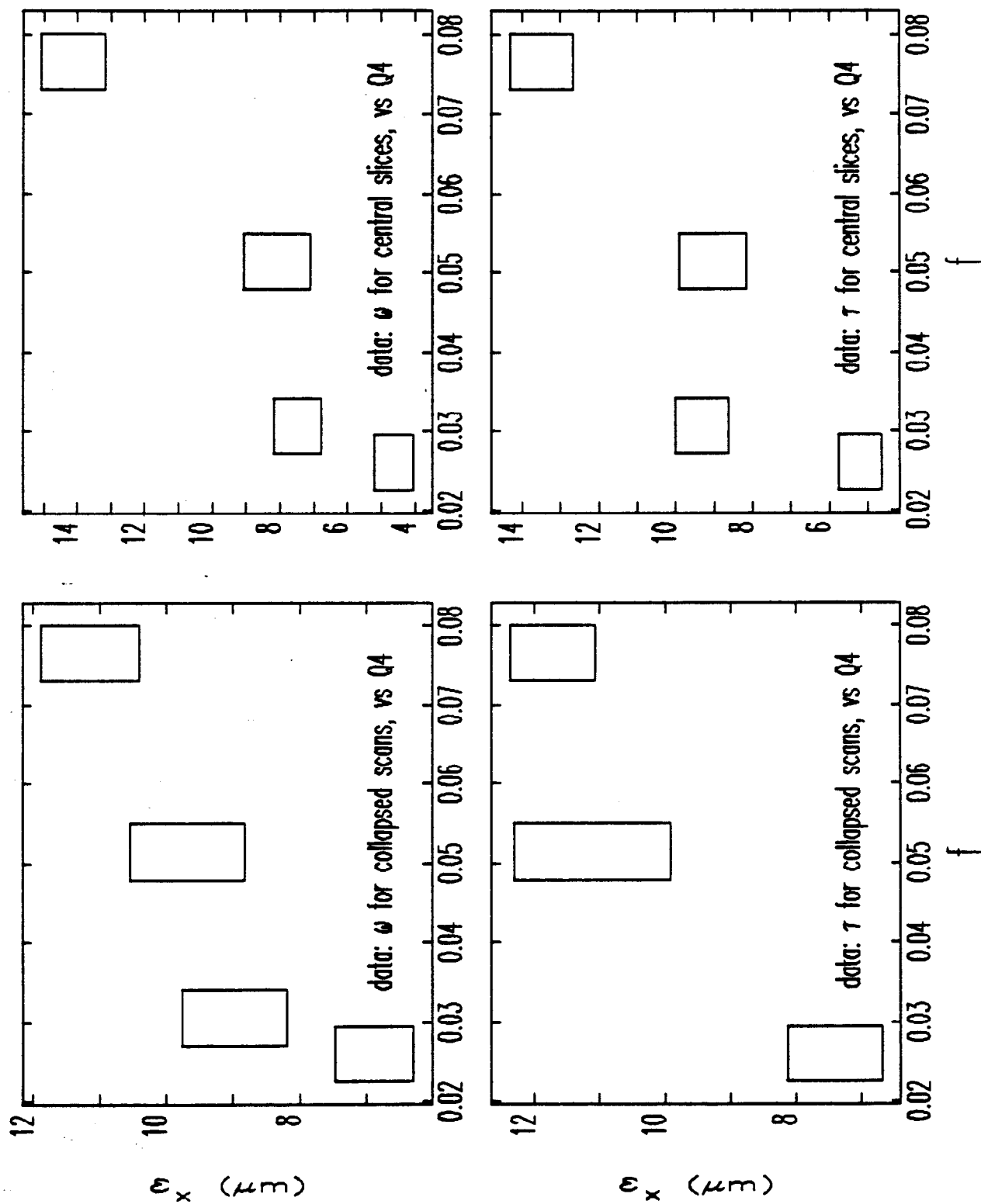


Figure 5.32: Horizontal Emittance versus f (Momentum Spread) as Inferred from Variation of Q4.

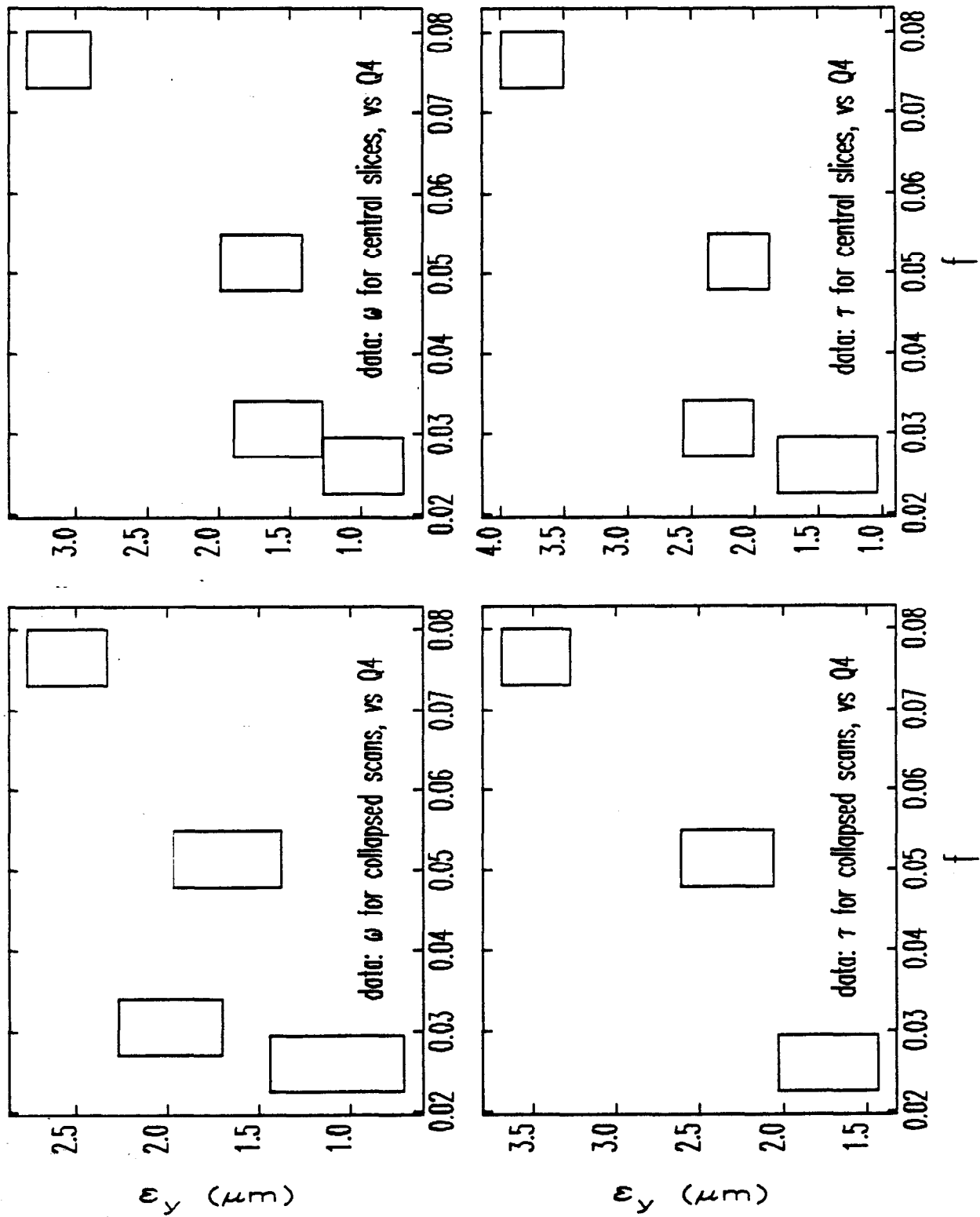


Figure 5.33: Vertical Emittance versus f (Momentum Spread) as Inferred from Variation of Q4.

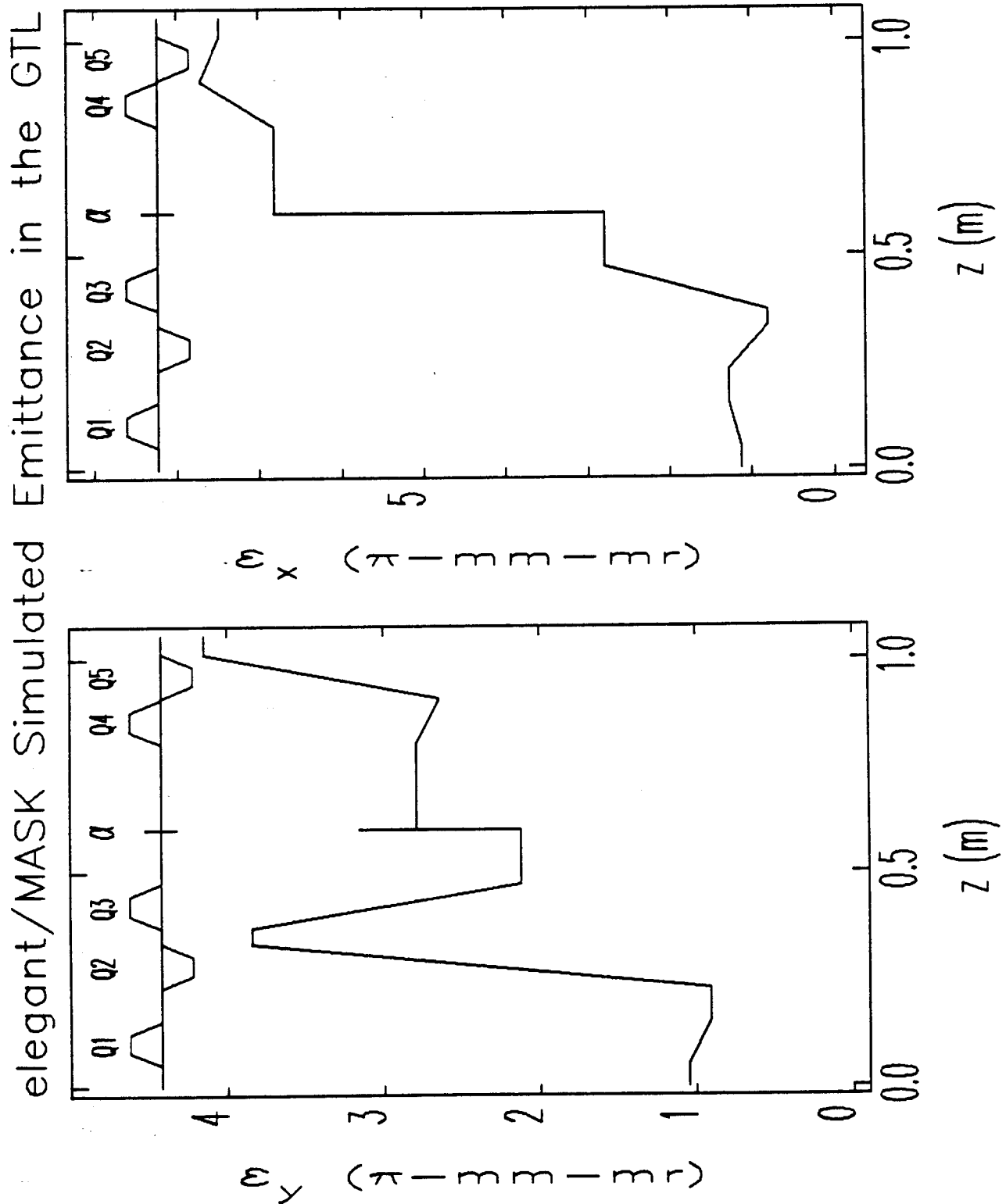


Figure 5.34: Variation of the RMS Geometric Emittance Along the Beamline for the Emittance Measurement Lattice with Q4 at 90 m^{-2} , from MASK/elegant Simulations.

experiments, Figure 5.34 shows an *elegant* simulation of the RMS geometric emittance in the x and y planes as a function of position along the beamline, where I have used the same optics as was used for the measurements (with Q4 set at 90 m^{-2}). The momenta of the simulation particles was pre-filtered in order to show the effect only of those particles that would actually exit the alpha-magnet, for $f = 0.08$. In addition, the data point at the center of the alpha-magnet is not shown, since the x emittance at this point is greatly inflated due to the dispersion. As discussed earlier in this chapter, one sees that chromatic aberrations have a dramatic effect on the emittance as the beam travels along the beamline.

Next, I show the effect of that variation of Q4 has on the emittance at the chopper screen (again, this is for $f = 0.08$). Specifically, Figure 5.35 shows the emittance for horizontal and vertical planes as a function of Q4, with Q5 set to zero, and in addition shows the emittance for Q4 set to 90 m^{-2} while Q5 varies. The emittances in these graphs are computed directly from the coordinates of the simulation particles after tracking through the beamline with *elegant*. Since the emittance is not constant as the quadrupoles are varied, it is a valid question whether obtaining the emittance by measuring the beam-size as a function of quadrupole strength is applicable.

To answer this question, I have run *elegant* for a series of alpha-magnet slit positions corresponding to those used in the experiment. *elegant* tracked simulated electron bunches for a series of values of Q4 (or Q5), dumping the transport matrix and the collapsed beam-sizes (both ω and τ) to disk for subsequent analysis with *emitmeas*.

Figure 5.36 shows the predicted variation of horizontal beam-size ω as a function of Q4 for $f = 0.08$, along with the experimental data to which the simulations correspond. (These beam-sizes are for the collapsed scans.) One sees that in general the simulation and experiment agree very poorly, with substantial agreement occurring only for ω_x versus Q4.

The differences are particularly dramatic for the vertical plane. In the experiments, the vertical beam-size went through a clear minimum as Q4 was varied. In the simulation, however, the beam-size does not go through a minimum in either case. This may well be related to the uncertainty in the alpha-magnet optics for the vertical plane. As discussed in Chapter 3, the effect of field errors in the alpha-magnet

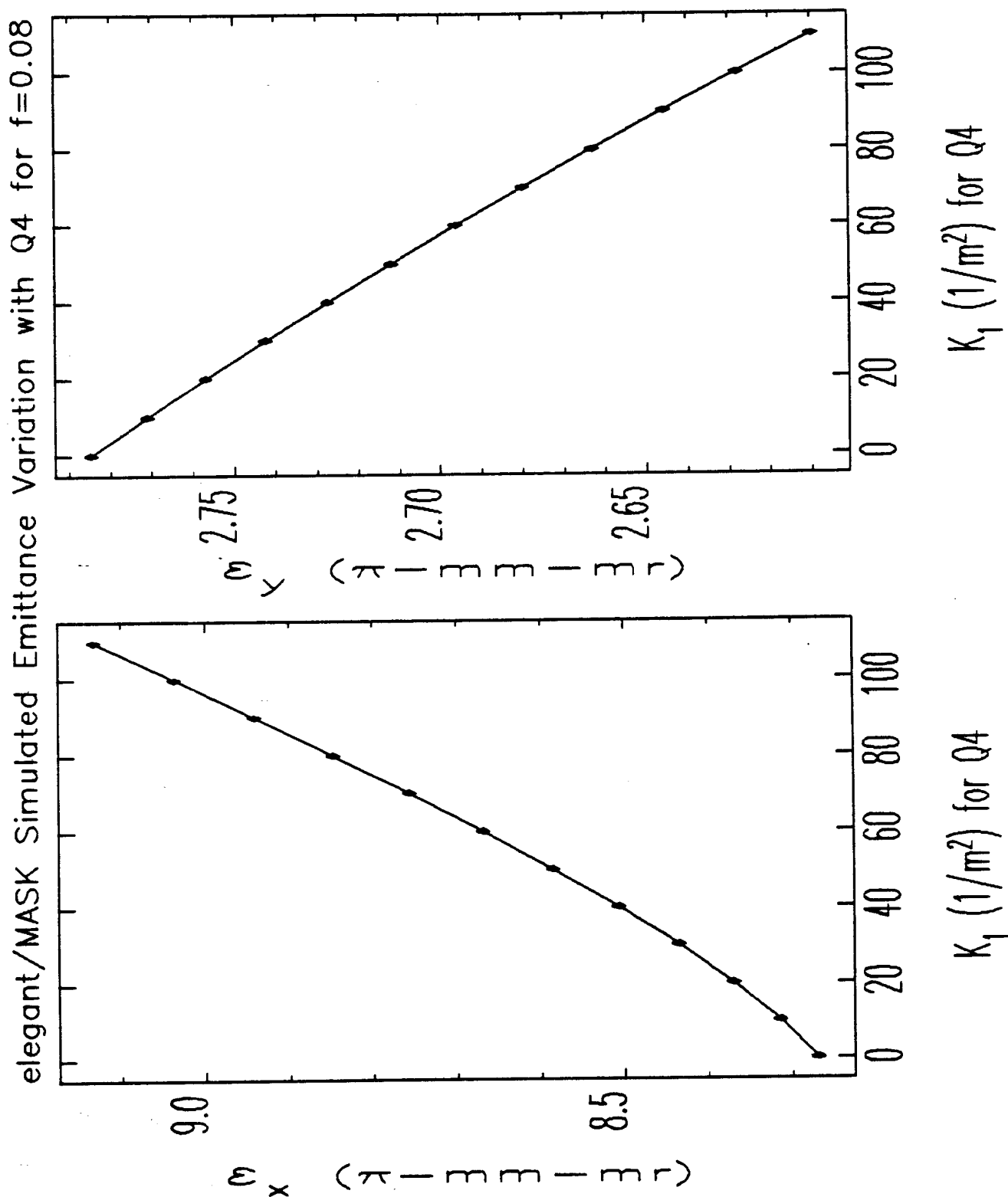


Figure 5.35: Emittance at the Chopper Screen as Altered by Q4, for $f = 0.08$, from MASK/elegant Simulations.

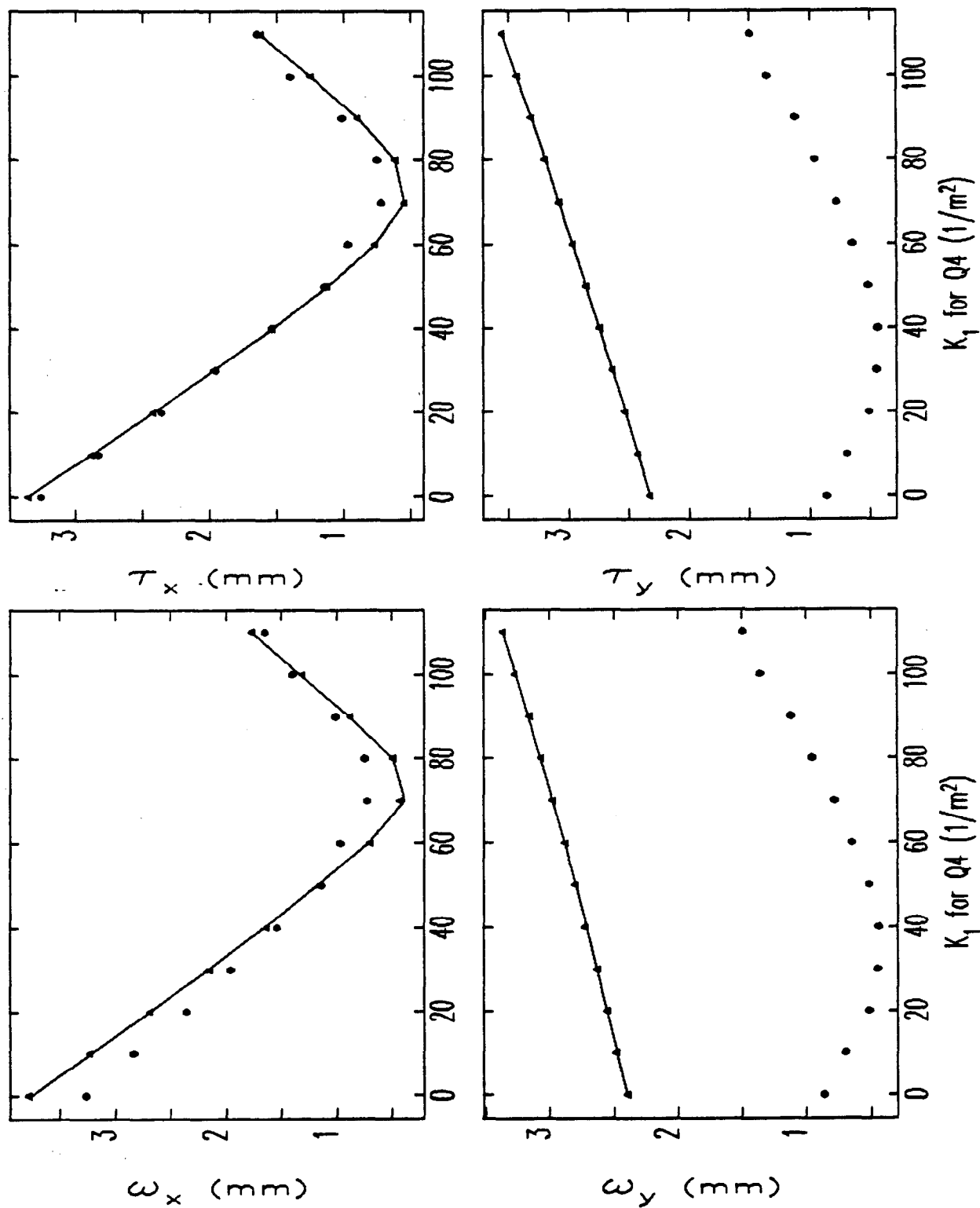


Figure 5.36: Beam-Size as a Function of Q4 Strength, from MASK/elegant simulations with $f = 0.08$

is much greater for the optics in the vertical plane than for the horizontal plane, and hence the correspondence between simulation and experiment may be expected to be worse for the vertical plane than for the horizontal plane. More work is needed to ascertain whether the known field errors in the alpha-magnet are sufficient to account for the observed discrepancy.

This does not mean, however, that the emittance measurements for either plane are invalid, since the emittance measurement depends only on the matrix from the beginning of the first varied element to the point of observation. Assuming that the errors in the alpha-magnet are only significant for the first-order matrix (an assumption I have not proved), the emittance would be unchanged, though the Σ -matrix would be altered. This would change the variation of beam-size with either Q4 as well, without changing the emittance that would be deduced from that variation.

Figures 5.37 and 5.38 show the emittance measurements for the collapsed scans (previously shown in Figures 5.32 through 5.33) along with simulation results obtained from *elegant*, *rfgun*, and MASK. As in the earlier Figures, the boxes represent the experimental measurements. The solid lines are the emittance as inferred from simulated measurements, using *rfgun*-generated initial particle distributions tracked by *elegant*, then analysed by *emitmeas*. (On some of the graphs, the solid line is missing because the beam-size did not go through a minimum, and the fitting failed.) The dotted lines are the upper and lower limit of the emittance in these simulations, indicating the variation of the emittance due to changing chromatic aberrations. Similarly, the dashed lines are the upper and lower limit of the emittance when MASK-generated initial particle distributions were used.

From Figure 5.37, one sees that use of ω as a beam-size measure is problematic, despite the appeal of the measure because of its robustness. I now refer specifically to simulation results, and the discrepancy between the emittance deduced from ω and upper and lower bounds on the RMS emittance computed by explicit averaging over the coordinates of the simulation particles. By contrast, in Figure 5.38 one sees that the emittance deduced from the RMS beam-size is generally quite close to the range through which the emittance actually varies in the simulation.

One would expect that as the momentum fraction was decreased, the inferred

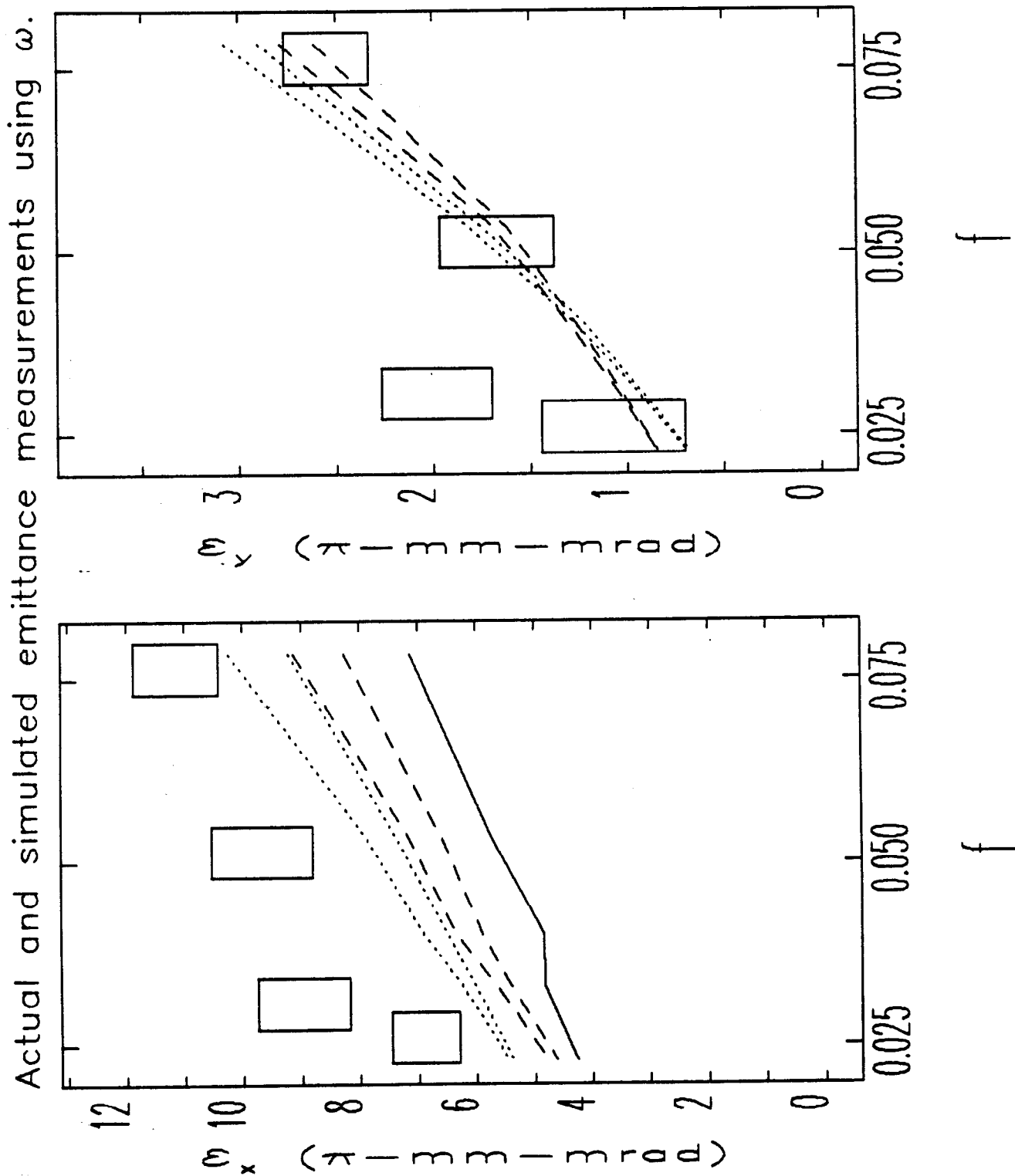


Figure 5.37: Emittance from ω vs. Quadrupole Strength, as a Function of Half-Momentum Spread, f , from Simulations and Experiment. (See text for explanation.)

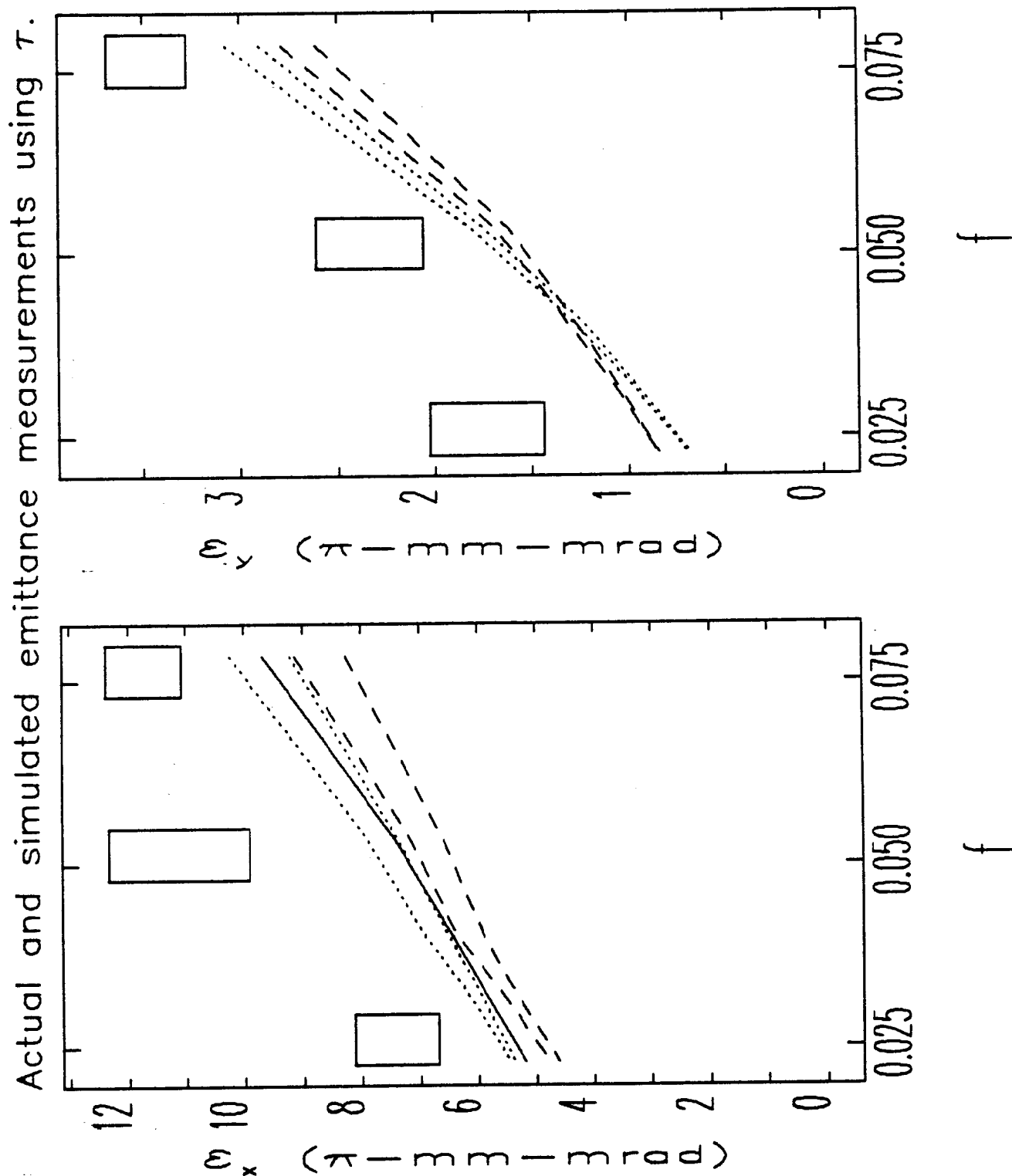


Figure 5.38: Emittance from τ vs. Quadrupole Strength, as a Function of Half-Momentum Spread, f , from Simulations and Experiment. (See text for explanation.)

emittance would approach the boundaries set by the variation of the explicitly computed emittance. From the Figures, one sees that this is not always true, even when τ is used as the beam-size measure. The reason is that, even for comparatively low momentum spreads (as low as $\pm 2.3\%$ in the simulations), there is still some dependence of the emittance on quadrupole strength. This is apparently sufficient to “throw off” the fits and make the emittance appear to be something different from what it actually is. I am confident that these results are not spurious, since `emitmeas` has been tested thoroughly using zero-momentum-spread simulation beams; in tests, the emittance for such a beam proved recoverable to the very high accuracy (limited by the fact that the data delivered to `emitmeas` was only good to single-precision accuracy). Note that the effects of momentum spread on the the emittance measurements are quite unlike the effects of noise, in that the latter do not cause systematic variations.

5.4.13 Possible Sources of Discrepancies

While there is some agreement between the simulations and the experimental results, the measurements on average give emittances that are 50% higher than the simulations predict. Possible sources of error in the emittance results stem from possible uncertainty in the position of the quadrupoles and in the calibration of the quadrupole strength (as a function of driving current). Simulations with `elegant` of the effect of errors in quadrupole strengths and positions show that these are relatively minor issues:

1. Motion of Q4 by ± 5 mm produces less than ± 5 % variation in the inferred emittance for either plane.
2. Motion of Q5 by ± 5 mm produces less than ± 10 % variation in the inferred emittance for either plane.
3. ± 10 % strength errors in Q4 produces less than ± 10 % variation in the inferred emittance for either plane.
4. ± 10 % strength errors in Q5 produces less than ± 13 % variation in the inferred emittance for the x plane, and less than $\pm 8\%$ variation for the inferred emittance for the y plane.

The effects of such errors are less than indicated by these results, since the positions are known to within a few mm and since the strength calibration is good to at least $\pm 5\%$. (Recall, however, that the quadrupole calibration was adjusted by 8% as a result of beam-optics tests, as discussed in a previous section of this chapter.)

In Chapter 2, I discussed the strong effect that non-linear fields in the gun have on the beam emittance. It is possible that if the cathode is not properly positioned, the character of these fields could be changed, thus leading to discrepancies between simulation and experiment. In particular, the non-linear fields would be expected to increase rapidly as the cathode is pulled back into the ceramic annulus. This issue requires further investigation.

Another possible explanation for the discrepancies, and one that I consider likely, is the excitation of other structure modes in the gun, leading to beating of the fields in the cells. Such beating (occurring at 50 MHz) has been observed in actual operation. In addition, the beam-sizes for the measurements are from averages over hundreds of bunches, so that the variation in current and bunch momentum during the RF pulse will effect the measured beam-sizes. That is, the phosphor responds to all electrons that reach it, and during any RF pulse this includes electrons from bunches emitted over several hundred nano-seconds (just how long depends on the experimental conditions, in particular the setting of the alpha-scraper). Both of these effects would increase the measured emittance through variation of the beam momentum (which would lead to different focusing in the quadrupoles and alpha-magnet) and through variation of the RF focusing in the gun. I have not attempted to quantify these effects.

While the experiments disagree with the simulations, “bottom-line” is that the emittance, in the presence of chromatic aberrations and other errors, has been found to be less than $12 \pi \cdot \text{mm} \cdot \text{mrad}$ in the horizontal plane, and less than $3.5 \pi \cdot \text{mm} \cdot \text{mrad}$ for the vertical plane. Depending on the momentum filtration employed, substantially smaller emittances can be obtained. The geometric mean of these upper bounds is about $6.5\pi \cdot \text{mm} \cdot \text{mrad}$, corresponding to a normalized emittance of $32 \pi \cdot m_e c \cdot \mu\text{m}$.

5.5 Bunch Length Measurement

In Chapter 4, I discussed the principle of magnetic compression, and made predictions of how effective the compression was expected to be. In particular, I predicted that bunch lengths of order 1 ps should be possible, with corresponding peak currents of several hundred amperes, depending on the current drawn from the gun. The SSRL preinjector consists of the GTL (described in an earlier section), followed by three SLAC-type linear accelerator sections and the linac-to-booster (LTB) transport line. The LTB features several bending magnets, the first of which (B1) is followed by an insertable phosphor screen ("the B1 screen"), allowing measurement of the momentum spread at the end of the linac with resolution as good as 0.02 %, depending on the adjustment of the quadrupoles between linac sections 1 and 2. (This resolution was determined empirically from the minimum beam-size achieved at the B1 screen.)

For the amount of RF power (2.6 MW) that was available for the gun as of this writing, the current reaching GT1 is limited to about 800 mA, with the momentum peak occurring at about 4 m_c. This corresponds to $E_{p2} \approx 60\text{MV/m}$ and hence an effective cathode area of about 5 mm², from which I infer that the current density is about 20 A/cm². Comparison with results of Chapter 4 would lead one to conclude that peak currents of about 200 A should be possible. However, the results of Chapter 4 were for $E_{p2} = 75\text{MV/m}$, which results in a higher-momentum beam ($p_{\text{peak}} > 5$) that is easier to compress than the lower momentum beams obtained when the gun is heavily beam-loaded.

Routine operation of the SSRL preinjector involves operating the gun at full RF power and with GT1 currents of 600-800 mA. About 2/3 of this current is allowed out of the alpha-magnet, and the full momentum spread at the end of the linac is typically less than 0.2 %. The momentum of the beam at the end of the linac is typically 200 m_c, giving $\Delta P \leq 0.4m_c$. This suggests that the bunch compression is working quite well, even for the initially low momentum beam from the fully beam-loaded gun. Ignoring the contribution of initial momentum spread and assuming $\beta = 1$ for the initial beam, I estimate the bunch length as 7 ps. This clearly over-estimates the bunch length, since it is known that the beam has significant initial momentum spread. I have not attempted to perform detailed simulations to investigate this

particular case further.

5.5.1 Principle of Bunch-Length Measurements

In order to get experimental verification of the bunch compression, I have made some bunch length measurements by employing the third accelerator section phased so that the center of the bunch receives no acceleration. Since the beam reaching the third section is already highly relativistic ($\approx 150m_e c$), one can approximate the effect of the third section by

$$\Delta p = \Delta p_3 \sin(\phi), \quad (5.80)$$

where Δp_3 is the momentum change that would be imparted to a relativistic electron passing through section 3 at the accelerating crest, and δp is the momentum change imparted to a particle at phase ϕ (relative to the null). (This is very similar to the equations of the first section of Chapter 4 for acceleration of an already relativistic particle, except that in Chapter 4, I referenced the phase to the RF crest.)

If the phase-length of the bunch is $\delta\phi$, centered about $\phi = 0$, then the resultant momentum spread for an initially mono-energetic beam is

$$\delta p = 2\Delta p_3 \sin(\delta\phi/2) \quad (5.81)$$

If the beam is not initially mono-energetic, the analysis is more complicated, and may depend on the detailed initial phase-space distribution of the bunch. However, if momentum spread imparted to the beam is large compared to the initial momentum spread, such effects can be ignored. By measuring δp as a function of Δp_3 , one can verify that the initial momentum spread is (or is not) inconsequential by verifying that δp depends (or does not depend) linearly on Δp_3 .

Because of this issue, for the experiments I have done and will report on here, I first phased sections 1 and 2 to obtain the minimum final momentum spread before varying Δp_3 . As seen in Chapter 4, this does not achieve the minimum bunch length, though it will produce a very short bunch. The bunch length also depends strongly on the alpha-magnet gradient, and hence it is necessary to select a gradient that is matched to the anticipated gun longitudinal phase-space.

It is convenient to rewrite equation (5.81) in terms of fraction momentum spread by dividing by the central momentum, p_o :

$$\frac{\delta p}{p_o} = 2 \frac{\Delta p_3}{p_o} \sin(\delta\phi/2). \quad (5.82)$$

Δp_3 is varied, of course, by varying the RF power level in section 3. This is quantified (see Chapter 4) as

$$\Delta p_3 = 20.4 \sqrt{P_3(\text{MW})}, \quad (5.83)$$

where P_3 is the RF power to section 3.

5.5.2 Practical Considerations

While the principle of the measurement is simple, its execution is less so on the SSRL preinjector, due to a number of factors:

1. At the time of this writing, there are still problems with pulse-to-pulse jitter in the RF power level, which can cause the beam on the B1 screen to jitter by more than the width produced by the momentum spread. This problem was circumvented by using the LeCroy 9450 oscilloscope to grab frames from the TV camera, each of which contains the image produced by a single beam pulse.
2. There is no way to determine the RF phase of the individual sections, or to ensure that the phases are held constant during the experiment. Long-term drifts in the modulator HV can cause drifts in the individual RF power output levels and phases of the individual klystrons. The only solution to this at present is to do each measurement as quickly as possible.
3. The RF phases are referenced to the phase of the second section, as discussed earlier in this chapter. Hence, optimization for the best alpha-magnet gradient to compress a given beam from the gun would involve rephasing the RF for the gun and sections 1 and 3, which can be very time-consuming. Ideally, a single control would be available to simultaneously vary the RF of all three sections relative to the gun. (The reason there must be any RF re-phasing at all is that changing the alpha-magnet gradient varies the path-length, and hence the time-of-flight, between the gun and linac.)

4. The phase-shifter for section 3 has a significant phase-dependent insertion loss, so that phasing the section to the phase null can be difficult. To verify that the section is phased at the null, one must vary the power into the section and verify that the central beam momentum is unchanged. If the section is not at a null, the phase must be varied until the null is found. Unfortunately, upon changing the phase, the insertion loss changes, which can cause the beam to jump in momentum, requiring the experimenter to vary B1 in order to find the beam again. In addition, the phase shifter shows significant hysteresis, further complicating the optimization.

Time permitting, one would vary the gradient and rephase the accelerator sections, and measure the bunch-length as a function of gradient. There was insufficient experimental time to do this (the experiments took place during the commissioning of the 3 GeV Booster, which required dedicated operation of the linac for injection into the booster). The results I will report on here thus do not represent the optimized compression of the bunch, but only the best that I achieved in the few experiments that were conducted.

5.5.3 Experimental Results

Figure 5.39 shows the experimental data for the most optimum conditions achieved. Plotted here is the fractional momentum spread versus $\Delta p_3/p_0$, where p_3 is again the maximum available momentum gain from section 3, as deduced from RF power measurements. The three sets of data are for three different positions of the alpha-scraper, so that different fractions of the beam are let through for each set, as indicated by the value of Q printed with the data. The Figure also gives the bunch-lengths deduced from the data, using the fits shown with the data points. The momentum spreads plotted here are FWHM values, which, because of the shape of the momentum distribution at the end of the linac, contains more than 90% of the beam.

The peak-current, defined as

$$\hat{I} = \frac{Q}{\delta t}, \quad (5.84)$$

is a measure commonly employed for rating the suitability of a beam to applications requiring high-brightness. From the data given in the Figure, one sees that the highest

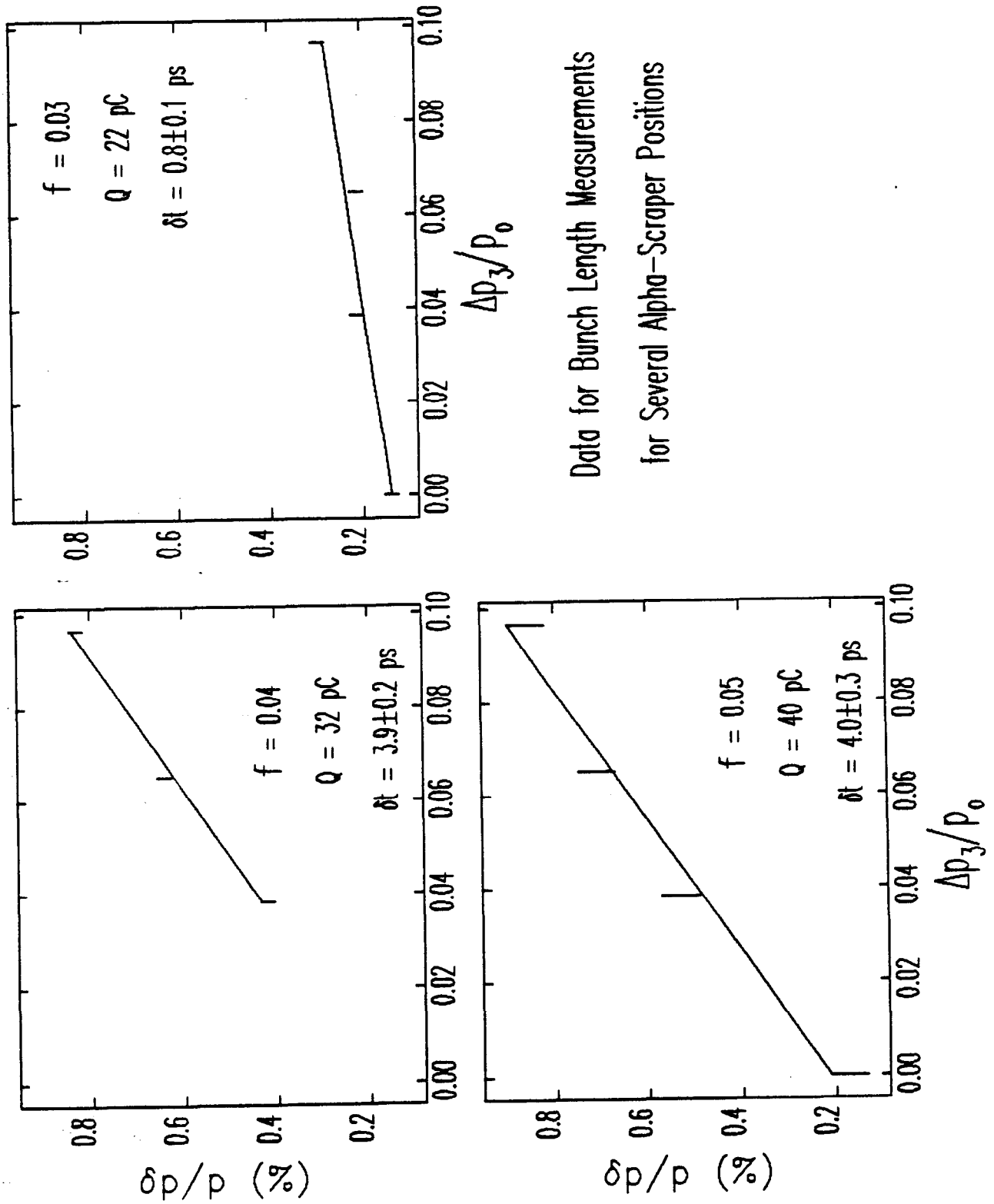


Figure 5.39: Data for Bunch-Length Measurements for Various Momentum Fractions Allowed Through the Alpha-Magnet

measured peak current is 28 ± 3 A. The current to GT1 in this case was 395 mA, which corresponds to 180 pC per bunch. Hence, in order to obtain this high peak-current, it was necessary to allow only 12% of the beam through the alpha magnet, corresponding to an initial momentum spread of ± 3 % (i.e., $f = 0.03$).

The peak-currents for the other two data sets are about 10 A, which is a value that was reproduced in several other measurements as well. While these peak-currents, even the 28 A, are significantly less than the predicted optimum performance of the system, it is clear that too little work has been done to date to conclude that the predictions are inaccurate. It is hoped that others will pursue this work with additional experiments.

5.5.4 Comparison with Simulations

The peak momentum of the bunch from the gun, as measured with the alpha-magnet scraper, was 4.4 m.c, which implies $E_{p2} \approx 65$ MV/m. Beam-loss simulations using *elegant* and a MASK-generated initial particle distribution predict 85% transmission from the gun to GT1, implying that the current out of the gun was 464 mA. Since the effective cathode area for $E_{p2} = 65$ MV/m is 4.7 mm^2 , the current density is inferred to be about 10 A/cm^2 . Hence, simulations of the bunch compression for comparison with experiment should use MASK-generated data for $E_{p2} = 65$ MV/m and $J = 10 \text{ A/cm}^2$.

In order to ascertain how close the experimental results are to what could have been achieved, and also to see how sensitive the bunch-length is to the alpha-magnet gradient, I have used *elegant* to compute the bunch length and other parameters at the end of the first section for a series of alpha-magnet gradients, using the just-mentioned MASK data. Figure 5.40 shows the results for a momentum fraction of 0.03. The alpha-magnet gradient for the data shown in Figure 5.39 was 189 G/cm. The conclusion is that the compression is roughly consistent with simulations for $f = 0.03$. One sees from the Figure that the bunch length is quite sensitive to the gradient, and in particular that a 5% increase in the gradient from 190 G/cm would have decreased the bunch length by a factor of about 2.

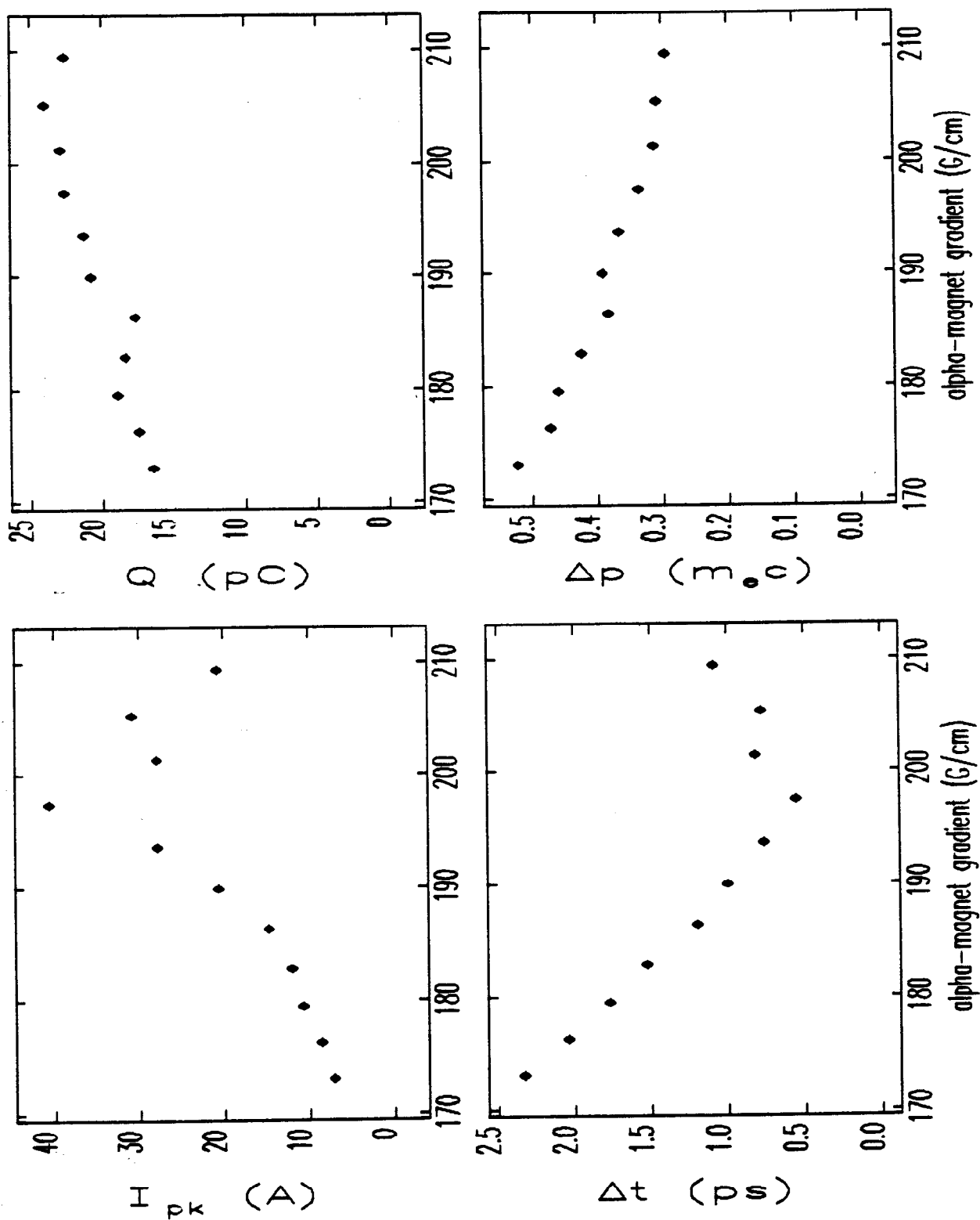


Figure 5.40: elegant/MASK-Simulated Beam Parameters After First Linac Section vs Alpha-Magnet Gradient for $f=0.03$, ($E_{p2} = 65\text{MV/m}$, $J = 10\text{ A/cm}^2$).

Appendix A

Computational Issues and Techniques

As the reader has no doubt noticed, I have made extensive use of computers in the research reported on in this thesis. I wrote much of the software that I used while at SSRL, and, since it has not been described in any publications, I am adding this appendix to acquaint the reader with some of this software. Much of it is of very general application, and this appendix will act as partial documentation. In the course of my descriptions, I will also comment on several issues pertinent to the use of computers in physics and to the state of the programs used by the accelerator physics community.

Part of my philosophy in doing research is that it is better to spend time writing a program that does a task than to do that task manually (using a hand-calculator, say), since the program will then be available to immediately solve the problem the next time. Though writing the program may take more time than solving the original problem, in the long run one gains in productivity through repeated use of the program. Because my goal in creating programs is to produce a tool for future use, I attempt to make each program solve a much more general form of my particular problem. In addition, I try to make the program as convenient and flexible as possible, to minimize the need for changes.

Some physicists have disdain for programming, an attitude I do not share. Programming is no different from solving differential equations, both being tools for solving problems. It would be as silly to look down on solving differential equations as it is to look down on programming. Computer programs differ from analytic approaches in that they are more easily misused and more easily used by those with little understanding, i.e., they are more easily used or misused by those who don't understand physics. This is not, however, an indictment of computer methods, but of those who abuse them.

One of the worst aspects of many of the programs used by accelerator physicists today is the user-interface. Many programs still require the user to type in rows of numbers, often in a rigid format, and still spit out row after row of numbers in tables spanning pages of fan-fold paper. These programs make little use of the computer's ability to talk to the user on *his* terms and to present the results in a way that aids the physicist's understanding. The user is left on his own to produce graphical or alternative representations of the results.

There are, of course, many programs that serve the physicist's needs much more satisfactorily. For the most part, these programs make use of a custom-designed user interface, so that the data from one program must be "post-processed" (e.g., plotted) with the aid of an auxiliary program written just for the physics program in question (or for some small group of programs). Examples of such codes are the standard version of MASK (which does all graphics internally and writes all other data in a single output file) and the POISSON group programs (which share a common, though incomplete, graphics program TEKPLOT, along with common pre-processors and some program-specific post-processors).

I consider this duplication of effort to be wasteful and to unnecessarily complicate the use of programs. In response to this problem, I have created three standardized data formats that are suitable for use in almost all applications. The simplest format—called `mpl` format after one of the primary programs that uses the format—is used by a large group of inter-communicating programs called the `mpl` Scientific Toolkit. The other two formats, the `dpp` and `column` formats, are self-describing data formats that are used to store and manipulate data, selected elements of which can then be written to `mpl` data sets for use with the Toolkit.

Physicists should not disdain to be involved in the design of the user interfaces for the programs they will use, for it is the requirements of doing physics that should dictate the design of the user interface. A program with an inflexible, inconvenient user interface forces the physicist to deal with tedious matters rather than the physics of the situation; writing such a program is bad physics as well as bad computer science. I believe that the ideas described in this appendix, and the programs that implement them, represent a significant step toward a more universal user interface for scientific programs.

`mpl` and `awe` formats and the principle programs that use them are described in more detail in a following sections. For now, I will describe each briefly. `mpl` format is essentially a series of (x, y) pairs, with optional uncertainties, and hence is not appropriate for storing all types of data. For a great many applications, however, this is not a serious limitation, and the simplicity of the format makes it a good choice.

The most sophisticated format, `dpp` format, is used for the output from many simulation programs. It consists of a header that gives the names and units of the

quantities in the file, together with the names and units of "auxiliary quantities". After the header, there follows a series of "tables", each consisting of values for the auxiliary quantities and an arbitrary number of rows of data, with each column of the table containing values for one of the named quantities. (For example, the quantities might be phase-space coordinates (x, x', y, y') , with the auxiliary quantities being the time and z coordinate.) A sophisticated post-processing program, `dpp`, is available to access and manipulate the data in `dpp` format files (which are not human-readable), allowing the user to select the data of interest, create new quantities by defining them in terms of existing quantities, and much more. `dpp` can create human-readable tables and, in its most common application, `mpl` data sets for use with the `mpl` Toolkit.

`column` format is intermediate between `mpl` and `dpp` formats. Like `mpl` format, it is human-readable, but like `dpp` format, it has a self-describing data structure that supports any number of data elements in a table. The programs `column` and `sheet` (a spread-sheet program) are available to manipulate data in `column` format and to create `mpl` data sets of selected sub-sets of the data in a `column` data set. `column` format has the disadvantage that it is cumbersome and inefficient for very large data sets, which are best stored in `dpp` format.

At this time, the programs that make use of these formats are available only on SSRL's VAX 8810 computer. I anticipate making the first release of the `mpl` Toolkit, `dpp`, and other of my programs (such as `rfgun` and `elegant`) in the near future.

A.1 The mpl Scientific Toolkit

The mpl Scientific Toolkit is a group of programs, written in the C programming language[91], sharing a common data file format. The Toolkit is a powerful aid to a scientist's use of computers, alleviating much of the tedium associated with the analysis and interpretation of data. While I developed the Toolkit in the course of the research reported on in this thesis, the programs are of much more general application.

Each of the programs in the Toolkit was developed in response to a specific need in my research. However, my philosophy in implementing each program was to try to generalize my particular problem, then to write a program to deal with this more general problem. While this involves more effort at the outset, I have found that it produced great productivity benefits in the long run, since the Toolkit is now sufficiently complete that a great many tasks can be performed using some combination of programs from the Toolkit.

In order to enhance the productivity of the Toolkit, the programs not only use mpl format (described below) for their input data, but they also create new data sets in the same format, when it is at all meaningful to do so. Hence, one can perform a sequence of operations on one's data by invoking a sequence of Toolkit programs.

An alternative to the Toolkit concept would be a single, integrated program that incorporated all of the functions of the individual Toolkit programs. I believe such a system is unwise, in that it locks the user into the capabilities that are put into the program by the programmer. With the Toolkit concept, the user can readily write his own programs to augment the Toolkit as needed, without any change in the way he uses the member programs. In addition, individual Toolkit programs can be improved or replaced, and new Toolkit programs can be added, without altering other parts of the Toolkit or recompiling and redistributing a massive new version of the complete code. Finally, the user is not forced to abandon the system command environment, so he is left free to interleave Toolkit program calls with calls to system programs, as his needs dictate.

The user-interface for the programs is command-line based, rather than menu-based or query-based. That is, with some exceptions among older or more complicated

programs, the programs in the Toolkit are executed by typing the program name followed by a list of command-line options. This makes the programs more amenable to use in batch-files and allows argument substitution through the command language. It also caters to the experienced user and his productivity, at the expense of making things slightly harder on the novice.

An `mpl` data set is an ordinary text file, such as might be created using a text editor. The lines of the file are read and processed one at a time, and no line may be longer than 1024 characters. The first four lines are descriptive text (as opposed to numeric data). The first line should be the name of the abscissa (or "x" variable), while the second line should be the name of the ordinate (or "y" variable). The third and fourth lines will be placed at the bottom and top of the plot, respectively, when the data set is plotted with `mpl` or `dpl`.

The fifth line contains the number of data points in the data set. It should be equal to or larger than the number actually in the data set. A warning will appear if this number is different from the actual number of points. The program `fixcount` is available to count the points for you and put the right number on the fifth line of the data file.

Subsequent lines each contain one data point, which consists of two through four numbers. The first two values are x and y, respectively. If there are three values, the third is interpreted as the uncertainty (or sigma) for the y value. If there are four values, the third is interpreted as the x uncertainty, and the fourth as the y uncertainty. The number of values that are taken from each line is established by the number of values given for the first data point. The data set ends when the file ends, or when the number of points specified has been reached, whichever comes first.

The format of the data is very free. Any non-numeric ascii character (i.e., any character other than a digit, a plus or minus sign, or a period) can be used as a separator between data elements on a single line. Spaces and tabs are preferred, but solely for aesthetic reasons. Any line beginning with an exclamation point is treated as a comment, and ignored.

What follows are short descriptions of the programs in the `mpl` toolkit at this time. A few of these programs are for very specific applications, though most are of general application. Some are quite simple, a few are downright trivial, while others

are very sophisticated. What really matters is that they are all useful, easy to use, and interlinked by the common data format.

This list does not constitute a user's manual for these programs. Rather, the programs are intended to be self-documenting, since each program will respond with help information if it is run improperly. Hence, the user may obtain help for any program simply by running the program without any command-line input. The general form of the "usage message" that each program responds with is

```
usage: program_name required_argument1 required_argument2 ...
      [optional_argument_1] [optional_argument_2] ...
      {choice1.1 | choice1.2 | ...}
      {choice2.1 | choice2.2 | ...}
      [{optional_choice1.1 | optional_choice1.2 | ...}]
      [{optional_choice2.1 | optional_choice2.2 | ...}] .
```

In words: required arguments (e.g., the name of the input data set) are listed without delimiters. Optional arguments (usually a program-control "switch", or an optional output filename), are delimited by square brackets. Sets of arguments that the user *must* choose one and only one of are grouped by curly braces and separated by vertical bars. Optional sets of arguments that the user may choose one (and only one) of are grouped by curly braces inside square brackets. An example of a usage message is given below.

Options, or "switches", are of the general form

```
-keyword[=value1[,value2...]],
```

with several alternative forms recognized (you may use / instead of -, and : or , instead of =). Any keyword may be abbreviated when entered on the command line, so long as enough characters are supplied to make the keyword uniquely identifiable. If the value listed in the usage message has single quotes around it, then the value must be typed literally (i.e., as in `-average=rms`); you should not type the single quotes yourself in running the program. Such values may, like the keywords, be abbreviated. In contrast, a value listed in double quotes represents a string that *may* need to be enclosed in double quotes (if, for example, it contains spaces, as in `-title='x vs`

y''). Illustrations of the calling syntax appear below. Note that `dpp` and the other programs described in this appendix employ the same command-line interface.

In what follows, the phrase “data set” refers to data stored in an `mpl` format file, which consists of a set of data points (x_n, y_n) with optional uncertainties σ_{y_n} and σ_{x_n} . Unless otherwise stated, each program writes its results as a new data set in a file of the user’s choice.

add: Adds (or subtracts) two data sets, with error propagation. Normally, the ordinates are added assuming that the abscissae match. Optionally, the abscissa can be added. There is also an option to match the abscissae before adding the ordinates, or vice-versa.

average: Performs averages of either column of data in a set of data sets, creating a new data set with the ordinates given by the averages, and the abscissae given either by the user or by incrementing a counter.

column: Extracts data from generic tables, such as might be output by any number of programs, and creates data sets. Hence, a program that prints rows of quantities in many columns can be interfaced to the Toolkit via `column`. (A better way to accomplish this is to modify the program to write its data in either `mpl` or `dpp` format.) Also, `column` extracts data `column`-format files into `mpl`-format files.

combine: Combines any number of data sets into a new data set, sorting the data sets by the first abscissa value in each set.

conpair: Performs the discretized convolution of a pair of data sets.

conap: Convolve a data set with a square aperture.

deriv: Takes the derivative of a data set, using

$$\left(\frac{\partial F}{\partial x} \right)_{x=x_a} \approx \frac{F(x_{n+m}) - F(x_{n-m})}{x_{n+m} - x_{n-m}}, \quad (1.1)$$

where $x_a = (x_{n+m} + x_{n-m})/2$ and where m is specified by the user. Strictly, the points should be equispaced (if not, use $m=1$).

dpl: Simple plotting program for a single mpl-format data set. See **mpl** for a more sophisticated program.

ellipse: Generates an mpl-format data set containing (x, y) points on an ellipse, given the Twiss parameters and the emittance.

filter: Performs digital filtering of a data set by doing an FFT, applying the filter, then doing an inverse FFT. Supports low-pass and high-pass filters with linear roll-off, as well as Parzen windowing[61] of the data.

fixcount: Fixes the point count of data sets. **fixcount** will attempt to simply overwrite the existing point count, if the fifth line of the data set has a sufficient number of characters to allow this without over-running onto the next line stored in the file. E.g., if the fifth line contains '1<return>' and the actual point count is 100, **fixcount** will have to re-write the entire file to make room for the two zeroes. If, however, the fifth line had contained '1 <return>', **fixcount** would over-write two of the trailing spaces with zeroes. This is not a trivial concern for data sets with thousands of points, and hence it is a good idea to put trailing spaces on the fifth line of each data set.

fft: Performs the FFT of a data set, producing a new data set with the magnitude vs. the frequency. Also does optional Parzen windowing[61] and provides output of real and imaginary components. Will work in either single or double precision, and will optionally pad or truncate your data to achieve 2^n data points (necessary for the FFT).

fwhm: Computes the full-width at half-maximum, with optional smoothing.

gfit: Fits a gaussian to a data set, finding the sigma, mean, baseline, and height, with the option of generating a new data set containing the fit evaluated at a series of points.

ggen: Generates a data set from evaluation of a gaussian at equispaced points.

hist: Makes histograms and cumulative distributions of one or more data sets, with optionally weighting of the histogrammed variable by the other variable.

integ: Computes the integral of a data set using the trapizoid rule with error propagation, creating a new data set with the integral as a function of the abscissa.

interp: Does polynomial interpolation on a data set, using whatever order of polynomial the user requests, with options for creating a new data set with interpolated values at equispaced points and for transforming one variable of a data set via interpolation on the first data set.

lsf: Does error-weighted least-squares polynomial fits to any order . Options for fitting only even or odd polynomials, or for fitting only specified powers. Also provides difference data sets and data sets from evaluation of fitted polynomials.

mpl: Versatile plotting program for multiple data sets. Allows zooming, point plotting, symbol plotting, and much more. Supports many common graphic output devices through use of SSRL's GHOST package. Has Greek and scientific character sets, with subscripting, superscripting, and in-line control of character attributes. The following "escape sequences" are recognized in character strings (these will be illustrated below):

1. \$g, \$r : switch to Greek or Roman characters.
2. \$a, \$b, \$n: go to Above (superscript), Below (subscript), or Normal script.
3. \$s, \$e: Start and End Special (mathematical) symbols.
4. \$i, \$d: Increase ($\times 1.5$) or Decrease ($/1.5$) character size.
5. \$t, \$f: go to Taller or Fatter letters (these are inverses of each other).
6. \$u, \$v: displace text vertically Upward or downward (respectively) by one-half character-height.
7. \$h: back-space one-half character width.

(mpl-format data sets and these character sequences are also recognized by my **draw** program, which was used to create all but a few of the graphs in this thesis. **mpl** is actually called as a subroutine in **draw**.)

mult: Does pair-wise multiplication (or division) of the ordinates (or abscissae, or both) of two data sets, with error propagation. If the data sets are of unequal

length, the program will optionally try to line up the abscissae before multiplying.

merge: Merges two data sets, in the sense of taking the abscissae and ordinates of the new data set from the abscissae and ordinates of two other data sets, as specified by the user. (The strange spelling is to avoid confusion with the VAX/VMS MERGE utility.)

params: Computes many parameters of a series of data sets, including positions, heights and sharpnesses of peaks, positions and values of minima and maxima, averages, and medians.

peakfind: Finds peaks in a data set, with optional smoothing and a user-defined threshold.

qsort: Sorts a data set into ascending (or descending order) by the abscissa, sub-sorting by the ordinate, with optional elimination of duplicate points.

rescale: Arguably the most powerful program in the toolkit. Performs very versatile transformations of a data set, including normalization, centering, scaling and offsetting, taking the logarithm, and more. Data sets may be sparsed, windowed, re-ordered, and the abscissae and ordinates may be swapped. Propagation of errors can be performed if sigmas are given in the data set. **rescale** will also accept user-defined transformations, specified as equations (this was done by incorporating my programming language/calculator **rpn** into **rescale**, just as it was incorporated into **dpp**).

rndgen: Generates random-number pairs, with gaussian and uniform distributions supported. The random number generator uses a random shuffling routine with two linear congruential generators[61].

smooth: Smooths a data set by multi-pass averaging over adjacent points.

setlog: Performs set logic on two data sets. For example, **setlog** will find all the data points in one data set but not the other, or all the data points in both

sets. User-specified tolerances are accepted to determine when two points are "the same".

stats: Does statistical analyses of a data-set, computing various moments, widths, and cumulative distribution parameters. Also gives the minimum, maximum, and spread.

total: Creates a new data set with

$$\tilde{y}_n = \sum_{i=1}^n y_i \quad (1.2)$$

zerofind: Finds locations of zeros in a data set, with interpolation between points.

Next, I present a simple example session making use of some programs in the `mpl` Toolkit. In particular, this is the sequence I used to create the data for the comparison of linear and non-linear field terms in Chapter 2. Recall that I compared $E_z(z)$ (the on-axis longitudinal field) with

$$T_1(z) = \frac{R_c^2}{8} \left[\partial_z^2 + k^2 \right] \frac{E_z(z)}{E_{p2}}, \quad (1.3)$$

where $R_c^2 = 0.3$ cm. The starting point is a data set containing $(z_i, E_{z,i})$ with z in meters, as previously extracted from a SUPERFISH-generated output file (which could be done using `column`). Lines preceded by exclamation points are comments. Lines in italic type are output from a program, while those in type-writer type are typed by the user:

```
! The initial data set is z_ez.sfish. Normalize it to a peak value of 1 and convert
! the abscissae from cm to m. The names of the data columns are also changed,
! using a subscript escape sequence to obtain E_norm. Note the use of the
! ampersand as a command-line continuation character:
$ rescale z_ez.sfish z_ez.out -normalize -x_divisor=100 &
$ -y_label="E$bnorm$n" -x_label="z (m)"
! Find out how to use the deriv program:
$ deriv
```

*usage: deriv inputfile outputfile [-interval=number] [-x-sigma=value]
[-y-sigma=value]*

! Take its derivative, using a derivative interval of 2 points:

```
$ deriv z_ez.out z_dez1.out -interval=2
```

! Take the second derivative as well. Abbreviate the command somewhat:

```
$ deriv z_dez1.out z_dez2.out -int=2
```

! Compute $k^2 E_z$, where $k = 2\pi/\lambda$ and $\lambda = 0.105\text{m}$.

! The y-axis label is changed to " $k^2 E_{\text{norm}}(1/\text{m}^2)$ ".

```
$ rescale z_ez.out z_k2_ez.out -y_transform="y k2 *" &
```

```
-rpn_expression="2 pi * 0.105 / sqr sto k2" &
```

```
-y_label="k$a2$n E$bnorm$ (1/m$a2$n)"
```

! Add $\partial_z^2 E_z$ and $k^2 E_z$

```
$ add z_dez2.out z_k2_ez.out sum.out
```

! multiply by $R_c^2/8$, with abbreviation of command-line options

```
$ rescale sum.out t1_nonlin.out -y_t="y C *" &
```

```
-rpn_ex=".003 sqr 8 / sto C" &
```

```
-y_label="T$b1$n" &
```

! An alternative form of this command, that is quicker

```
$ rescale sum.out t1_nonlin.out -y_multiplier=1.125e-6 &
```

```
-y_label="T$b1$n"
```

! Compare E_z and T_1 by graphing on a VT100-series terminal (GHOST device 3),

! using different intensities for the two data sets.

```
$ mpl t1_nonlin.out,z_ez.out -multipen
```

! Repeat, but expand around the end of cell 1 ($z = 0.026\text{ m}$), with auto-scaling of

! the vertical extent of the plot.

```
$ mpl t1_nonlin.out,z_ez.out -multipen -scale=0.024,.028,0,0
```

Special note to FORTRAN users: VAX FORTRAN (and perhaps other implementations as well) uses, by default, the FORTRAN-carriage-control record structure for output files. C uses stream files, which by definition have no record structure. The VAX C library is supposed to provide translation between the different record formats in an invisible way, but does not do so properly for FORTRAN-carriage-control files. Hence, if you wish to generate mpl data sets from FORTRAN programs, you should

open the output file using the following syntax:

```
open(unit=unit_number, name=filename, status='new',  
      carriagecontrol='none', recordtype='stream_cr')
```

A.2 The awe Self-Describing Data Format

I created **awe** format from the realization that most output from scientific programs can be organized into tables. The columns of a table contain quantities having the same name and units, while each row contains quantities that are grouped together. For example, the columns might be z , E_z , E_r , and B_ϕ , so that a row would contain the latter three quantities as a function of the first. **awe** format consists of a header that gives the names and units of the columns, plus additional information (names and units of "auxiliary quantities") that pertains to all the data in the table. After the table-format is defined for a particular file, any number of tables in that format may follow, distinguished by a counter and (optionally) by the values of the auxiliary quantities. There are no internal limitations on the number of rows, columns, or tables that may be present in the data file; this is limited only by the memory capacity of the machine.

The program **awe** (for Dump Post-Processor) provides a universal user-interface to any program that creates **awe**-format output files. By using the unformatted representation of numbers, **awe**-format escapes the problem that many programs fall prey to, namely, the necessity of having to print fewer and fewer significant figures as more columns are added to the table, with the attendant problems whenever any numerical quantity exceeds the allowed format width. In addition, unformatted output is much faster and more efficient in terms of data storage, an important consideration for programs (like MASK and **elegant**) that dump very large amounts of data. This has the disadvantage that **awe**-format files are not human-readable, as common text format output is. Hence, among other things, **awe** provides the user with the means to create readable, text files in very flexible ways. **awe** permits the user to create his own text files with tables of just the data he is interested in. **awe** also produces **mpl**-format files containing data of the user's choice; this is the most common use of **awe**, since it is by this route that graphical output can be obtained. **awe** performs a variety of data manipulations, such as selecting subsets of a data set, calculating new quantities using user-supplied equations, and taking averages, to name a few.

For example, as discussed in Chapter 2, MASK dumps the quantities $(r, z, \beta_r, \beta_z, t, \gamma)$ for any macro-electron that crosses certain user-defined z planes. If one wishes to plot

t vs. γ (or any other pair of quantities) the program **awe** will create an **mpl**-format file from MASK's **awe**-format output. This same **mpl**-format file can be used to create histograms, graphs, as input to statistical analysis programs, and so forth, using programs from the **mpl** Toolkit.

awe also allows one to define new quantities that are functions of the quantities stored in a **awe**-format file. Hence, if one was more interested in the phase than the time-of-exit, this could be defined in terms of t . New quantities (calculated from equations given by the user) are on an equal footing with the quantities stored in the file. Hence, the physicist does not need to pore over computer printouts, calculator in hand, in order to put a program's output into the form he needs, nor is it necessary to write a new program to perform this task. **awe** supports a full range of scientific functions (from simple arithmetic operations to integer-order Bessel functions and complete elliptic integrals), and will also accept user-defined functions stored in a function library.

I have implemented **awe**-format output for MASK, **rfgun**, PARMELA, SUPERFISH, POISSON, **elegant**, **emitmeas**, and **serrors**, among other programs. Using **awe**-format for MASK also allows direct use of MASK output in my tracking code **elegant** and several other codes. Since **rfgun** and my version of PARMELA (see chapter 3) both use **awe** format as well, it is possible to write post-processing procedures and programs that work equally well with data from any of these programs.

The following is the usage message printed by the current version (December 1990) of **awe**, using the same syntax conventions as was used for the **mpl** programs in the last section:

```
usage: awe data_file {output_file | outputfile_root}
      [-dumps=dump_numbers,...] [-separate_dumps] [-verbose]
      [-sample_interval=number] [-average_over_dump[={rms|sum}]]
      [-log_file=filename] [-format="C-style format string"]
      [-define_quantity=quantity_name,quantity_unit,"rpn-expression"]
      [-filter=quan_to_filter,lo_limit,up_limit,pair_or_seq_numbers_to_filter]
      [-sort=quan_to_sort_by,number_to_keep[, 'descending']]
      [-rpn_expression="rpn-expression-to-execute-first"]
      [-rpn_defns_file=filename]
```

```

{ -first=quantity_name[=alias],...
  -second=quantity_name[=alias],...
| -sequence[=auxiliary_name[=alias]]
  -quantity=quantity_name[=alias],...
| -contour_grid=min1,max1,min2,max2,n1,n2[, 'combine'][, 'simple']
  [-n_contours=number] -first=quantity_name
  -second=quantity_name -quantity=quantity_name[,...]
| -table=filename,quantity_name[,quantity_name,...]
| -list_quantities
}

```

Description of non-self-explanatory arguments:

- {`outputfile` | `outputfile_root`}: The name of an output file to be created, or a partial output filename from which output filenames will be constructed.
- [`-dumps=dump_numbers,...`] [`-separate_dumps`] [`-verbose`]: Allows specification of the “dumps” (or tables) from the file that are to be used, whether these dumps should be output to separate files, and whether informational messages will be printed for each dump.
- [`-sample_interval=number`]: Specifies sparsing of the data, so that only every number-th data point is used.
- `-first=quantity_name[=alias]` `-second=quantity_name[=alias]`: Specifies output of pairs of data (to the first and second columns of `mpl-format` files). The filename for each pair will be constructed from the `outputfile_root` and the names of the quantities (or their aliases, if any).
- `-sequence[=auxiliary_name[=alias]]` `-quantity=quantity_name[=alias]`: Specifies output to `mpl-format` files of data as a function of an auxiliary variable or the dump “time” counter (which is a mandatory auxiliary quantity, and a left-over from the early days of `awe`). The filename for each pair will be constructed from the `outputfile_root` and the names of the quantities (or their aliases, if any).

- `-contour_grid=min1,max1,min2,max2,n1,n2[, 'combine'][, 'simple'] :`
Specifies that the user wishes to create data suitable for input to the `contour` program for contour plotting, computation of path integrals, etc. The `-first` and `-second` arguments give the names of the independent variables (call them (x_1, x_2)) of the contour map, with the `-quantity` arguments giving the names of any number of dependent variables (for separate output). The items for use with the `-contour_grid` keyword are the extent of the contour map in the x_1 and x_2 , and the number of grid points in each dimension. The 'combine' and 'simple' options specify the type of data interpretation. If 'combine' is given, then data from all dumps is combined before processing; otherwise, dumps are processed separately. If 'simple' is given, then the program assumes that (x_1, x_2) pairs lie on the grid specified by the arguments, which reduces the processing to simply putting each data point in array location of the closest grid point to any given (x_1, x_2) pair. If 'simple' is not given, then the program interpolate in two dimensions to find the value of the dependent variables at each grid point, which is a much more time-consuming process, but necessary for processing data from programs that use irregular meshes (like SUPERFISH). This latter procedure is not entirely reliable.
- `-table=filename,quantity_name[,quantity_name...]` : Specifies creation of a text table in the named file, in column format (which is human-readable).

As a simple example of the use of `awe`, suppose that one has just run `elegant` with a variable quadrupole strength in order to do a simulated emittance measurement (see Chapter 5). The beam-size and quadrupole strength, along with many other parameters, are stored in the "final parameters" output file, which I will refer to as `emitmeas.fin` in the example. I also show the use of `mpl` to plot the data:

```
! Extract the horizontal RMS beam-size (called "Sx" by elegant) vs the quadrupole
! strength (called "Q4[K1]"):
$ awe emitmeas.fin em -first:"Q4[K1]=K1" -second="Sx"
```

```
file opened: em_K1_Sx.out
```

```
! Plot this data using symbol 28, with points connected by lines:
```

```

$ mpl em_k1_sx.out -plot_code=0,28 -connect
! Extract the emittance for both planes as a function of Q4 strength. elegant
! uses "ex" and "ey" for the emittances in the x and y planes, respectively.
$ awe emitmeas.fin em -first:"Q4[K1]=K1","Q4[K1]" -second="ex","ey"
file opened: em_K1_ex.out
file opened: em_K1_ey.out
! Plot the emittances for both planes, using different symbols:
$ mpl em_k1_ex.out,em_k1_ey.out -plot_code=0,28,1,29 -connect
! Extract the geometric mean of the emittances vs Q4 strength:
$ awe emitmeas.fin em -first:"Q4[K1]" -second=eg &
-define=eg,m-rad,"ex ey * sqrt"
1 new quantity was defined:
    eg (m-rad): ex ey * sqrt
file opened: em_K1_eg.out
! Plot this along with x and y emittances, changing plotter pens between data sets.
$ mpl em_K1_e%.out -multi_pen
! Make a table containing the quadrupole strength, horizontal beta function, and
! the elements of the horizontal transport matrix, R, along with  $1 - \det(R)$ :
$ awe emitmeas.fin &
-define=odetR," ", "1 R11 R22 * R12 R21 * - -" &
-define=betax,m,"Sx 2 pow ex /" &
-table=horiz.tab,Q4[K1],Sx,R11,R12,R21,R22,betax,odetR
2 new quantities were defined:
    odetR (:): 1 R11 R22 * R12 R21 * - -
    betax (m): Sx 2 pow ex /

```

The file `emitmeas.fin` contains 46 quantities as a function of the quadrupole strength, including beam-sizes, emittances, transport-matrix elements, and more. I leave it to the reader to imagine how unwieldy it would be to have these quantities printed to a text file in the fashion typical of physics programs. With **awe**, the user selects just the data he is interested in, and manipulates it into the desired form with a minimum of effort. This would be powerful enough as the interface to a single physics program (**elegant**, say), but it is all the more powerful in providing a uniform

interface to many different programs, as well as an interface *between* different physics programs (e.g., between MASK and **elegant**, or **elegant** and **emitmeas**).

Note that since **awe** format is self-describing, upgrades to **elegant** that result in more data being sent to the "final parameters" file (or any other file) will not change the user interface, beyond making more data available to the user via **awe**. (In fact, the final parameters file contains a variable number of quantities, depending on how many quantities the user chooses to vary in his **elegant** simulation.) This applies to the interface between programs as well, since a program that accepts **awe**-format input obtains its data by "asking for it" by name. For example, the program **emitmeas** (see Chapter 5) finds the data for the R-matrix and beam-sizes by finding quantities with the appropriate names (the same names used in the examples above). A set of subroutines is available for use in any program that needs to utilize data stored in **awe** format.

I will not give a detailed description (i.e., at the byte level) of **awe** format here beyond what has been given above, since the format is going to undergo modifications in the near future to further improve its functionality. The upcoming changes will allow further expansions of the format without invalidating data files stored in a previous version of the format, by the addition of a format version number. This will be done before any release of the program is made, to forestall problems with multiple versions that use different formats. Also, the format will be expanded to include text descriptions for each variable, format-specifiers for each variable (to specify how the data should be printed when ascii output is requested), and text descriptions of each individual table in a file (in addition to the existing text description of the file as a whole), in addition to other changes.

This issue of changing formats should not be confused with the issue of whether **awe** can accept data tables other than those it is current working with. There is no limitation (except at the hardware level) on the creation of new data tables in the existing **awe** format. Any new application can describe a new data-table in the format **awe** currently accepts. The upcoming changes in **awe** format refer to improvements in the way programs can describe their data to **awe** or to other programs that call the **awe** subroutine library to read **awe** format files.

Bibliography

- [1] Y.Minowa (Mitsubishi Electric). Japanese Government Patent, Number SHO-WA58-20180, 1983. (Applied for: 1974, Public Notice: 1975).
- [2] G. A. Westenskow and J. M. J. Madey. Microwave electron gun. *Laser and Particle Beams*, 2:223-225, 1984.
- [3] H. Goldstein. *Classical Mechanics*. Addison Wesley, Reading, Massachusetts, second edition, 1981.
- [4] M. Weiss. A Short Demonstration of Liouville's Theorem. In *Proceedings of the 1986 CERN Accelerator School*, July 1987.
- [5] L. D. Landau, E. M. Lifshitz. *Statistical Physics, Part 1*. Pergammon Press, Oxford, third edition, 1980.
- [6] H. Wiedemann. Physics of Particle Accelerators. Lecture notes of course given in Fall 1987 in the Stanford University Applied Physics Department, 1987.
- [7] M. Reiser. Theory and Design of Charged Particle Beams. Draft of a forthcoming book, Spring, 1989.
- [8] M. Sands. The Physics of Electron Storage Rings. Technical Report SLAC-121, SLAC, November 1970.
- [9] E. D. Courant and H. S. Snyder. Theory of the Alternating Gradient Synchrotron. *Annals of Physics*, 3:1-48, 1958.

- [10] K. L. Brown. A First- and Second-Order Matrix Theory for the Design of Beam Transport Systems and Charged Particle Spectrometers. SLAC Report SLAC-75, SLAC, June 1982.
- [11] K. T. McDonald and D. P. Russell. Methods of emittance measurement. Technical Report DOE/ER/3072-51, Princeton University, March 7 1989.
- [12] B. E. Carlsten and R. L. Sheffield. Photoelectric Injector Design Considerations. In *Proceedings of the 1988 Linear Accelerator Conference*, October 1988.
- [13] R.L.Sheffield. Photocathode RF Guns. In *Physics of Particle Accelerators, AIP Conference Proceedings* 184, 1987-1988.
- [14] C. Travier. RF Guns: A Review. RFG Note SERA/90-219/RFG, Laboratoire De L'Accelerateur Lineaire, August 1990.
- [15] J. C. Gallardo and R. B. Palmer. Preliminary Study of Gun Emittance Correction. *IEEE Journal of Quantum Electronics*, 26(8):1328-1331, 1990.
- [16] M. Reiser. Physics of High-Brightness Sources. In *Proceedings of the 1989 Workshop on Advanced Accelerator Concepts*, January 1989.
- [17] R. D. Ruth. Report on the International Workshop on Next Generation Linear Colliders. In *Proceedings of the IEEE Particle Accelerator Conference*, pages 716-720, March 1989.
- [18] P. B. Wilson. Wakefield Acceleration: Concepts and Machines. In *High-Brightness Accelerators*, pages 129-155. NATO Advanced Study Institute, 1986.
- [19] A. M. Sessler and D. B. Hopkins. The Two-Beam Accelerator. In *1986 Linear Accelerator Conference Proceedings*, pages 385-390, 1986.
- [20] R. H. Pantell. Free-Electron Lasers. In *Physics of Particle Accelerators*, volume 184 of *AIP Conference Proceedings*, pages 1707-1728, 1989.
- [21] C. A. Brau. Free-Electron Lasers. In *Physics of Particle Accelerators*, volume 184 of *AIP Conference Proceedings*, pages 1615-1706, 1989.

- [22] A. Hofmann. Theory of Synchrotron Radiation. ACD Note 38, SSRL, September 1986.
- [23] S. Krinsky. Undulators as Sources of Synchrotron Radiation. *IEEE Transactions on Nuclear Science*, NS-30(4):3078-3082, 1983.
- [24] K.-J. Kim. Angular Distribution of Undulator Power for an Arbitrary Deflection Parameter K. *Nuclear Instruments and Methods*, A246:67-70, 1986.
- [25] H. Motz. Applications of the Radiation from Fast Electron Beams. *Journal of Applied Physics*, 22(5):527-535, 1951.
- [26] H. Wiedemann, *et. al.* 3 GeV SPEAR Injector Design Handbook. Technical report, SSRL, March 1988.
- [27] Kwang-Je Kim. Brightness and Coherence of Radiation from Undulators and High-Gain Free Electron Lasers. In *IEEE Particle Accelerator Conference Proceedings*, 1987.
- [28] M. Borland. Calculating Emittance from Images of Undulator Radiation. In *IEEE Particle Accelerator Conference Proceedings*, 1989.
- [29] L. Mandel and E. Wolf. Coherence Properties of Optical Fields. *Reviews of Modern Physics*, 37(2):231-284, 1965.
- [30] E. Hecht and A. Zajac. *Optics*. Addison-Wesley, Reading, Mass., 1979.
- [31] J. D. Jackson. *Classical Electrodynamics*. J. Wiley, New York, second edition, 1975.
- [32] G. A. Westenskow, J. M. J. Madey, L. C. Vintro, S. V. Benson. Owner's Manual for the Microwave Electron Gun. HEPL Technical Note TN-86-1, HEPL, February 1986.
- [33] W. C. Turner, *et. al.* High-Brightness, High-Current Density Cathode for Induction Linac FELs. In *Proceedings of the 1988 Linear Accelerator Conference*, October 1988.

- [34] J.S.Fraser, R.L.Sheffield, E.R. Gray, G. W. Rodenz. High-Brightness Photoemitter Injector for Electron Accelerators. In *IEEE Particle Accelerator Conference Proceedings*, 1985.
- [35] B.E.Carlsten and R. L. Sheffield. Photoelectric Injector Design Considerations. In *Proceedings of the Linear Accelerator Conference*, 1988.
- [36] K. T. McDonald. Design of the Laser-Driven RF Electron Gun for the BNL Accelerator Test Facility. *IEEE Transactions on Electron Devices*, 35(11), 1988.
- [37] J.S.Fraser, R.L.Sheffield, E.R. Gray, P.M.Giles, R.W.Springer, V.A.Loeb. Photocathodes in Accelerator Applications. In *IEEE Particle Accelerator Conference Proceedings*, 1987.
- [38] P. E. Oettinger, R. E. Shefer, D. L. Birx, M. C. Green. Photoelectron Sources: Selection and Analysis. *Nuclear Instruments and Methods*, A272:264-267, 1988.
- [39] S. V. Benson, J. Schultz, B. A. Hooper, R. Crane, J.M.J.Madey. Status Report on the Stanford Mark III Infrared Free Electron Laser. *Nuclear Instruments and Methods*, A272:22-28, 1988.
- [40] J.S.Fraser, R.L.Sheffield, E.R. Gray, P.M.Giles, R.W.Springer, V.A.Loeb. Photocathodes in Accelerator Applications. In *IEEE Particle Accelerator Conference Proceedings*, 1987.
- [41] M. B. James. Production of High-Intensity Electron Bunches for the SLAC Linear Collider. SLAC Report SLAC-Report-319, SLAC, August 1987.
- [42] S. P. Kapitza and V. N. Melekhin. *The Microtron*. harwood, London, 1969.
- [43] R. B. Neal. A High Energy Linear Electron Accelerator. M. L. Report 185, Stanford Microwave Laboratory, February 1953.
- [44] E. Tanabe. Private communication.
- [45] H.A.Eng. Achromatic Magnetic Mirror for Ion Beams. *The Review of Scientific Instruments*, 34(4), 1963.

- [46] T. I. Smith. Intense Low-Emittance Linac Beams for Free Electron Lasers. In *Proceedings of the Linear Accelerator Conference*, pages 421–425, June 1986.
- [47] G. A. Loew, R. H. Miller, C. K. Sinclair. The SLAC Low-Emittance Accelerator Test Facility. In *Proceedings of the Linear Accelerator Conference*, pages 144–147, June 1986.
- [48] R. B. Neal, editor. *The Stanford Two-Mile Accelerator*, R.B.Neal, editor. W.A.Benjamin Inc., 1968.
- [49] M. Borland. elegant: A Matrix/Integrating Code for Third-Order Tracking. ACD-Note, SSRL. To be published.
- [50] M. Borland. rfgun: A Program to Simulate RF Guns. ACD-Note, SSRL. To be published.
- [51] A.T.Drobot, et. al. Numerical Simulation of High Power Microwave Sources. *IEEE Trans.*, 32:2733–7, 1985.
- [52] K.Halbach, R.F.Holsinger. SUPERFISH—A Computer Program for Evaluation of RF Cavities with Cylindrical Symmetry. *Particle Accelerators*, 7:213–222, 1976.
- [53] E.Tanabe, M.Borland, M.C.Green, R.H.Miller, L.V.Nelson, J.N.Weaver, H.Wiedemann. A 2-MeV Microwave Thermionic Gun. SLAC Publication SLAC-PUB-5054, SLAC, August 1989.
- [54] M.Borland, M.C.Green, R.H.Miller, L.V.Nelson, E.Tanabe, J.N.Weaver, H.Wiedemann. Performance of the 2 MeV Microwave Gun for the SSRL 150 MeV Linac. In *Proceedings of the Linear Accelerator Conference*, September 1990.
- [55] G. A. Loew, R.Talman. Elementary Principles of Linear Accelerators. SLAC Publication SLAC-PUB-3221, SLAC, September 1983.
- [56] P. B. Wilson. High-Energy Electron Linacs: Applications to Storage Ring RF Systems and Linear Colliders. SLAC Publication SLAC-PUB-2884, SLAC, February 1982.

- [57] J. N. Weaver. Formulas for Measuring Q_o , β , E_{\max} , and B_{\max} in a Superconducting Cavity. Technical Report TN-68-21, SLAC, July 1968.
- [58] G. A. Loew. Charging and Discharging Superconducting Cavities. Technical Report TN-68-25, SLAC, November 1968.
- [59] M. Bartsch, *et. al.* MAFIA Release 3.X. In *Proceedings of the Linear Accelerator Conference*, Albuquerque, NM, 1990.
- [60] J. Gao. The Precise Measurement of Electric and Magnetic Fields in a Resonant Cavity. In *Proceedings of the Linear Accelerator Conference*, Albuquerque, NM, 1990.
- [61] W. H. Press, B. P. Flannery, S. A. Teukolsky, W. T. Vetterling. *Numerical Recipes in C*. Cambridge University Press, Cambridge, 1988.
- [62] C. Kittel and H. Kroemer. *Thermal Physics*. W.H. Freeman, San Francisco, second edition, 1980.
- [63] R.H. Miller. Private communication.
- [64] M. Abramowitz and I.A. Stegun. *Handbook of Mathematical Functions with Formulas, Graphs, and Mathematical Tables*. National Bureau of Standards, Washington, D.C., 1964.
- [65] U. Laustroer, U. Van Rienen, T. Weiland. URMEL and URMEL-T User Guide. Technical Report DESY-M-83-03, DESY, February 1987.
- [66] K. Halbach. A Program for the Inversion of System Analysis and Its Application to the Design of Magnets. In *Proceedings of the 2nd Conference on Magnet Technology*, Oxford, England, 1967.
- [67] K. G. Steffen. *High Energy Beam Optics*. Wiley, New York, 1965.
- [68] K. L. Brown, F. Rothacker, D.C. Carey, Ch. Iselin. TRANSPORT: A Computer Program for Designing Charged Particle Beam Transport Systems. SLAC Report SLAC-91, SLAC, May 1977.

- [69] R.H.Helm, R.H.Miller. *The Stanford Two-Mile Accelerator*, R.B.Neal, editor. W.A.Benjamin Inc., 1968.
- [70] H.Wiedemann, *et. al.* 3 GeV SPEAR Injector Design Handbook. Technical report, SSRL, March 1988.
- [71] F. C. Iselin, J. Niederer. The MAD Program (Methodical Accelerator Design) Version 7.2 User's Reference Manual. Technical Report CERN/LEP-TH/88-38, CERN, July 1988.
- [72] B.E.Carlsten, B.D.McVey, E.M.Svaton, G.R.Magelssen, L.M.Young. Magnetic Bunchers for the Generation of High Peak Current, Low Emittance Electron Pulses at Medium Energy. In *Proceedings of the Linear Accelerator Conference*, September 1990.
- [73] R. I. Cutler, E. R. Lindstrom, S. Penner. Conceptual Design of a High Current Injector for the NIST-NRL Free Electron Laser. In *Proceedings of the IEEE Particle Accelerator Conference*, pages 328-330, March 1989.
- [74] C. Bourat, G. Meyrand, D. T. Tran, D. Tronc, A. Massarotti, A. Wrulich. The 100 MeV Preinjector for the Trieste Synchrotron. In *Proceedings of the IEEE Particle Accelerator Conference*, pages 935-937, March 1989.
- [75] U. Bizzarri, *et. al.* Status of the Free Electron Laser Experiment at the ENEA Frascati Center. *Nuclear Instruments and Methods*, A237:213-219, 1985.
- [76] J. Rees. A Progress Report on the SLAC Linear Collider. In *Proceedings of the Linear Accelerator Conference*, pages 209-213, June 1986.
- [77] M. Borland, J.N. Weaver, R. Anderson, M. Baltay, L. Emery, A.S. Fisher, R. Hettel, R.H. Miller, H. Morales, J. Sebek, B. Youngman. Design and Performance of the Traveling-Wave Beam Chopper for the SSRL Injector. In *To be published in IEEE Particle Accelerator Conference Proceedings*, San Francisco, CA, 1991.
- [78] J. Sebek, M. Baltay, M. Borland, J. Cerino, L. Emery, R. Hettel, H. Morales, D. Mostowfi, J.-L. Pellegrin, M. Rowen, J. Safranek, V. Smith, J. Voss, J.N.

- Weaver, H. Wiedemann, Y. Yin, B. Youngman. Diagnostic Instrumentation for the SSRL 3 GeV Injector for SPEAR. In *To be published in IEEE Particle Accelerator Conference Proceedings*, San Francisco, CA, 1991.
- [79] J.N Weaver, S. Baird, M. Baltay, M. Borland, C. Chavis, L. Emery, R. Hettel, S.J. Mello, R.H. Miller, H. Morales, H.-D. Nuhn, J. Safranek, J. Sebek, J. Voss, D. Wang, H. Wiedemann, B. Youngman. The Linac and Booster RF System for a Dedicated Injector for SPEAR. In *To be published in IEEE Particle Accelerator Conference Proceedings*, San Francisco, CA, 1991.
- [80] J. Sebek. Private communication.
- [81] E. Benson, J. N. Weaver. Private communication.
- [82] R. L. Sheffield. Private communication.
- [83] M. C. Ross, N. Phinney, G. Quickfall, H. Shoaee, J. C. Sheppard. Automated Emittance Measurements in the SLC. SLAC Publication SLAC-PUB-4278, SLAC, March 1987.
- [84] K. L. Brown, R. V. Servranckx. First- and Second-Order Charged Particle Optics. SLAC Publication SLAC-PUB-3381, SLAC, July 1984.
- [85] P. R. Bevington. *Data Reduction and Error Analysis for the Physical Sciences*. McGraw-Hill, New York, 1969.
- [86] M. C. Ross, J. T. Seeman, R. K. Jobe, J. C. Sheppard, R. F. Stiening. High Resolution Beam Profile Monitors in the SLC. *IEEE Transactions on Nuclear Science*, NS-32:2003-2005, 1985.
- [87] K. D. Jacobs, J. B. Flanz, T. Russ. Emittance Measurements at the Bates Linac. In *IEEE Particle Accelerator Conference Proceedings*, Chicago, IL, 1989.
- [88] M. C. Ross. Using Television Cameras to Measure Emittance. Single Pass Collider Memo CN-280, SLAC, September 1984.
- [89] S. Yenko and D. R. Walz. A High-Resolution Phosphor Screen Beam Profile Monitor. *IEEE Trans.*, 32:2009-2011, 1985.

- [90] J. T. Seeman, V. Luth, M. Ross, J. Sheppard. Beam Tests of Phosphorescent Screens. Single Pass Collider Memo CN-290, SLAC, March 1985.
- [91] B. W. Kernighan and D. M. Ritchie. *The C Programming Language*. Prentice-Hall, Englewood Cliffs, N.J., second edition, 1988.

Errata

19 November 1991

Errata are listed by section number.

• 3.3.2

- I've used the prime symbol inconsistently in this section. In particular, x' and y' are slopes relative to the central trajectory, while q'_i ($i=1,2,3$) are velocities (normalized to βc).
- In equations 3.64 and 3.75, the fourth entry of the right-hand vector should be $\frac{q'_3}{\sqrt{1-q_3'^2} \cos(\text{atan}(x'))}$.
- Just before equations 3.66, 3.71, and 3.76, replace the word "slopes" by "velocities".
- Equation 3.67 should have a minus sign in front of the square-root sign.
- In equation 3.70, replace q'_3 by q'_3/q'_2 .

• 3.3.3

- In equation 3.82, the second entry of the right-hand vector should be Q'_1/Q'_2 , and the fourth entry should be Q'_3/Q'_2 .

• 3.5.2

- In Table 3.5, the following matrix elements should be changed to the values given:

$$\begin{aligned} U_{3422} &= 7.202 \\ U_{3432} &= -2.728 \cdot 10^{-3} \\ U_{3444} &= -1.113 \cdot 10^2 \\ U_{4322} &= 1.282 \cdot 10^1 \\ U_{4333} &= -4.324 \cdot 10^{-1} \\ U_{4432} &= -1.439 \cdot 10^{-3} \\ U_{4433} &= -1.445 \\ U_{4443} &= 8.683 \cdot 10^1 \\ U_{4444} &= -3.154 \cdot 10^2 \end{aligned}$$

- In Table 3.7, the following matrix elements should be changed to the values given:

$$\begin{aligned} U_{3422} &= -6.979 \cdot 10^{-1} \\ U_{3444} &= 3.661 \cdot 10^{-1} \\ U_{4311} &= -1.491 \\ U_{4321} &= -6.846 \\ U_{4322} &= -6.318 \\ U_{4333} &= 2.389 \cdot 10^{-1} \\ U_{4411} &= 6.622 \\ U_{4421} &= 1.452 \cdot 10^1 \\ U_{4422} &= 6.901 \\ U_{4433} &= -5.745 \cdot 10^{-1} \\ U_{4443} &= -1.683 \\ U_{4444} &= 2.312 \\ U_{4641} &= 1.269 \end{aligned}$$

- In Table 3.9, the following matrix elements should be changed to the values given:

$$U_{1641} = 6.914 \cdot 10^{-4}$$

$$U_{3422} = -1.376$$

$$U_{3444} = -3.287$$

$$U_{4311} = -1.021 \cdot 10^1$$

$$U_{4333} = -3.022$$

$$U_{4411} = -1.434 \cdot 10^1$$

$$U_{4422} = -1.762$$

$$U_{4431} = -1.087 \cdot 10^{-3}$$

$$U_{4433} = -1.321 \cdot 10^1$$

$$U_{4444} = -8.426$$

$$U_{4631} = -2.404 \cdot 10^1$$

$$U_{4641} = -2.923 \cdot 10^1$$

$$U_{4643} = -1.008 \cdot 10^{-3}$$

$$U_{4663} = -1.481 \cdot 10^1$$

$$U_{4664} = -1.615 \cdot 10^1$$